



UNIVERSITAT  
POLITÈCNICA  
DE VALÈNCIA



# **Application of multivariate image analysis to prostate cancer for improving the comprehension of the related physiological phenomena and the development and validation of new imaging biomarkers**

## **Author:**

Eric Aguado Sarrió

## **Supervisors**

José Manuel Prats Montalbán

Roberto Sanz Requena

Valencia, October 2019

A doctoral thesis submitted to the Department of applied statistics, Operations Research and Quality



UNIVERSITAT  
POLITÈCNICA  
DE VALÈNCIA



---

## Acknowledgments

This journey started six years ago after finishing the last exams of my Master degree. In that summer of 2013 I was thinking about my future and how to orientate the Master's thesis. Truly, I had no idea on what to do, but Alberto Ferrer, after the presentation of my work for his subject, suggested me to have a meeting with José Manuel Prats where they showed me the interesting new approach of “our” methods to medical imaging they were working on. I got involved so easy in this world by their hand, and after all this time, they have been the best supervisors I could ever imagined. I learnt how to investigate; they taught me about the importance of knowing the process in detail before trying anything, to argue everything, to propose new ideas, the importance of the testing/validation, to give a measure of the reliability of the results and more, a bunch things that will make this list extremely long. Thank you so much, Alberto and José Manuel. A few more words for JM, he has been always there for me, in the best and worst moments, he is an amazing professor and better person. To my second supervisor Roberto Sanz, it was always a pleasure to work with him. The relation between these two worlds (university and hospital) is never easy, but he managed to go with us together in the same direction during this journey. Roberto, thank you for your dedication and hard work of giving us always the best data set you can, listening to our ideas and contributing with your valuable advices. I would like to thank Luís Martí Bonmatí for introducing us into this world and saving some time from his busy schedule for us, always in a kind way. I would also like to thank all the people from the Hospital Quirón, without their work and their images, this thesis wouldn't have been possible.

To my office mates. Dani, we know each other for a long time and we have travelled a lot together, it was always nice to have him on the other side of the table. To Raffa and Abel for helping me and answering to all my questions. To Borja and Antonio for having good times discussing and arguing together. To Alba and Joan, we didn't share so much time but they are magnificent and very talented people.

To my “all time” friends in my little village, Kike, Mode, Jorge, Javi, Toni, Carles, etc. for the long nights of just talking. To my friends in the city, Vicci and Rivera, we lived together 4 years and I got so many precious memories that will stay with me forever.

And last, but not least, to my family, they always supported me, gave me their love and tried to charm me up when I felt bad. But also to celebrate when we succeed. Unfortunately, my “uelos” aren't with us anymore, I dedicate this work to them and hope they would have been proud of me. Thank you.



---

## Contributions

List of contributions authored by the candidate during the development of the thesis:

### *Peer-reviewed publications*

1. Aguado-Sarrió E, Prats-Montalbán JM, Sanz-Requena R, Alberich-Bayarri A, Martí-Bonmatí L, Ferrer A. Prostate diffusion weighted-magnetic resonance image analysis using multivariate curve resolution methods. *Chemom. Intell. Lab. Syst.* 2015; 140: 43-8.
2. Prats-Montalbán JM, Aguado-Sarrió E, Ferrer A. (2016) Multivariate Curve Resolution for Magnetic Resonance Image analysis: applications in prostate cancer biomarkers development. In *"Resolving Spectral Mixtures, with application from ultrafast spectroscopy to super-resolution imaging"*, Data Handling in Science and Technology 30, 519–550, Elsevier, Amsterdam.
3. Aguado-Sarrió E, Prats-Montalbán JM, Sanz-Requena R, Garcia-Martí G, Martí-Bonmatí L, Ferrer A. Biomarker comparison and selection for prostate cancer detection in Dynamic Contrast Enhanced-Magnetic Resonance Imaging (DCE-MRI). *Chemom. Intell. Lab. Syst.* 2017; 165: 38-45.
4. Aguado-Sarrió E, Prats-Montalbán JM, Sanz-Requena R, Duchesne C, Martí-Bonmatí L, Ferrer A. Assessment of prostate cancer aggressiveness by combining mpMRI and multivariate image analysis methods. *Submitted*.

### *Oral communications in conferences*

1. Aguado-Sarrió, E.; Prats-Montalbán, J.M.; Ferrer Riquelme A. Prostate Diffusion Weighted-Magnetic Resonance Image Analysis using Multivariate Curve Resolution Methods. *VI Chemometrics Workshop for Young researchers*. Valencia (Spain) Oct. 2015.
2. Aguado-Sarrió, E.; Prats-Montalbán, J.M.; Ferrer Riquelme, A. Análisis de imágenes de resonancia magnética de difusión en próstata empleando los métodos de resolución multivariante de curvas. *Congreso Anual de la Sociedad Española de Ingeniería Biomédica (CASEIB)*. Madrid (Spain) Nov. 2015.
3. Aguado-Sarrió, E.; Prats-Montalbán, J.M.; Sanz Requena, R.; Ferrer A. Martí-Bonmatí, L. Mejora en la detección del cancer de próstata usando biomarcadores de modelos farmacocinéticos de segunda generación y métodos estadísticos de variables latentes. *Congreso Anual de la Sociedad Española de Ingeniería Biomédica (CASEIB)*. Valencia (Spain). Nov. 2016.
4. Aguado-Sarrió, E.; Prats-Montalbán, J.M.; Sanz Requena, R.; Ferrer A. Martí-Bonmatí, L. Functional MRI Analysis using multivariate curve resolution methods: developing cancer biomarkers. *15th Scandinavian Symposium on Chemometrics (SSC15)*. Naantali (Finland). June. 2017.



---

## Abstract

The increase in life expectancy and population with age higher than 50 years is producing a major number of detected cases of prostate cancer (PCa). For this reason, the resources are focused in the early diagnosis and effective treatment. In spite of multiple studies with histologic discriminant biomarkers, it is hard to clearly differentiate the low aggressiveness PCa cases from those that will progress and produce mortality or rather a decrease in the life expectancy.

With the objective of improving the diagnosis, location and gradation of the malignant tumors, Magnetic Resonance Imaging (MRI) has come up as the most appropriate image acquisition technique for cancer studies, which provides a non-invasive, sensitive and specific diagnosis, based on morphological and functional (blood perfusion and water diffusion) sequences. The different characteristics and parameters extracted from these sequences, known as imaging biomarkers, can evaluate the different processes associated to tumor development, like pharmacokinetic modeling for angiogenesis assessment (perfusion) or mono- and bi-exponential signal decay modeling for cellularization (diffusion).

Normally, these imaging biomarkers are analyzed in a “univariate” way, without taking advantage of the internal correlation structures among them. One way to improve this analysis is by applying Multivariate Image Analysis (MIA) statistical techniques, obtaining simplified (latent) structures that help to understand the relation between parameters (variables) and the inner physiological processes, moreover reducing the uncertainty in the estimation of the biomarkers.

In this thesis, new imaging biomarkers are developed for perfusion and diffusion by applying MIA tools like Multivariate Curve Resolution Alternating Least Squares (MCR-ALS), obtaining parameters with direct clinical interpretation. Partial Least Squares (PLS) based methods are then used for studying the classification capability of these biomarkers. First, perfusion imaging biomarkers have been tested for tumor detection (control vs lesion). Then, diffusion + perfusion have been combined to study tumor aggressiveness by applying PLS-multiblock methods (SMB-PLS).

The results showed that MCR-based perfusion biomarkers performed better than state-of-the-art pharmacokinetic parameters for lesion differentiation. Regarding the assessment of tumor aggressiveness, the combination of diffusion-based imaging biomarkers (using both the parametric models and MCR) and normalized T2-weighted measurements provided the best discriminating outcome, while perfusion was not needed as it did not supply additional information.

In conclusion, MIA can be applied to morphologic and functional MRI to improve the diagnosis and aggressiveness assessment of prostate tumors by obtaining new quantitative parameters and combining them with state-of-the-art imaging biomarkers.



---

## Resumen

El aumento de la esperanza de vida en la población con edad por encima de 50 años está generando un mayor número de casos detectados de cáncer de próstata (CaP). Por este motivo, los recursos se destinan al diagnóstico en etapas tempranas y al tratamiento efectivo. A pesar de la multitud de estudios basados en biomarcadores y discriminación histológica, es difícil diferenciar con efectividad los casos de CaP con baja agresividad de aquellos que progresarán y acabarán produciendo mortalidad o una disminución en la esperanza de vida del paciente. Con el objetivo de mejorar el diagnóstico, localización y gradación de los tumores malignos, las técnicas de imagen por Resonancia Magnética (MRI) son las más adecuadas para el estudio del cáncer, proporcionando métodos de diagnóstico no-invasivos, sensibles y específicos, basados en secuencias morfológicas (T2w) y funcionales (perfusión de la sangre y difusión del agua). Las diferentes características y parámetros extraídos de estas secuencias, conocidos como biomarcadores de imagen, pueden evaluar las diferencias asociadas al desarrollo de los procesos tumorales, como los modelos farmacocinéticos para estudiar angiogénesis (perfusión) y los modelos mono- y bi-exponenciales para estudiar la caída de la señal en difusión con el objetivo de estudiar la celularización. Normalmente, estos biomarcadores de imagen se analizan de forma “univariante”, sin aprovechar la información de las estructuras de correlación interna que existen entre ellos. Una manera de mejorar este análisis es mediante la aplicación de las técnicas estadísticas que ofrece el Análisis Multivariante de Imágenes (MIA), obteniendo estructuras (latentes) simplificadas que ayudan a entender la relación entre los parámetros (variables) y sus propios procesos fisiológicos, además de reducir la incertidumbre en la estimación de los biomarcadores. En esta tesis, se han desarrollado nuevos biomarcadores de imagen para perfusión y difusión con la aplicación de alguna de las herramientas de MIA como la Resolución Multivariante de Curvas con Mínimos Cuadrados Alternos (MCR-ALS), obteniendo parámetros que tienen interpretación clínica directa. A continuación, los métodos basados en mínimos cuadrados parciales (PLS) se aplicaron para estudiar la capacidad de clasificación de estos biomarcadores. En primer lugar, los biomarcadores de perfusión se utilizaron para la detección de tumores (control vs lesión). Posteriormente, la combinación de perfusión + difusión + T2 se empleó para estudiar agresividad tumoral con la aplicación de métodos PLS multibloque, en concreto (secuencial) SMB-PLS. Los resultados mostrados indican que los biomarcadores de perfusión obtenidos mediante MCR son mejores que los parámetros farmacocinéticos en la diferenciación de la lesión. Con lo que respecta al estudio de la agresividad tumoral, la combinación de los biomarcadores de difusión (empleando ambos métodos: modelos paramétricos y MCR) y los valores de T2w normalizados proporcionaron los mejores resultados.

En conclusión, MIA se puede aplicar a las secuencias morfológicas y funcionales de resonancia magnética para mejorar el diagnóstico y el estudio de la agresividad de los tumores en próstata. Obteniendo nuevos parámetros cuantitativos y combinándolos con los biomarcadores más ampliamente utilizados en el ambiente clínico.



---

## Resum

El increment de la esperança de vida en la població per damunt dels 50 anys està generant un major nombre de casos detectats de càncer de pròstata (CaP). Per aquest motiu, els recursos es destinen al diagnòstic en etapes primerenques i al tractament efectiu. Tot i la multitud de estudis basats en biomarcadors y discriminació histològica, es difícil diferenciar amb efectivitat els casos de CaP que tenen baixa agressivitat dels que progressaran y acabaran produint mortalitat o una disminució en la esperança de vida del pacient. Amb el objectiu de millorar el diagnòstic, localització y gradació dels tumors malignes, les tècniques de imatge per Ressonància Magnètica (MRI) son els mètodes més adequats per al estudi del càncer, proporcionant metodologies de diagnòstic no-invasius, sensibles y específiques basades en seqüències morfològiques (T2w) y funcionals (perfusió de la sang y difusió del aigua). Les diferents característiques i paràmetres extrets de aquestes seqüències, coneguts com biomarcadors d'imatge, poden avaluar las diferències associades al desenvolupament dels processos tumorals. Primer, amb els models farmacocinètics per a estudiar angiogènesis (perfusió) y segon, amb els models mono- i bi-exponencials per a estudiar la caiguda de la senyal en difusió amb el objectiu de estudiar la cel·lularització. Normalment, aquests biomarcadors d'imatge s'analitzen de forma "univariant", sense aprofitar la informació de las estructures de correlació interna que existeixen entre ells. Una forma de millorar aquest anàlisis es mitjançant la aplicació de las tècniques estadístiques aportades pel Anàlisis Multivariant de Imatges (MIA), obtenint estructures (latents) simplificades que ajuden a entendre la relació entre els paràmetres (variables) i els seus processos fisiològics, a més de reduir la incertesa en la estimació dels biomarcadors. En aquesta tesis, s'han desenvolupat nous biomarcadors d'imatge per a perfusió i difusió amb la aplicació de alguna de las ferramentes de MIA com la Resolució Multivariant de Corbes i Mínims Quadrats Alterns (MCR-ALS), obtenint paràmetres que tenen interpretació clínica directa. A continuació, els mètodes basats en mínims quadrats parcials (PLS) s'han aplicat per a estudiar la capacitat de classificació d'aquests biomarcadors. En primer lloc, els biomarcadors de perfusió s'han utilitzat per a la detecció de tumors (control contra lesió). Posteriorment, la combinació de perfusió + difusió + T2 s'ha utilitzat per a estudiar agressivitat tumoral amb la aplicació de mètodes PLS multi-bloc, en concret (seqüencial) SMB-PLS. Els resultats mostren que els biomarcadors de perfusió obtinguts mitjançant MCR són millors que els paràmetres farmacocinètics en la diferenciació de la lesió. En lo que es refereix al estudi de la agressivitat tumoral, la combinació dels biomarcadors de difusió (utilitzant els dos mètodes: models paramètrics i MCR) i els valors de T2w normalitzats proporcionaren els millors resultats.

En conclusió, MIA es pot aplicar a les seqüències morfològiques i funcionals de ressonància magnètica per a millorar el diagnòstic i el estudi de l'agressivitat dels tumors en pròstata. Obtenint nous paràmetres quantitativs y combinant-los amb els biomarcadors més utilitzats en el ambient clínic.



---

# Contents

<b>1. HYPOTHESIS AND OBJECTIVES</b> .....	<b>15</b>
<b>1.1. Hypothesis</b> .....	<b>15</b>
<b>1.2. Objectives</b> .....	<b>15</b>
1.2.1. First objectives .....	15
1.2.2. Second objectives .....	16
<b>2. INTRODUCTION</b> .....	<b>17</b>
<b>2.1. Prostate cancer (PCa)</b> .....	<b>17</b>
2.1.1. General aspects and risk factors .....	17
2.1.2. Anatomy and histology .....	18
2.1.3. Diagnosis .....	21
<b>2.2. Magnetic resonance imaging (MRI)</b> .....	<b>23</b>
2.2.1. Classical morphologic sequences. T1- and T2-weighted sequences.....	24
2.2.2. Functional MRI sequences .....	26
<b>2.3. Dynamic contrast-enhanced magnetic resonance imaging (DCE-MRI)</b> .....	<b>27</b>
2.3.1. The DCE-MRI acquisition.....	27
2.3.2. DCE-MRI data .....	28
2.3.3. Pharmacokinetic modeling: theory.....	29
2.3.4. Imaging biomarkers calculation (Pharmacokinetic modeling).....	33
<b>2.4. Diffusion-weighted magnetic resonance imaging (DW-MRI)</b> .....	<b>34</b>
2.4.1. The DW-MRI acquisition .....	34
2.4.2. DW-MRI data .....	36
2.4.3. Exponential modeling: theory.....	37
2.4.4. Imaging biomarkers calculation (exponential modeling).....	38
<b>2.5. Multiparametric MRI: PI-RADS and imaging biomarkers limitations</b> .....	<b>39</b>
<b>2.6. Multivariate image analysis and its application to oncology</b> .....	<b>42</b>

<b>3. MATERIALS AND METHODS .....</b>	<b>45</b>
<b>3.1. Materials .....</b>	<b>45</b>
<b>3.2. Statistical models .....</b>	<b>48</b>
3.2.1. PCA .....	48
3.2.2. MCR-ALS .....	49
3.2.3. PLS and PLS-DA.....	51
3.2.4. SMB-PLS.....	52
<b>3.3. Registration method.....</b>	<b>55</b>
<b>4. DEVELOPING NEW IMAGING BIOMARKERS WITH MCR.....</b>	<b>63</b>
<b>4.1. Data structure preparation of MR images .....</b>	<b>63</b>
<b>4.2. Applying MCR to DCE-MRI .....</b>	<b>64</b>
4.2.1. MCR-perfusion sequential step procedure .....	65
4.2.2. A detailed example of MCR-perfusion application.....	67
<b>4.3. Applying MCR to DW-MRI.....</b>	<b>75</b>
4.3.1. MCR-diffusion proposed model .....	76
4.3.2. MCR-diffusion sequential procedure .....	77
4.3.3. MCR-diffusion models discussion.....	82
<b>5. PERFUSION BIOMARKERS COMPARISON FOR CANCER DETECTION.....</b>	<b>87</b>
<b>5.1. Biomarker structure organization .....</b>	<b>88</b>
<b>5.2. Goodness of prediction parameters: f-score, precision and recall .....</b>	<b>88</b>
<b>5.3. Variable selection and classification method .....</b>	<b>89</b>
<b>5.4. Results and discussion .....</b>	<b>92</b>

---

<b>6. STUDY OF AGGRESSIVENESS BY COMBINING DIFFERENT MRI SEQUENCES .....</b>	<b>97</b>
6.1. Data structure organization.....	97
6.2. SMB-PLS-DA iterative procedure method .....	99
6.3. Results and discussion .....	102
<b>7. CONCLUSIONS.....</b>	<b>113</b>
<b>8. FUTURE WORK .....</b>	<b>115</b>
<b>9. REFERENCES .....</b>	<b>117</b>



# Chapter 1

# Hypothesis and Objectives

## 1.1. Hypothesis

The combined analysis of magnetic resonance (MR) imaging biomarkers obtained from clinical models and statistical latent variable based methods can improve the detection and gradation of prostate tumors located in the peripheral zone.

## 1.2. Objectives

### *1.2.1. First objectives*

- To evaluate the applicability of multivariate curve resolution (MCR) to dynamic contrast-enhanced MR imaging (DCE-MRI) of the prostate and to compare the extracted dynamic components with the quantitative parameters (i.e. biomarkers) estimated from state-of-the-art pharmacokinetic models (1<sup>st</sup> and 2<sup>nd</sup> generation).

- To explore the capability of MCR methods to model the different behaviors associated to the water diffusion process in diffusion weighted MRI (DW-MRI), helping specialists to detect and characterize prostate tumors.
- To check the adequacy of the different theoretical models commonly applied in clinical practice, by sequentially incorporating constraints in the MCR algorithm using prior knowledge about the perfusion and diffusion processes.
- To provide new imaging biomarkers that may complement those commonly used for clinical diagnosis (DCE-MRI and DW-MRI).

### ***1.2.2. Second objectives***

- To study the potential of imaging biomarkers for tumor detection.
- To make a model comparison between different imaging perfusion biomarkers, selecting the most relevant ones in terms of tumor detection (minimizing false negatives and false positives rates), thus improving the tissue classification.
- To combine the different functional studied sequences and take advantage of all the sources of information together for improving the characterization of tumors in prostate and differentiate grades of aggressiveness (Gleason scores).

# Chapter 2

## Introduction

### 2.1. Prostate cancer (PCa)

#### *2.1.1. General aspects and risk factors*

Prostate Cancer (PCa) is nowadays the most common malignant neoplasm for men over 50 years. In Europe, the number of diagnosed cases is continuously increasing with a 7% rate per year since the 90's. PCa is also the second one in terms of mortality (only behind lung cancer) [1].

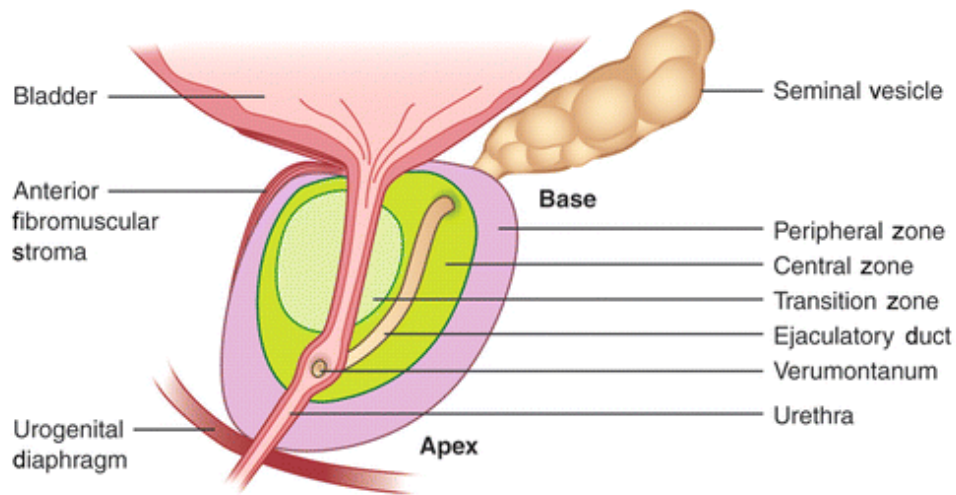
While it is true that PCa mortality rates are falling dramatically, the number of detected cases is increasing, due to the higher life expectancy and population aging, so the efforts are focusing on its early diagnosis and effective treatment. [2]. Thus, most of the cases are diagnosed in the early stages of the disease, when the tumor is still in the gland, and the possibilities of salvation are significantly increasing. However, the focus in early diagnosis also causes the detection of benign or less aggressive tumors with more silent behavior, making the differentiation way more complicated.

Regarding the risk factors, evidence associates PCa to a series of factors, involving, among others, age (risk augmented in patients older than 50 years old), race/ethnicity (more risk in African Americans) and the family history (genetic factors) [3].

### **2.1.2. Anatomy and histology**

Gil Vernet introduced the anatomic concept we have today in 1953 with his work “Biology and pathology in prostate” where the topographic anatomy of the prostate was described [4].

Years later, in 1968, John McNeal, an expert on prostate structure from the University of Stanford, published his first description about the topographic zonal anatomy. In his different works, McNeal described the anatomy from another point of view, establishing the most clinic-pathologic meaningful zonal distribution of the prostate, which is considered the most accurate nowadays (fig. 1).



Source: Verma et al. [5].

**Figure 1. Schematic shown in sagittal view of prostate illustrates normal zonal description of prostatic anatomy.**

According to McNeal’s works [6,7], the prostate is not considered a homogenous gland because three different glandular regions compose it: peripheral zone (PZ), central zone (CZ) and transition zone (TZ). There exists another non-glandular region that should be taken into consideration, composed by fibromuscular tissue (stroma), known as anterior zone (AZ). Besides, the urethra is considered as the reference point for the description of the prostatic region by dividing the organ into the posterior region, mainly glandular, and the anterior region, mainly fibromuscular. Thus, the prostate can be described anatomically as:

- Peripheral zone (PZ) (70% of the prostatic volume). Corresponds to the sub-capsular portion of the posterior aspect of the prostate gland.
- Central zone (CZ) (20-25% of the prostate volume). Corresponds to the base of the prostate surrounding the distal urethra. It contains the ejaculatory ducts.
- Transition zone (TZ) (5-10% of the prostate volume). Wraps up the urethra.
- Anterior zone (AZ). It is composed by fibromuscular tissue without glandular structures. It covers the anterior and anterolateral surfaces of the glandular prostate.

In the case of developing benign prostate hyperplasia (BPH), these percentages may vary, being the TZ the region that achieves the larger prostatic volume [8].

#### **Histology: Zonal distribution of the prostatic pathologies.**

Mainly, two different tissues compose the prostate: the glandular tissue (epithelial component), and the fibromuscular tissue (stromal component), which is located inside the glandular tissue.

According to the prostate zones defined by McNeal, the parenchyma presents some histological singularities. The regions of the prostate differ in their glandular architecture as much as in their epithelial components. The most compact and abundant stroma is located on the TZ, less on the PZ, and even more reduced but compacted in the CZ. The AZ is composed by muscles and fibroconnective tissue, which is continued with the fibers of the detrusor muscle in the anterior face of the bladder [9]. This histology is truly relevant in prostate cancer studies because the illnesses are different depending on the region where they were developed [7]. For example, PCa is more frequently originated in the PZ and the prostate benign hyperplasia is more susceptible to appear in the TZ. The PCa studies are normally focused on analyzing the PZ, since approximately 70-75% of the malignant neoplasias are found in this zone and only 20-30% originated in the TZ [10]. The malignant neoplasias originated in the CZ are infrequent (5-10%) and are normally secondary, generated due to the invasion by the neighborhood of another neoplasia [11]. These are the principal reasons why this work is focused on studying the PCa and its aggressiveness in the PZ.

#### **Histology: Gleason gradation system**

From a histological point of view, the adenocarcinoma is the most frequently type of cancer, as it is represented by the 95% of all the prostate tumors. It is originated in the glandular component of the prostate and it has a well-known pattern that presents its

own characteristics and a particular gradation. Other less frequent types of carcinoma are the squamous cell or transitional, the sarcomas and the neuroendocrine tumors [12].

The use of the anatomopathological gradation system described by Donald Gleason in 1966 has been normalized in the last years, mainly because of its recommendation after one conference supported by the WHO [13]. This system assigns a score based on morphological criteria of the tissue architecture that reflects the glandular differentiation grade. The gradation is established from 1 (well-differentiated tumor) to 5 (undifferentiated). As a consequence of the internal heterogeneity on the architecture of these tumors, the Gleason score is obtained as a sum of the values assigned to the two more representative adenocarcinoma cellular patterns in the tissue, the primary pattern and the secondary pattern according to prevalence. Therefore, the final result is included in the interval (2-10) i.e. Gleason1 + Gleason2.

In 2005, the International Society of Urological Pathology (ISUP) carried out the first revision of the classification. In this meeting, the principal recommendations were not to use the score of 1 and 2 in the biopsy. This way, all the biopsies should be scored at least with 3+3, that is the new definition of the “3-pattern”. Another recommendation was the inclusion in the biopsy report of any higher-grade finding, even if it represents only the 5% of the total tumoral volume [14]. As a consequence, the cases nowadays classified as Gleason 6 are the less aggressive ones, fitting better the definition of clinically insignificant carcinomas [15].

The value of the gradation according to the Gleason system is essential for the classification of the patients into different risk groups [16], presenting a clear prognostic meaning. Based on this, the Gleason grade has a big relevance on the survival of the PCa patients. This way, the death risk after 15 years (specific cancer mortality) is very high in patients with Gleason between 7 and 10 (76-93%), moderate in Gleason 6 patients (44%) and low in Gleason lower than 6 (8-14%) [17]. Also, according to the tumoral volume, there exists an important relation with the prognostic of the lesion, considering that the tumors with higher volume than 5 cm<sup>3</sup> present worse stage, higher Gleason grade, higher number of positive surgical margins and higher biochemical relapse [18].

### **Histology: multifocality**

In most of the cases, the prostate carcinoma is a multifocal disease when it is analyzed by radical prostatectomy (RP). The appearance is estimated in the bibliography between 57-91% of the cases [19, 20]. As a consequence of this multifocality, the concept of dominant tumoral lesion (index lesion) has been implemented, defined as the most prevalent lesion according to the tumoral total volume of the prostate and the Gleason grade, which is related to the biological aggressiveness. Once the index lesion is defined, the other ones are considered secondary lesions, and may not represent any life-threatening risk for the patient [21].

### 2.1.3. Diagnosis

#### Classic strategies when dealing with prostate cancer

Today, early diagnosis of PCa is still done after the joint assessment of digital rectal examination (DRE) and the prostate-specific antigen (PSA). During many years, the detection of the prostate carcinoma and its therapeutic guiding was fundamentally based on these two parameters and afterwards, the biopsy [22]. However, it is established that these factors and/or techniques have important limitations.

- The **digital rectal examination** (DRE) is able to detect posterior and lateral tumors in the prostate, theoretically when its diameter is higher than 0,2 cm, but it has several difficulties with lesions located at deep or anterior regions. The DRE has low positive predictive value (PPV) [23]. Also, it presents bias due to repeatability and reproducibility variability as it has important inter and intraexaminer variation [24].
- The **PSA** is a whey protein. It is important to highlight that this is not a cancer specific protein but one from the prostatic tissue. Therefore, it could go up even in benign pathologies such as prostatitis and BPH.

Traditionally, the cut point for defining the test as positive has been 4 ng/ml (based on the classic works of Cooner and Catalona in 1990 and 1991). This value is also established as a reference point from which the biopsy should be done, despite the lack of evidence of considering this point as the optimal one [25]. It is also very relevant to highlight that a serum PSA lower than 4 ng/ml does not imply the absence of the illness. To prove this, numerous publications have shown that up to 32% of patients with positive biopsy have lower than 4 ng/ml levels of PSA and 79% of men with higher than 4,1 ng/ml levels of PSA have not PCa [26]. Thus, the principal problem of PSA is its lack of specificity.

- The **prostate biopsy** (PB) is applied to patients in whom the presence of a carcinoma is suspected. This is essential, not only from the point of view of the confirmation of the diagnosis, but also from the prognostic perspective to reveal, among others, the grade of tumor differentiation (Gleason) [16, 27].

Nowadays, the most applied biopsy method is the systematic transrectal biopsy guided by echography, obtaining at least 12 cylinders of prostate tissue following a fan sampling pattern [28]. However, it has been demonstrated that sometimes PB produces both infrastaging and overstaging of the Gleason grade in comparison with the value evidenced later on pieces obtained by radical prostatectomy (RP) [29, 30]. This discrepancy has been established around 30%, which is traduced in unintentionally wrong applied surgeries [31, 32].

The main limitations of PB are:

- It is not well diagnosed in 20-30% of the clinically significant tumors [33], especially in those located on difficult access zones for biopsy as the apex or the anterior zone (AZ). It must be noted that AZ tumors represent the 25-33% of the PCa in the studies on prostatectomy pieces [10].
- High risk of false negatives (FN): 39-52%. Sometimes it is necessary to biopsy the patient again, which produces discomfort for the patient and an increase of the morbidity [33, 34].
- Often, the PCa is diagnosed on patients with previous negative biopsy and perseverance in the increase of the PSA values [35].
- An important number of non-clinically significant PCa are diagnosed, which leads to overtreatment [36].

There exist another better schemes for PB such as the transperineal biopsy [37]. But, despite the limitations and inconveniences, the systemic endorectal is still nowadays the most widely applied technique for prostate biopsy guided by echography with at least 12 cylinders [28]. The advantages of this technique are basically its lower procedure time, lower cost, the application of local anesthesia, the use of standard equipment and easy-learning operation.

The development of new techniques like radical prostatectomy and radiation therapy are the current curative treatment options for localized PCa. But it also causes secondary effects like non-negligible urinary, sexual, and intestinal morbidity. As a result, the specialists face the dilemma of treating PCa's that would have never caused death, with the added consequence of worsening the quality of life of these patients. Focal therapy is an alternative between active surveillance (stressful for patients) and radical therapy (with their described side effects). This way, by effectively acting on the tumor, the rest of the gland is preserved and the side effects are reduced. Its effectiveness requires accurate information on the location and spread of PCa within the gland (PCa intraglandular map) and the degree of aggressiveness (Gleason). Conventional prostate exams like DRE provide limited information on the PCa intraglandular map.

### **New strategies when dealing with prostate cancer: imaging techniques**

In order to overcome the well-known limitations of the classic invasive techniques based on transrectal biopsy, imaging techniques come up as non-invasive alternatives for detecting and characterizing prostate tumors. Traditionally, imaging techniques have played a minor role in analyzing the PCa. Usually, the only relevant techniques have been the transrectal echography as an image guide of the prostatic biopsy, and the computerized tomography (CT) for general thoracic and abdominopelvic staging, but

with low precision for local staging. Also, the classical magnetic resonance (MR) sequences like T1- and T2-weighted have not been relevant either in the detection of PCa [38]. Therefore, results from conventional MRI T2 do not usually provide enough information for proper guiding of the radiation therapy [39].

Therefore, it is necessary to develop new procedures to accurately detect and locate the tumors [40]. And for this, it is mandatory to understand the nature and behavior of the tumoral processes. Fortunately, in the last decades, the role of MR in PCa has been empowered considerably, especially with the development of surface coils, high-resolution imaging and functional/dynamic techniques. These improvements have allowed detecting and locating the tumor with higher diagnostic precision, as well as a better biological characterization [41]. In recent years, the multiparametric MRI study of the prostate has become the image standard to detect tumors, assess extension and evaluate recurrence, as the European Society of Uroradiology (ESUR) proposed the Prostate Imaging Data and Reporting Structure (PI-RADS) [42] (*see chapter 2.5*). This way, MR and more precisely the perfusion and diffusion techniques, which are the ones selected for the study of the PCa in the present thesis, allow the determination of certain parameters known as imaging biomarkers. An imaging biomarker can be defined as a feature extracted from medical images, which can be measured objectively (gives quantitative information) and behaves as an indicator of a normal biological process, a disease or a response to a therapeutic intervention [43]. This way, they can be used for determining biological properties related to the tumor growth.

## **2.2. Magnetic resonance imaging (MRI)**

MRI is a non-invasive imaging technology that produces three-dimensional detailed anatomical images without the use of damaging radiation. It is used for disease detection, diagnosis, and treatment monitoring. It is based on sophisticated technology that excites and detects the change in the direction of the rotational axis of hydrogen protons found in the water that makes up living tissues.

MRI employs powerful magnets, which produce a strong magnetic field that forces protons in the body to align with that field. When a radiofrequency current is then pulsed through the patient, the protons are stimulated (excitation), and spin out of equilibrium, straining against the pull of the magnetic field. When the radiofrequency field is turned off, the MRI sensors are able to detect the energy released as the protons realign with the magnetic field (relaxation). Both during excitation and relaxation, magnetic gradients are applied in order to locate where the relaxation signal comes from, so that this signal can be spatially codified using small variations in the magnetic field value. This signal location is essential to reconstruct images properly.

The time it takes for the protons to relax, as well as the amount of energy released, changes depending on the environment and the chemical nature of the molecules. For

each biological tissue, this relaxation process is characterized by two times: T1 (longitudinal relaxation time) and T2 (transversal relaxation time). The differences in T1 and T2 are the basis of MRI contrast, so that in the final images the radiologists are able to tell the difference between various types of tissues based on these magnetic properties [44].

To obtain an MRI image, a patient is placed inside the magnet and must remain still during the imaging process in order not to blur the image. A typical MRI study comprises different types of sequences and weightings. Each sequence has a different acquisition configuration, with variations in the intensity and duration of both the radiofrequency pulses and the field gradients, so that each time a set of differences in the tissue magnetic properties are weighted, releasing images with different contrasts (i.e. T1-weighted, T2-weighted, etc.).

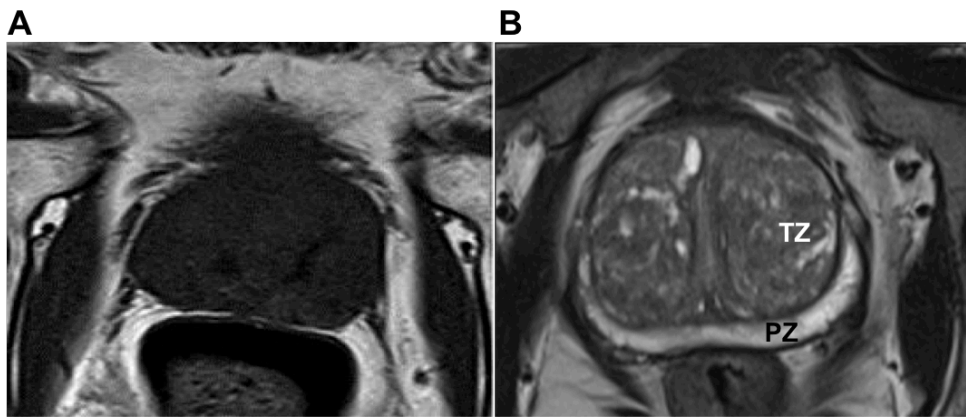
Sequences are often separated in morphologic (high spatial resolution, with excellent detail of anatomic properties) and functional (less spatial resolution and high temporal resolution, with good detail of dynamic physiological process).

### ***2.2.1. Classical morphologic sequences. T1- and T2-weighted sequences***

The most popular morphologic sequences, based on spin echo (SE) or fast spin echo (FSE) acquisitions, are the T1- and T2-weighted.

In the prostate, the T1-weighted sequence is normally performed in an axial plane from the aortic bifurcation to the pubis symphysis. In this sequence, the prostate shows homogeneous middle signal intensity, which cannot discriminate the zonal anatomy (fig. 2). T1 is mainly used for studying pelvic adenopathies, looking for metastasis in the osseous pelvis and detecting possible hemorrhagic changes after biopsy that may hinder the interpretation of the rest of MR sequences [5].

The T2-weighted sequence is normally performed in the three spatial planes due to its higher tissue contrast resolution, containing the prostate and the seminal vesicles. It allows differentiating the zonal anatomy of the prostate: the PZ is normally shown homogeneously hyperintense and separated from the TZ, which is shown heterogeneous and hypointense (fig. 2). However, the CZ and the TZ cannot be distinguished between them. Normally, T2 is only used for an initial exploration of the tumor region and for locoregional staging.



Source: De Visscher P. [45].

**Figure 2. Axial plane of the prostatic gland. A) T1-weighted sequence, showing constant medium signal intensity, cannot discriminate the zonal anatomy. B) T2-weighted sequence allows discriminating the zonal anatomy in two regions, the PZ (homogeneously hyperintense) and the TZ (heterogeneously hypointense).**

### Zonal anatomy in the T2 sequence

MR is considered the best image technique for the study of the prostatic anatomy due to its higher spatial resolution and better contrast of the soft tissues [12]. It is crucial to know the zonal anatomy in order to interpret the MR studies correctly. The characteristics of the MR for each region is described hereafter:

- The PZ presents high signal intensity (due to its composition of ductal and acinars elements with liquid inside) [5]. This hyperintense signal is higher or equal to the signal of the periprostatic fat.
- The CZ presents clearly hypointense signal (due to its major composition of fibromuscular compact stroma).
- The TZ presents hypointense signal (due to its composition of abundant and compact fibromuscular stroma with disperse glandular elements) and cannot be differentiated from the CZ according to its visual appearance. With the presence of BPH it presents an heterogeneous nodular aspect due to the combination of the normal fibroses component of the prostate, which is hypointense in T2, with the adenomatoses nodes of the BPH, that are hyperintense [46]. The shape of the TZ may vary a lot at the adult age regarding to its size and signal heterogeneity, and sometimes can reach huge dimensions, squeezing the PZ.

- The AZ or fibromuscular stroma presents clearly hypointensity as it is composed of fibromuscular tissue. It consists on a band that covers the anterolateral region of the prostate.

The similar signal intensities between the CZ and the TZ make them indistinguishable in MR morphologic imaging. For this reason, they are considered the same region and it is called sometimes “central gland”. However, with the presence of BPH, different signal intensity distribution on the TZ can be observed and differentiated from the CZ signal intensity. Also, it should be highlighted that the term “central gland” referring the combination of the CZ and TZ is just an approximation but it is not a good representation of the zonal anatomy [47, 48].

### **Prostate cancer initial exploration with T2 weighted sequences**

In T2-weighted images, the prostate tumor is identified on the PZ as an area or hypointense node, indicating shorter T2 relaxation time for the tumor than the normal gland, in the hyperintense region of the PZ. However, these images have low diagnostic precision with respect to malignant tumors because the findings in MR can be confused with other non-neoplastic entities like prostatitis, glandular fibrosis, postbiopsy hemorrhage and the post-treatment changes (radiotherapy and hormonotherapy) [49]. Also, the T2 utility for PCa diagnosis is not exempt of errors due to its variation in sensibility and specificity with values around 69-90% according to the literature, and depends on the MR selected criteria and the radiologist experience [38]. Besides, on the TZ, the limitation of this sequence is higher due to the difficulties in the delimitation with precision and in a prospective way of the hypointense zones related to the cancer, in comparison to the normal or hypointense hyperplastic tissue. In this type of sequence, the PCa may be assumed as hypointense nodes in T2 with worse defined limits than the hyperplastic nodes, or maybe as hypointense areas of lenticular morphology [50].

#### **2.2.2. Functional MRI sequences**

Tumors are complex biologic models with intrinsic physiologic characteristics, which cannot be studied objectively using the classical MR sequences [51]. The new development of the functional sequences has allowed studying the physiological and tumor characteristics in a non-invasive way, contributing with additional information for anatomy understanding. This new information is related to two of the main biological indicators of tumor processes, known as vascularization and cellularization. When a group of growing cells presents abnormally high demands of oxygen and nutrients, the tissue responds creating new vessels (angiogenesis) or developing existing ones (neovascularization). On the other hand, the process associated with the increase in cellular density that leads to cell agglomeration in the tissue is called

cellularization. The combination of both processes is what usually determines the presence of an early tumor as first steps in oncogenesis.

In order to improve diagnosis, tracking and tracing of these malignant tumor processes, new MRI techniques have been developed to acquire complementary information to that obtained from conventional MRI, which are not able to discriminate the early tumor regions with precision. Dynamic contrast enhanced-magnetic resonance imaging (DCE-MRI) and diffusion weighted-magnetic resonance imaging (DW-MRI) are the MR functional imaging techniques studied in this thesis [52, 53].

### **2.3. Dynamic contrast-enhanced magnetic resonance imaging (DCE-MRI)**

When studying perfusion, angiogenesis and neovascularization can seldom occur in healthy subjects, but they are strongly present in pathological conditions such as tumors. Thus, the formation of these new and tortuous vessels produces an increase in the blood perfusion. In MRI, these processes can be studied with DCE-MRI [54].

#### **2.3.1. The DCE-MRI acquisition**

In this technique, an exogenous Gadolinium- (Gd) based contrast media is administered intravenously. It diffuses from the capillary network into the extravascular extracellular space (EES), returns to the vascular system and is progressively filtered by the kidneys. The relatively small molecular size of these agents (500–1000 Da) allows them to pass through the vascular endothelium via passive diffusion into the EES of the tissue, establishing a dynamic relationship between the image signal intensity changes and the amount of contrast media that passes and diffuses into a certain tissue.

This sequence requires high temporal resolution but maintaining the spatial resolution in order to detect small variations inside the tissue. This way, the acquisition is normally taken during approximately 5-6 minutes at different evenly- or unevenly-distributed time points. In this thesis, the sequence is acquired during 5.5 minutes at 47 different unevenly-spaced time points.

The capability to analyze tumor angiogenesis in a quantitative and reproducible way from DCE-MR images has important applications to depict and grade tumors and also to evaluate the therapeutic response early after treatment onset [55, 56].

### **2.3.2. DCE-MRI data**

The DCE-MRI acquisition sequence is performed along the volume of the studied organ. Usually, images are acquired at spatial planes corresponding to different slices of the human body (the number of slices depends on the studied organ). The dynamic spectra (s) are then obtained pixel-by-pixel at the considered time points and can be represented in a signal vs time plot (fig. 3).

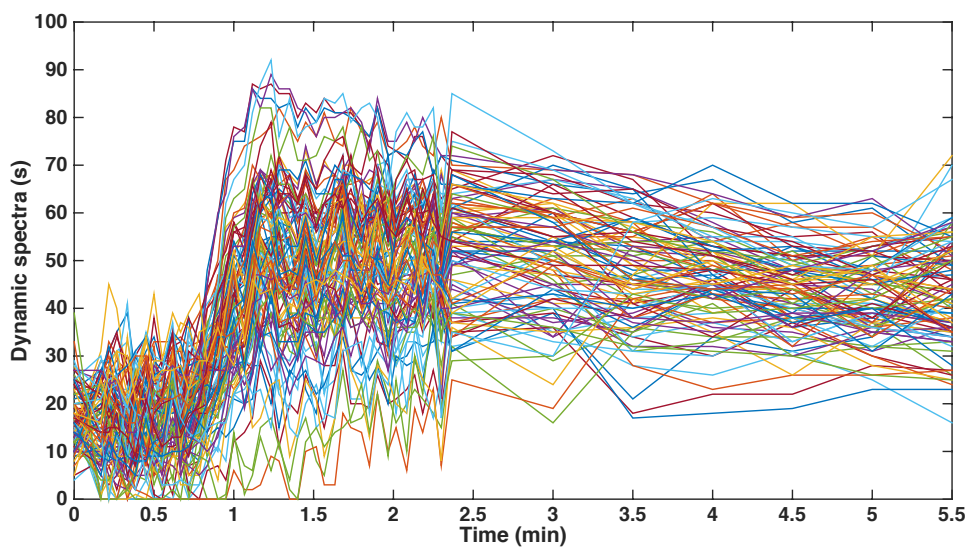


**Figure 3. DCE-MRI dynamic spectra plot (signal intensity vs time). The sequence is acquired at 47 time points (expressed in minutes) during 5.5 minutes.**

From these dynamics, perfusion models are created, which provide relevant quantitative and reproducible information for characterizing tumors or other tissues with pathological changes associated with some microvascular components, by studying the intensity versus time curves (known as enhancement or uptake curve) associated to each pixel of the image. Out of the different approaches proposed to achieve this evaluation, mathematical pharmacokinetic models have become the most popular way due to their ability to provide clinically-oriented biomarkers in tumor analysis [57-59].

### 2.3.3. Pharmacokinetic modeling: theory

Pharmacokinetic modeling of DCE-MR images is based on the application of a mathematical analysis to the enhancement curves on a pixel-by-pixel basis. In these models, compartmental systems have been used to describe tissue dynamics, considering the intravascular (vessels: VS) and the extracellular extravascular (EES) spaces as main compartments in terms of mass exchange. Four different models are considered, divided into two groups according to its complexity. On one hand, one model belonging to the so-called “classical” or “first-generation” models: the Tofts model (or its extended version, i.e. Tofts extended model), and on the other hand the models belonging to the so-called “second-generation” models, the 2-compartment exchange model (2CXM), the adiabatic approximation to tissue homogeneity (AATH) and the distributed parameter (DP) [57, 58].

#### First generation models

Tofts et al. [57] firstly introduced a one-compartment model as a generalization of the Kety model. The mass balance equation can be defined as follows.

$$\frac{dC_t(t)}{dt} = K^{trans} C_{AIF}(t) - k_{ep} C_t(t) \quad \text{Equation 2.1}$$

Where  $K^{trans}$  ( $\text{min}^{-1}$ ) is the volume transfer constant;  $k_{ep}$  ( $\text{min}^{-1}$ ) is the washout constant;  $C_{AIF}$  (mg/ml) is the contrast concentration of the arterial input function (AIF), which describes the contrast agent input to the tissue of interest; and  $C_t$  (mg/ml) is the contrast concentration in the EES.

The extended version of the Tofts’ model consider two different compartments, adding the vascular space ( $v_p$ ) to the contrast exchange:

$$\frac{dC_t(t)}{dt} = v_p \cdot C_p(t) + K^{trans} C_{AIF}(t) - k_{ep} C_t(t) \quad \text{Equation 2.2}$$

Where  $v_p$  is the normalized volume of the vascular space (ml/ml) and  $C_p$  (mg/ml) is the contrast concentration in the plasma space. A scheme is shown in figure 4.

This model assumes that the effect of the vascular tracer can be ignored.  $K^{trans}$  represents the total contrast transference from the plasma space to the EES, whereas  $k_{ep}$  is associated with the washout of the contrast from the EES to the plasma. In this case, the tracer transport is modelled through the EES compartment with normalized volume

( $v_e = K^{trans}/k_{ep}$ ). This model is known as “first-generation” pharmacokinetic model and has been widely applied in oncology for perfusion analysis till the present days.

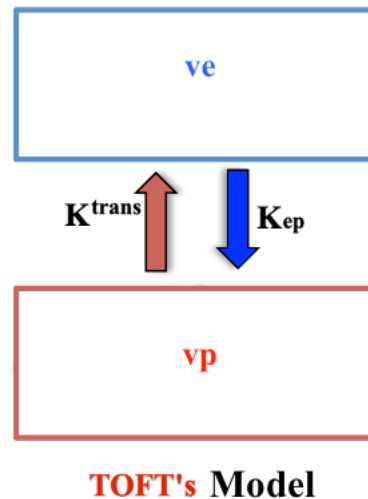


**Figure 4. First-generation model scheme, (Toft’s extended model, the Toft’s simple model does not consider the vascular ( $v_p$ ) space). It shows the mechanism of contrast exchange between the EES ( $v_e$ ) and the vascular space ( $v_p$ ).  $K^{trans}$  is the parameter that represents the exchange from the VS to the EES (contrast captation) and  $k_{ep}$  represents the exchange from the EES to the VS (wash-out).**

### **Second generation models**

However, the development and evolution of MRI hardware has provided an improvement in image quality and pixel resolution that exposes the limitations of the classical models. This allows developing new approaches designed to overcome the limitations of ‘classical’ models to obtain additional and more accurate information about the tissue. The most important models are the 2CXM, AATH and the DP model [58]. These new approaches are known as “second-generation” models and a scheme is shown in figure 5.

The main advantage of second-generation models is the possibility of measuring the plasma flow ( $F_p$ ) separately from the capillary permeability-surface area product (PS) rather than a single parameter ( $K^{trans}$ ), whose physiological meaning represents a combination of  $F_p$  and PS. The separation of both phenomena allows a better understanding of perfusion behaviours in tumors.

Second-generation models are bicompartamental. In this way, the EES ( $v_e$ ) and plasma space ( $v_p$ ) can be used undivided or be further divided into infinitesimal subcompartments according to the model scheme (fig. 5). The notation is defined as follows:  $v_p$  (ml/ml) is the normalized volume of the plasma space;  $v_e$  (ml/ml) is the normalized volume of the EES;  $C_p$  (mg/ml) is the contrast concentration in the plasma space;  $C_e$  (mg/ml) is the contrast concentration in the EES;  $F_p$  ( $\text{min}^{-1}$ ) is the plasma flow;  $PS$  ( $\text{min}^{-1}$ ) is the permeability-surface area product;  $E$  (%) is the extraction fraction; and  $L$  (mm) is the distance between the first and last subspace.

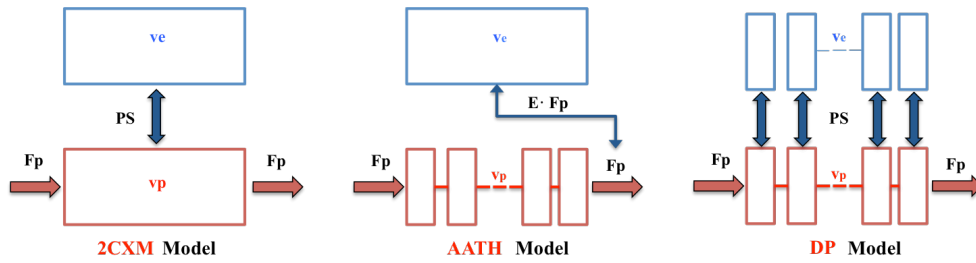


**Figure 5. Second-generation models scheme, (left to right: two-compartment exchange model, 2CXM; adiabatic approximation of tissue-homogeneity, AATH; distributed-parameter, DP) sorted in terms of complexity attending to the number of compartmental divisions.**

In the same way as the Tofts model, mass balances can be applied to the different compartments for tissue modelling, depending on the corresponding complexity. 2CXM is the simplest of the second-generation models, where both spaces are undivided.

$$v_p \frac{dC_p}{dt}(t) = F_p \cdot C_{AIF}(t) - F_p \cdot C_p(t) + PS \cdot C_e(t) - PS \cdot C_p(t) \quad \text{VS balance Equation 2.3}$$

$$v_e \frac{dC_e}{dt}(t) = PS \cdot C_p(t) - PS \cdot C_e(t) \quad \text{EES balance Equation 2.4}$$

The next one is the AATH model, where the plasma space is divided in infinitesimal subcompartments and it is assumed that the permeability contrast transference is produced at the end of the vessels (the last plasmatic compartment).

$$\frac{v_p}{L} \frac{\partial C_p}{\partial t}(x, t) = -F_p \frac{\partial C_p}{\partial x}(x, t) \quad \text{VS balance Equation 2.5}$$

$$v_e \frac{dC_e}{dt}(\mathbf{t}) = E \cdot F_p \cdot C_p(\mathbf{L}, \mathbf{t}) - E \cdot F_p \cdot C_e(\mathbf{t}) \quad \text{EES balance Equation 2.6}$$

Finally, in the DP model both compartments are divided into infinitesimal spaces and the contrast transference due to permeability (PS) is assumed constant along the system.

$$\frac{v_p}{L} \frac{\partial C_p}{\partial t}(\mathbf{x}, \mathbf{t}) = -F_p \frac{\partial C_p}{\partial x}(\mathbf{x}, \mathbf{t}) + \frac{PS}{L} C_e(\mathbf{x}, \mathbf{t}) - \frac{PS}{L} C_p(\mathbf{x}, \mathbf{t}) \quad \text{VS balance Equation 2.7}$$

$$\frac{v_e}{L} \frac{\partial C_e}{\partial t}(\mathbf{x}, \mathbf{t}) = \frac{PS}{L} C_p(\mathbf{x}, \mathbf{t}) - \frac{PS}{L} C_e(\mathbf{x}, \mathbf{t}) \quad \text{EES balance Equation 2.8}$$

These systems of partial differential equations can be solved analytically expressing the contrast concentration  $C(t)$  as a convolution product of the  $C_{AIF}$  and the  $R(t)$  function, which is the solution of the mass balances [58]. These contrast concentrations  $C(t)$  can be directly obtained from the signal intensity  $I(t)$  using a direct conversion based on relaxivity and field strength, being  $I(t)$  the intensity of each pixel at each time point.

$$C(\mathbf{t}) = (C_{AIF} * R)(\mathbf{t}) \quad \text{Equation 2.9}$$

In this expression (eq. 8),  $R(t)$  only depends on the first ( $K^{trans}$ ,  $k_{ep}$ ,  $v_e$ ) or second ( $F_p$ ,  $PS$ ,  $v_e$ ,  $v_p$ ) generation perfusion parameters (biomarkers) at each time instant ( $t$ ).

For example, the solution of the convolution product for Toft's model [57], which is one of the simplest pharmacokinetic models, is presented in equation 9:

$$C(\mathbf{x}, \mathbf{y}, \mathbf{t}) = K^{trans} \int_0^t C_{AIF}(\tau) e^{-k_{ep}(t-\tau)} d\tau \quad \text{Equation 2.10}$$

In order to obtain these biomarkers, the models need as input the reference of an appropriate arterial input function ( $C_{AIF}(t)$ ) obtained from the tumor-feeding artery [60-63]. This function is a time-varying curve with a specific dynamics pattern, comprising a baseline, an abrupt positive peak, and a fast decay or washout. These curves are usually extracted by manually placing ROIs in the artery (i.e., one of the iliac arteries for the prostate) and the tissue of interest. But this approach introduces a user-dependent bias into the analysis since the accuracy in the computation of the

biomarkers depends on the proper determination of the  $C_{AIF}(t)$ : the higher the uncertainty in the determination of the  $C_{AIF}(t)$ , the higher the uncertainty in the estimation of the pharmacokinetic parameters.

One alternative to the manually determined artery ROI location is the application of a latent variable based model like Principal Component Analysis (PCA) [64], selecting the pixels related to the arterial dynamic pattern [65]. This fast and objective AIF determination approach is also patient-focused, hence resulting in major benefits related to radiologist time, reproducibility, and personalized medicine.

#### ***2.3.4. Imaging biomarkers calculation (Pharmacokinetic modeling)***

Once the  $C_{AIF}$  has been calculated for each patient individually, the perfusion sequence is analyzed pixel-by-pixel applying the different pharmacokinetic approximations.

The biomarkers are calculated using non-linear optimization algorithms. For this purpose, the values of these biomarkers are evaluated in order to minimize, for each model at each pixel, the difference between the contrast measured concentration and the convolution product function:  $(C_{AIF} * R)(t)$ . Note that non-linear optimization can only provide local optima. So, in order to obtain reliable results, the optimization method defines different starting points and selects the best result minimizing the Residual Sum of Squares (RSS) evaluated as the sum of the squared differences at each time point. Using this technique, the probability of obtaining the global optimum is higher as the number of starting points increases, testing a relatively high number of “starting points” in the variable space.

Following the optimization method, 3 biomarkers are obtained in the case of the Toft’s model ( $K^{trans}$ ,  $k_{ep}$ ,  $v_e$ ) and 4 when considering second-generation models ( $F_p$ ,  $PS$ ,  $v_e$ ,  $v_p$ ). It must be strengthened, however, that these pharmacokinetic models assume some a priori knowledge about the dynamics followed by the tissues. Nevertheless, it is possible that, when the tissue starts producing new vessels and tissue structures in a chaotic way, the dynamics do not behave as expected. Therefore, it seems necessary to establish some parameter in order to evaluate the goodness of fit of the dynamic behaviors, to evaluate the reliability of the obtained biomarkers. However, in clinical practice, the values of the biomarkers are normally obtained without any information of this fit and applied directly for tumor diagnosis and/or prognosis. In order to tackle this issue, this thesis introduces the use, not only of these biomarkers, but also of the Residual Sum of Squares (RSS) as a complementary biomarker (parameter), which provides information about how well the pixel is fitted by the assumed model, measuring the disagreement between each voxel behavior and its prediction from the assumed model. By computing and storing the RSS, this method not only helps in determining the value of the biomarker but also its reliability.

## **2.4. Diffusion-weighted magnetic resonance imaging (DW-MRI)**

Diffusion [66] is a physical process that occurs due to the thermal agitation of the water molecules inside the human body. These translational displacements depend, among other factors, on the tissue structure according to the cellular organization. In normal conditions, the prostatic gland presents an extremely ramified ductal structure. But in the presence of PCa, numerous groups of agglomerated cells are formed, leading to an increase on cellularity with rests of necrosis and fibrosis, all reducing the mobility of water molecules. When the tissue is highly cellularized, the water molecules have more restrictions to movement due to a decreased interstitial space and a higher number of cell membrane interfaces. However, when the tissue is highly vascularized, molecules are in a non-restricted high-velocity environment within the vessels, and the spatial movements are possible in all directions, as the prostate can be assumed as an isotropic tissue (the diffusion is the same regardless of the direction). This assumption can be considered correct because, in spite of being a microductal structure, there are not preferential diffusion directions inside the prostate gland (the extremely complex ductal structure can be considered as a homogeneous tissue).

The diffusion process can be evaluated with DW-MRI. This non-invasive technique provides high-resolution images that are sensitive to water molecules movement inside the tissues.

### **2.4.1. The DW-MRI acquisition**

The diffusion sequence is an adaptation of a spin echo sequence T2 weighted. It has to be acquired with a long enough echo time in order to perform two gradient pulses during the acquisition. As a consequence, the intensity of the resultant signal in a pixel that contains free movement protons is equal to the signal of a T2 weighted image. This signal, associated to the diffusion value on that pixel, is then reduced progressively according to a factor (b-value [40]).

The most widely used sequence is the ultrafast SE based on the echo planar imaging (EPI) of the  $k$  space with parallel image acquisition. It consists on the application of an initial radiofrequency (RF) pulse of  $90^\circ$  and then, a counter pulse of  $180^\circ$  [67]. The applied gradients are bipolar, as the pixel signal loss during their application is only due to the movement of the hydrogen nucleus of the water. Besides, the presence of a magnetic gradient in a pixel creates, by its own, a signal fall due to the presence of different magnetic fields on both edges of the pixel, causing a greater gap and, in consequence, an inherent fall of the signal. In order to obtain a signal that depends only on the molecules movement avoiding the gradient gap caused on the static nucleus, bipolar gradients should be used [68].

For the diffusion-weighted acquisition, after applying the  $90^\circ$  RF pulse of the SE sequence, two new pulses of a fixed value  $G$  will be added. This consists on one pulse

previous to the  $180^\circ$  RF pulse and another one, symmetric to the first one, after the  $180^\circ$  RF pulse (fig. 6). According to this, in the diffusion image, immediately after a pulse, the molecules of a volume are in the same phase. Thus, when a gradient is applied to that volume, the molecules are dephased differently depending on where they are. Afterwards, if another opposite gradient of the same magnitude is applied, only those protons that have not moved at all (restricted diffusion) will come back to the same phase. By contrast, the molecules with higher mobility will not recover their phase completely after the second pulse application [69, 70].

The complete sequence of pulses in figure 6 is well known as the Stejskal-Tanner sequence. Here, two gradient pulses are performed symmetrically around of the  $180^\circ$  pulse of the base sequence, separated by a time interval  $\Delta$ . The duration of the gradient pulses is adjustable by a parameter called  $\delta$  [69].

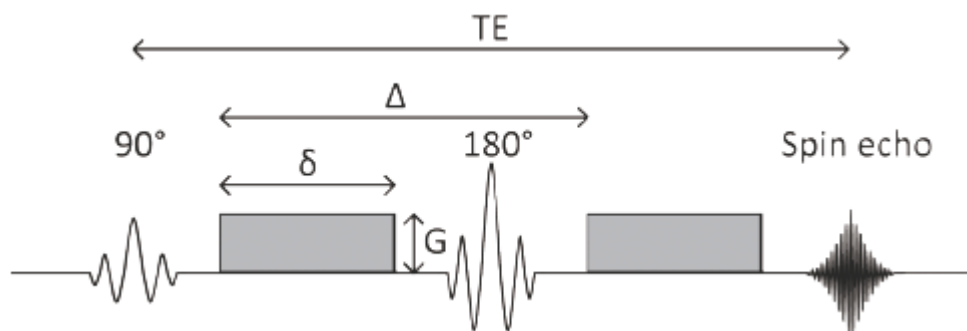


**Figure 6. Pulse sequence Stejskal-Tanner diagram for the calculation of molecular diffusion with MR.**

The differences between tissues can be appreciated by applying this sequence:

On one hand, in the restricted mobility tissues, i.e. those considered highly cellular, the water molecules barely move. In this kind of tissue, the second pulse cancels the application of the first gradient. As a result, there is not significant signal loss and the T2 signal is basically maintained. In other words, the low mobility of the molecules is shown as a high signal in the diffusion-weighted images.

On the other hand, in the non-restricted mobility tissues (low cellularization), the molecules travel relatively long distances during the application of both gradients. As a consequence of these longer distances, the molecules cannot recover the phase after the application of the second gradient. As a result, a signal loss reducing the tissue signal intensity of the T2-weighted is observed. In other words, the higher mobility regions are shown in the diffusion-weighted images as a loss of signal.

Depending on the configuration of the MR equipment and based on the duration and the amplitude of the applied magnetic field gradient, image acquisition is associated to the b-value [40]. The selection of a proper b-value highly influences the resulting images, as it is the responsible of the diffusion weighting. The b-value can be expressed as follows:

$$b = \gamma^2 \cdot G^2 \cdot \delta^2 \cdot \left( \Delta - \frac{\delta}{3} \right) \quad \text{Equation 2.11}$$

Where G is the gradient amplitude,  $\gamma$  is the gyromagnetic proton constant,  $\delta$  is the duration of the gradient pulse and  $\Delta$  is the application interval between the gradient pulses.

The signal of the image decreases with the increase in the b-value acquired. This attenuation (loss of signal) depends on the characteristics of the tissue, being stronger if the tissue is vascularized and much more moderate if it is highly cellular. The range of different signal attenuations between these two types of tissue at the same b-value is the basics to study the different behaviors in the diffusion process.

#### **2.4.2. DW-MRI data**

The DW-MRI acquisition sequence is performed, as in perfusion, along the volume of the studied organ. In this case, for each slice, images are taken with different b-values. This way, a signal spectrum  $s$  is extracted from each pixel of the image (figure 7), associated to the different b-values. The number of b-values varies among clinical studies, reaching up to 10 values for the clinical setting [71]. In this thesis, the sequence has been acquired at 6 different b-values (0, 50, 200, 400, 1000, 2000)  $\text{sec}^2/\text{mm}$ .

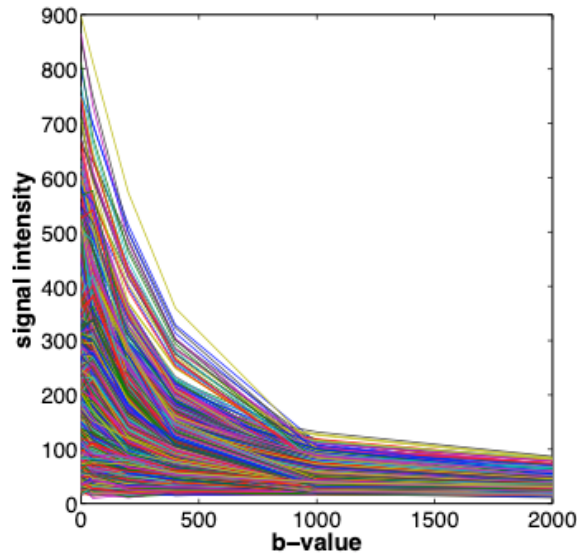


Figure 7. DW-MRI spectra plot (signal intensity vs b-value). The sequence is acquired at 6 different b-values (ranging from 0 to 2000 s/mm<sup>2</sup>).

#### 2.4.3. Exponential modeling: theory

In order to model the signal decay of the diffusion process, spectra can be fitted with different expressions.

For those based on the decay of the signal as a function of the b-value (like the prostate tissue), the most widely used is the monoexponential model (described by Stejskal and Tanner [72]), whose associated parameter, the apparent diffusion coefficient (ADC) integrates the global effect of the slow displacements (intracellular and interstitial) as well as fast movements due to extravascular diffusion:

$$\frac{s}{s_0} = e^{-b(ADC)} \quad \text{Equation 2.12}$$

Where  $s_0$  is the initial value of the signal when the b-value equals zero. The ADC values express the average distance that the water molecules cover within a pixel at a certain time. It is related with the cell density, the permeability of the membranes and the tortuosity of the intercellular interstitial space. It is called “apparent” because it reflects several different mechanisms, as it is a combination of the two phenomena expressed before:

1. The movement associated to the water molecules (Brownian movement), known as slow diffusion (cellular tissue).
2. The intravascular movement in the microcapillaries vessels, known as fast diffusion or pseudo-perfusion (vascularized tissue).

Fast diffusion may produce an overestimation of the real diffusion values if not properly considered. The principal problem is that the monoexponential model does not take into account the different mechanisms of the diffusion process. Currently, one way of dealing with this problem is by using a two-exponential model, known as intra-voxel incoherent motion (IVIM) [73]. This is a more complex model that considers two behaviors, slow and fast diffusion, weighted by a parameter called vascular fraction ( $f$ ), which relates to the proportion of vascular tissue in a pixel. This model is able to separate these two effects from the signal decay in the pixel with increasing values of  $b$  [67]. This way, it is possible to quantify and segregate the slow diffusion (real diffusion), due to extravascular spread (cellularization); from fast diffusion (pseudo-perfusion), due to vascularization. This helps in a more accurate detection of tumors, since they are related to low-real diffusion values and higher pseudo-perfusion values. The expression of the IVIM model is shown below:

$$\frac{s}{s_0} = (1 - f)e^{-bD} + f e^{-b(D+D^*)} \quad \text{Equation 2.13}$$

The spectra are normalized with  $s_0$  as in the monoexponential approach. Three different parameters must be estimated: the diffusion coefficient ( $D$ ), the pseudo-perfusion coefficient ( $D^*$ ) and the vascular fraction ( $f$ ). This way, the normalized signal  $s/s_0$  is modeled as a weighted average of the slow diffusion (water movement inside the cellular tissue, characterized by  $D$ ) and the fast diffusion (water movement inside the vascular tissue, characterized by  $D + D^*$ ). The slow diffusion behavior is weighted by the non-vascular fraction ( $1-f$ ) related to it, and the fast diffusion term by the corresponding  $f$  vascular fraction, since the major contribution of this phase (in the order of 10 times higher) is from  $D^*$  if compared to  $D$ ; however this last parameter is not so low to be obviated. Despite the fact that the IVIM model is theoretically more appropriate according to physiological criteria, the monoexponential model is, nowadays, the most widely used in medical practice due to its simplicity.

#### **2.4.4. Imaging biomarkers calculation (exponential modeling)**

As stated in the perfusion section (*see chapter 2.3.4*), diffusion biomarkers are also obtained by using non-linear optimization methods minimizing the residual sum of squares (RSS). In this case, only one biomarker is considered for the monoexponential

model (ADC) and three ( $f$ ,  $D$  and  $D^*$ ) for the IVIM model. However, the IVIM model can also be calculated directly, avoiding optimization methods, by applying a two-step constrained analysis “segmented” approach, which is an alternative route for reducing measurement error [74]. In this thesis, the segmented approach was applied to speed-up the calculations without losing accuracy. The comparison between methods was performed previously to the analysis (results not shown). At the end of the process, the RSS is included in this thesis as an additional biomarker for the same reasons explained in the perfusion section.

## **2.5. Multiparametric MRI: PI-RADS and imaging biomarkers limitations**

Once the perfusion and diffusion techniques are explained, we can define the combined analysis of morphological MR sequences with one or more of the functional sequences (perfusion, diffusion) as multiparametric MR imaging (mp-MRI). Current clinical practice follows a set of rules to detect and characterize prostate tumors, known as Prostate Imaging Reporting and Data System (PI-RADS). In the original PI-RADS, a suspicion score for the presence of clinically significant cancer was assigned on 5-point scale to characterize prostate lesions, ranging from 1 (most probably benign) to 5 (most probably malignant) on each mp-MRI sequence (T2w, DW-MRI, DCE-MRI) based on subjective criteria. In addition to detailed recommendations on integrating mp-MRI scores according to prostate zonal anatomy (Table 1), the updated PI-RADSv2 [42], published in 2015, also suggested a simplified approach for the DCE-MRI interpretation scheme (dichotomous positive or negative instead of the 1–5 scale suggested in PI-RADSv1), and included a pathologic definition of clinically significant prostate cancer, which should be used for comparison to mp-MRI.

**Table 1. Integration of MRI scores from T2-weighted images (T2W), Diffusion-weighted images (DWI), and dynamic contrast-enhanced (DCE) images from the prostatic peripheral zone (PZ) and transition zone (TZ) recommended by PI-RADS v2 [42]. “Any” indicates 1-5.**

Peripheral Zone (PZ)				Transition Zone (PZ)			
DWI	T2W	DCE	PIRADS	T2W	DWI	DCE	PIRADS
1	Any*	Any	1	1	Any	Any	1
2	Any	Any	2	2	Any	Any	2
3	Any	-	3	3	$\leq 4$	Any	3
		+	4		5	Any	4
4	Any	Any	4	4	Any	Any	4
5	Any	Any	5	5	Any	Any	5

Source: Vargas et al [75].

Despite several efforts to include quantitative measurements (imaging biomarkers), most radiologists continue to rely on qualitative criteria, either because of lack of evidence, difficult access to state-of-the-art software tools or professional inertia. As a result, PI-RADS staging has important drawbacks related to inter- and intra-subject interpretation, based on expert opinion and it also requires evidence-based support and refinement. Besides, although imaging biomarkers have not yet been incorporated in PI-RADS, it is expected that future versions will include them, considering the growing accumulated evidence.

As mentioned before, the imaging biomarkers can be interpreted as spatially-distributed characteristics and parameters extracted by functional MRI sequences [52, 54]. However, analysis of imaging biomarkers poses different problems:

- Imaging biomarkers are obtained in a univariate way by fitting MR signals to some mathematical models, not taking advantage of the internal correlation structures between pixels.
- The simultaneous evaluation of several biomarkers is difficult, even more when considering the different combinations that may be related to a tumor. This can be complicated and require “a priori” knowledge.
- The types of biomarkers to analyze depend on the structure of the studied organ (prostate, breast, brain, etc.).
- Some of the obtained parameters (e.g., the transfer coefficient of  $K^{\text{trans}}$ ) have a complex physiological interpretation [76], since it mixes

permeability and vascular flow. Therefore, it seems interesting to obtain biomarkers having an easier clinical interpretation.

- Also, these biomarkers may suffer from bias in their estimation due to measurement errors introduced by the different artifacts and/or reproducibility errors associated with the values of some model input function (e.g., the AIF).

Likewise, there are different models of different grades of complexity both for perfusion and diffusion. Such models are justified in certain cases (e.g., exponential-based in diffusion). However, it should be highlighted that the IVIM model is not a classic biexponential model because the two exponential decays are not independent as they are complementary weighted by the vascular fraction,  $f$ . Furthermore, the normalization of the spectra (dividing by  $s_0$ ) causes a distortion, modifying the shape of the original curve (fig. 8 (A)) and decreasing the signal-to-noise ratio (as can be seen in figure 8 (B)). Thus, this standardization reduces the variability range masking the different behaviors present in the signal decays. In other cases (e.g., second generation pharmacokinetic models [57]) the complexity has not yet been justified. Therefore, it becomes necessary to have models able to extract such a priori knowledge from data directly extracted from the sequences.

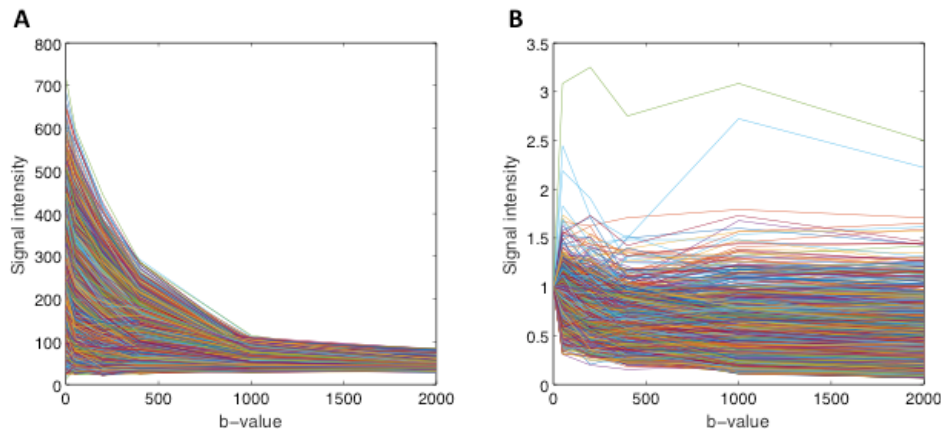


**Figure 8. Signal attenuation spectra in a DW-MRI case. (A) Before normalization. (B) After normalization.**

In addition to these last points, the “a priori” knowledge about the correlation between biomarkers (combinations of values between them) when determining the existence of a tumor may not be enough, since there may be other combinations that also lead to the detection of a tumor; thus resulting in false negatives, i.e. non-detected tumors. This

possibility increases with the number of biomarkers.

All these limitations cause difficulties when doing the calculations and interpretation of the results provided by these parametric models, what has limited their applicability and widespread use in clinical practice, as it is difficult to obtain a validation and standardization of the parameters that ensure reproducibility among different studies.

One possible way to improve the interpretation of these functional sequences is by applying multivariate statistical projection models to the DCE-MRI and DW-MRI data. In image analysis, the application of these statistical models is known as Multivariate Image Analysis (MIA) [77,78], based on latent variables models such as Principal Component Analysis (PCA) [79], Multivariate Curve Resolution (MCR) [80-82], or Partial Least Squares (PLS) [83-84].

## **2.6. Multivariate image analysis and its application to oncology**

The main characteristic of MIA is the capability to study the whole set of pixels at the same time by extracting the sources of variation caused by the latent structures present in the images. Applying MIA to oncology [85] allows extracting the sources of variation from a relevant number of time-sequenced images from different individuals, providing new statistical models that help explaining the perfusion differences between healthy and cancer-affected tissues. MIA can also be applied with segmentation and classification purposes, as in Gurjal et al. [86], as well as for segregating between healthy and diseased livers [87], showing the potentials of the technique.

Also, by using MIA, the multivariate model might describe the dynamics even better than the mathematical (clinical) imposed model, better pointing out to the pixels of interest for improving the model. This might be due, at least partially, to the fact that the wealth of physiological and pharmacokinetic assumptions likely oversimplifies an exceptionally complex system [85], varying from patient to patient.

The main and most widespread MIA tool is PCA [79]. However, two problems arise when PCA is applied on DW-MRI data:

- No prior information can be included in the model.
- The orthogonality of the principal components is a limitation to model the different diffusion behaviors that are not necessarily orthogonal.

In order to overcome these drawbacks, it is possible to use more flexible models, as is the case of Multivariate Curve Resolution (MCR) [80-82]. This model does not impose these types of restrictions, but others related to some a priori knowledge, when available; hence being able to provide more clinically (or physiologically) interpretable results. Applications of MCR models on biomedical images can be found in [88-91].

In the next chapter, the materials (patient database) and methods (MIA most relevant tools and an image registration technique) used for studying the prostate cancer with MR imaging will be described.



# Chapter 3

## Materials and methods

### 3.1. Materials

In this thesis, the patient database consisted of 55 histologically-confirmed cases of peripheral prostate tumors and 11 healthy cases that do not present any type of tumor. DCE-MRI, DW-MRI sequences are acquired in all cases, ensuring full prostate coverage (12 to 16 slices) by using an in-plane resolution of  $192 \times 192$  voxels, each one measuring  $1.5625 \times 1.5625 \times 4 \text{mm}^3$ . DCE-MRI and DW-MRI sequences are acquired during 47 time points (acquisition time 5 min) or 6 different b-values (0, 50, 200, 400, 1000, 2000)  $\text{sec}^2/\text{mm}$  respectively. Besides, morphologic T2w images are also acquired covering full prostate volume (25 slices) by using an in-plane resolution of  $512 \times 512$  voxels, each one measuring  $0.4883 \times 0.4883 \times 3 \text{mm}^3$ . The data is arranged in a 4D (or 3D when considering T2w images) structure for each patient individually, and refolded into a bidimensional structure.

In perfusion, images are taken with different time points and a 4D data structure is organized as follows: the spatial two-dimensional image ( $x \cdot y$ ), the  $z$  dimension associated to slice number in the axial direction of the body (starting from the top), and the temporal dimension ( $t$ ).

For each slice (keeping  $z$  constant), the 4D structure can be separated in  $z$  3D structures. One specific case for  $z_1$  is showed in figure (9, A).

Being  $t$  the total number of time points and  $z$  the total number of slices. Considering the

3D matrix, each pixel of the image can be expressed as a dynamic spectrum with an intensity value associated to each time point. This way, the 3D matrix is refolded into a 2D matrix where the pixels are located in rows and the different time points in columns, rearranging the whole slice image and obtaining the structure showed in figure (9, B).

Finally, each row of the 2D can be plotted versus time in a bi-dimensional graph obtaining the dynamic spectra. Figure (9, C) represents the group of spectra related to one slice of the organ (each dynamic spectrum corresponds to one row of the 2D matrix). This way, a signal dynamic spectrum  $s$  is extracted from each pixel of the image, associated to the different time points.

In diffusion, the unfolding procedure is performed the same way as in perfusion (fig. 10). The only difference is to change the functional dimension, using b-values instead of time.

Furthermore, since it is necessary to analyze the whole organ volume, each slice ( $z$ ) (following the transverse plane of the body) needs to be stacked one below the other, forming the data structure shown in figure 11.

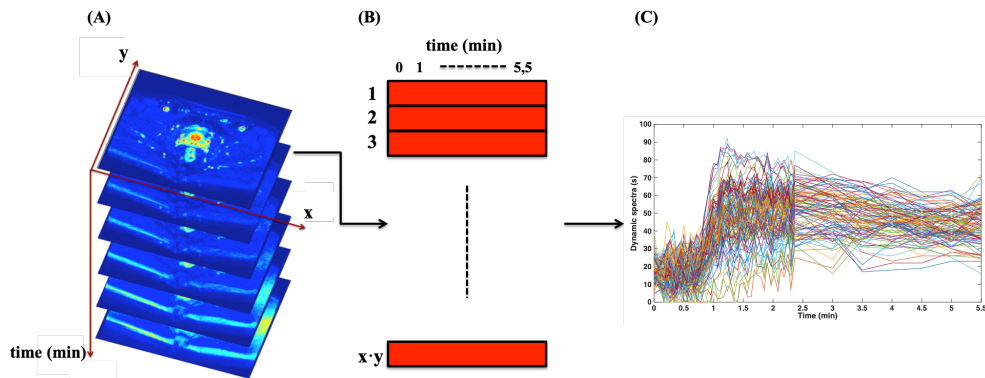


**Figure 9. (A), 3D data structure for a specific slice of one case of DCE-MRI;  $x$  and  $y$  are the spatial resolution of the image,  $t$  is the number of time points for perfusion. (B), Unfolded 2D matrix considering slice 1 ( $z_1$ ). (C), Dynamic spectra evolution along time, showing signal intensity for a specific slice of the prostate.**

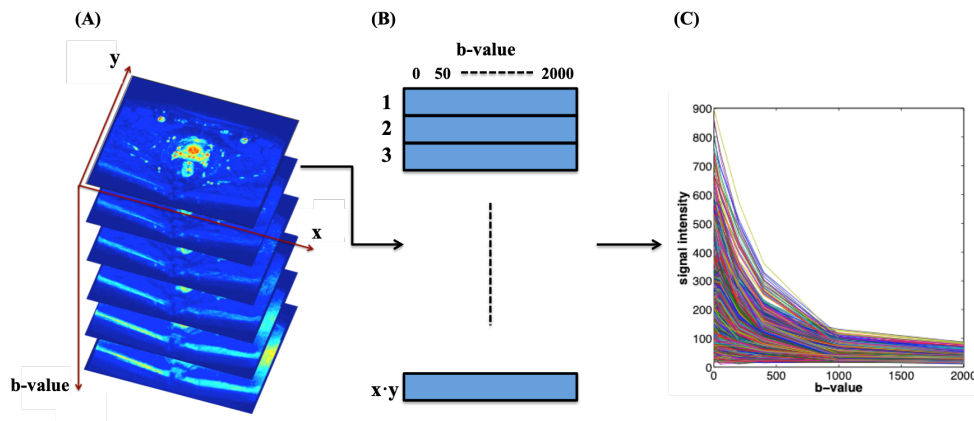


Figure 10. (A), 3D data structure for a specific slice of one case of DW-MRI;  $x$  and  $y$  are the spatial resolution of the image,  $b$ -value corresponds to the images obtained at each value of  $b$ . (B), Unfolded 2D matrix considering slice 1 ( $z_1$ ). (C), Spectra evolution along the value of  $b$ , showing signal intensity for a specific slice of the prostate.

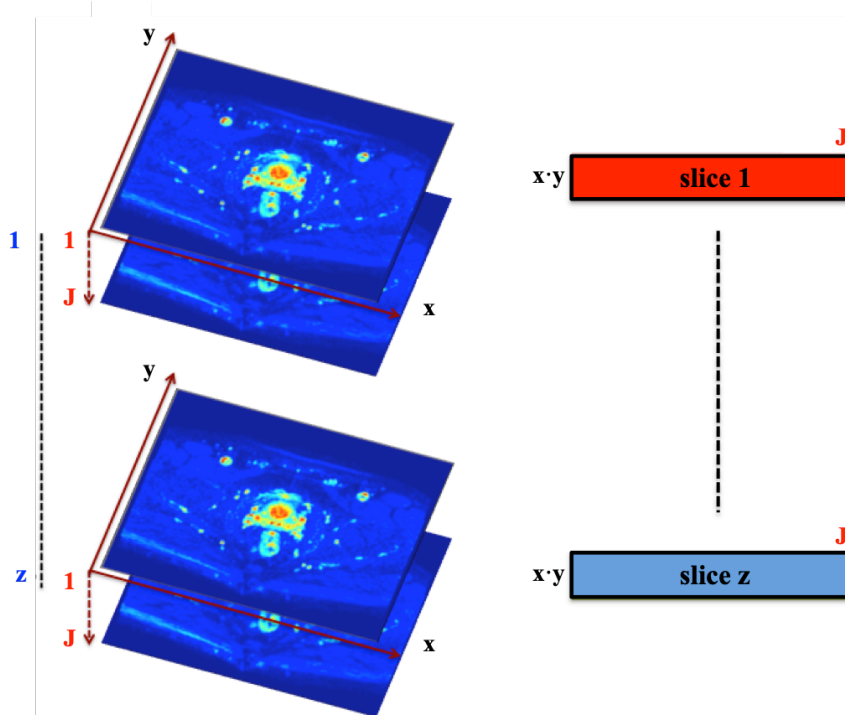


Figure 11. Data structure for MCR analysis. Images are  $x \cdot y$  pixels size,  $J$  is the number of  $b$ -value or time points (diffusion or perfusion respectively),  $z$  is the number of slices. The 2D unfolded matrix dimensions are  $((x \cdot y \cdot z)) \cdot J$

DCE-MRI and DW-MRI data structures are used in *chapter 4* for developing the MCR-based imaging biomarkers.

Also, reference tumor and control regions of interest (ROIs) have been manually segmented for the peripheral zone of the prostate. Considering biopsy location and image findings, the prostate cancer is evaluated by using the PI-RADSv2 [42] reporting scheme, defining two different types of ROIs:

- DL: Dominant Lesion, related to carcinogen tissue at the peripheral prostate zone (PI-RADS $\geq$ 4).
- HP: Healthy Peripheral, related to healthy tissue at the peripheral prostate zone (PI-RADS=1).

These ROIs are manually defined by radiologists, considering the PI-RADS score and the biopsy result, and are used as the gold reference for tissue classification in *chapter 5*. Besides, it is assumed that the behaviour of the healthy regions on the peripheral zone of the gland has no significant differences between cancer and healthy patients [92]. Therefore, it can be safely used as a healthy tissue reference.

For studying aggressiveness, only affected regions (DL ROI's) are considered. For this purpose, selecting a regularized indicator of the level of malignancy is required: the Gleason score (*Chapter 2.1.2*). In this case, the Gleason is used to separate the lesions into two categories:

1. Low aggressiveness (LA): Gleason  $\leq$  6.
2. High aggressiveness (HA): Gleason  $\geq$  7.

Since no healthy ROI's is used in this work, for the analysis, a ROI classified as LA is considered a **positive** and a ROI classified as HA is considered a **negative**.

All patients gave consent for using their medical images, which were anonymized before post-processing. The local Ethics Committee approved the study protocol.

## **3.2. Statistical models**

In this section the most relevant multivariate statistical methods applied in this thesis are presented (i.e., PCA [79] MCR-ALS [80-82], PLS regression [83, 84] and SMB-PLS [93-95]).

### **3.2.1. PCA**

Principal Component Analysis (PCA) [79] is a multivariate statistical projection method that allows compressing the information of a data matrix  $\mathbf{X}$  into a reduced

number of uncorrelated (orthogonal) components known as “latent variables” (LV). This is performed by means of a linear decomposition of the  $\mathbf{X}$  matrix:

$$\mathbf{X} = \mathbf{T} \cdot \mathbf{P}^T + \mathbf{E} \quad \text{Equation 3.1}$$

Where  $\mathbf{X}$  is the data matrix organized by individuals in rows and variables in columns,  $\mathbf{T}$  is the score’s matrix and  $\mathbf{P}^T$  is the loading’s matrix and  $\mathbf{E}$  gathers the residuals.

### 3.2.2. MCR-ALS

Multivariate Curve Resolution-Alternating Least Squares (MCR-ALS) is an algorithm that fits the requirements for image analysis when physico-chemical, physiological or other type of “real phenomena” interpretation is the prior relevance [81, 96-98]. This method decomposes the original raw image following the Beer-Lambert bilinear model:

$$\mathbf{S} = \mathbf{C} \cdot \mathbf{D}^T + \mathbf{E} \quad \text{Equation 3.2}$$

Where  $\mathbf{S}$  is the signal unfolded image,  $\mathbf{D}^T$  is the matrix of pure dynamic behaviors and  $\mathbf{C}$  gathers the relative contribution of each modeled behavior. This notation is not the commonly used in MCR, where  $\mathbf{D}$  usually relates to the data matrix and  $\mathbf{S}$  to the “pure spectra”.

To perform the decomposition, the original 3D image needs to be unfolded into a data table with the spectral channels of all pixels one below the other. The spatial structure of the image is recovered after the resolution process by folding back the concentration profiles into the higher dimensional spatial ordering (these plots are known as “distribution maps”). Regarding the algorithm, MCR-ALS is an iterative method that performs the decomposition into the bilinear model  $\mathbf{S} = \mathbf{C}\mathbf{D}^T$  by means of an alternating least squares optimization of the matrices  $\mathbf{C}$  and  $\mathbf{D}^T$  according to the following steps:

1. Determination of the number of compounds in the raw image,  $\mathbf{S}$ .
2. Generation of initial estimates (e.g.,  $\mathbf{D}^T$ -type matrix).
3. Given  $\mathbf{S}$  and  $\mathbf{D}^T$ , calculation of  $\mathbf{C}$  under constraints.

4. Given  $\mathbf{S}$  and  $\mathbf{C}$ , calculation of  $\mathbf{D}^T$  under constraints.
5. Reproduction of  $\mathbf{S}$  from the product of  $\mathbf{C}$  and  $\mathbf{D}^T$ .
6. Go to step 3 until convergence is achieved.

The number of image constituents can be known beforehand or be determined by an exploratory PCA [79] on the whole data set. The alternating optimization should always start using the original measurement,  $\mathbf{S}$ , and an initial guess of either the  $\mathbf{C}$  or the  $\mathbf{D}^T$  matrices. Typically, in images, the initial estimate is a matrix  $\mathbf{D}^T$ , formed by pixel spectra picked up from the image according to previous knowledge (from pixels in areas of interest) or as a result of applying chemometric tools for purest pixel selection, such as SIMPLS-to-use Interactive Self-modeling Mixture Analysis (SIMPLISMA) [99]. The initial estimates of the image constituents (i.e. the pure spectra of an hyperspectral image) may be easy to determine if one has some “a priori” knowledge about the studied process or, when this is not the case, a good alternative is to find selective pixels (where only one constituent appears) that represents better these “pure spectra” than directly selecting spectral channels.

One important characteristic about MCR-ALS is the elimination of the orthogonality constraint for the latent variables, causing the ALS method to provide infinite solutions for the problem (ambiguity in the solution). One way to get the most suitable solution for the problem is by imposing in the algorithm the knowledge about the spectral data. The way to incorporate this “a priori” knowledge in MCR-ALS is by using constraints. These constraints can be defined as chemical or mathematical properties that the concentration profiles or spectra should fulfill [81, 97]. During the iterative process, the calculated concentration profiles and spectra are modified so that they obey the preselected conditions. The application of constraints is optional and should be performed according to the natural characteristics of the data set. Flexibility is also a relevant issue and, therefore, concentration profiles and spectra can obey different constraints and, within the  $\mathbf{C}$  or  $\mathbf{D}^T$  matrices, constraints can be applied profile-wise or even element-wise. Constraints play a double role in resolution methods: on one hand, they ensure the chemical, biological or any other type of meaning of the recovered distribution maps and spectra. On the other hand, they greatly decrease the ambiguity in the resolved profiles.

The concept of ambiguity in the solution is associated to the fact that many  $\mathbf{C} \cdot \mathbf{D}^T$  products can reproduce the original data set with the same optimal fit. In mathematical notation, we can rewrite the bilinear model as:

$$\mathbf{S} = \mathbf{C} \cdot \mathbf{T} \cdot \mathbf{T}^{-1} \cdot \mathbf{D}^T = \mathbf{C}' \cdot \mathbf{D}'^T \quad \text{Equation 3.3}$$

Where  $\mathbf{C}' = \mathbf{C} \cdot \mathbf{T}$  and  $\mathbf{D}'^T = \mathbf{T}^{-1} \cdot \mathbf{D}^T$ , thus obtaining infinite  $\mathbf{T}$  matrices (solutions). The way to cut down the uncertainty in the resolution results is by limiting the possible solutions to those that fulfill the preset constraints. This way, the more efficient the constraints are, the better defined the solution results [100].

There are many studies where these tools can be applied. In the following chapter the application of MCR on DCE-MRI and DW-MRI for the development of new images (imaging biomarkers) able to detect and locate tumors at early stage, in the case of prostate cancer (PCa), is presented. The main objective is to create images with clinical interpretation that will help doctors in diagnosis and prognosis tasks.

### 3.2.3. PLS and PLS-DA

Partial Least Squares (PLS) [83] is a statistical latent variable method that tries to find the relations between two matrices ( $\mathbf{X}$  and  $\mathbf{Y}$ ) by modelling the covariance structure between both spaces, finding the multidimensional space that maximizes the covariance between  $\mathbf{X}$  and  $\mathbf{Y}$ . The PLS approach models the data through the use of the following expressions:

$$\mathbf{T} = \mathbf{X} \cdot \mathbf{W}^* = \mathbf{X} \cdot \mathbf{W} \cdot (\mathbf{P}^T \cdot \mathbf{W})^{-1} \quad \text{Equation 3.4}$$

$$\mathbf{X} = \mathbf{T} \cdot \mathbf{P}^T + \mathbf{E} \quad \text{Equation 3.5}$$

$$\mathbf{Y} = \mathbf{U} \cdot \mathbf{Q}^T + \mathbf{F} \quad \text{Equation 3.6}$$

Where  $\mathbf{T}$  is the score matrix for  $\mathbf{X}$ ,  $\mathbf{U}$  is the score matrix for  $\mathbf{Y}$ ,  $\mathbf{P}$  the loading matrix for  $\mathbf{X}$ ,  $\mathbf{Q}$  the loading matrix for  $\mathbf{Y}$ ,  $\mathbf{W}$  and  $\mathbf{W}^*$  weighting matrices, and  $\mathbf{E}$  and  $\mathbf{F}$  the residual matrices for  $\mathbf{X}$  and  $\mathbf{Y}$ , respectively. Usually, NIPALS (nonlinear iterative partial least squares) algorithm is used for fitting PLS models. A brief explanation of NIPALS can be found in [83].

The PLS model can be expressed in a regression form, as:

$$\mathbf{Y} = \mathbf{X} \cdot \mathbf{B}_{\text{PLS}} \quad \text{Equation 3.7}$$

$$\mathbf{B}_{\text{PLS}} = \mathbf{W} \cdot (\mathbf{P}^T \cdot \mathbf{W})^{-1} \cdot \mathbf{Q}^T \quad \text{Equation 3.8}$$

The PLS-DA [84] is an alternative method when we are dealing with categorical variables in  $\mathbf{Y}$ . In this case, the method is applied as a discriminant between different classes of individuals. Besides, PLS-DA is a versatile algorithm that can be used for predictive and descriptive modeling as well as for discriminative variable selection.

For model optimization, PRESS (predicted residual sum of squares) or its equivalent  $Q^2$  is calculated in order to quantify the goodness of the predictions.

$PRESS_A$  is the squared sum of the prediction errors “r” of the not-considered observations “O” (external set), when “A” components are used to build the model.

$$PRESS_A = \sum_{i=1}^O r_i^2 \quad \text{Equation 3.9}$$

Whereas cumulative  $Q^2$  for “A” components is calculated as follow:

$$Q_{cum}^2(A) = 1 - \frac{PRESS_A}{TSS} \quad \text{Equation 3.10}$$

#### **3.2.4. SMB-PLS**

The Sequential Multi-Block - Partial Least Squares algorithm (SMB-PLS) proposed by Lauzon-Gauthier and Duchesne [95] is an alternative multi-block method to Sequential Orthogonalised - Partial Least Squares (SO-PLS) [101] and Multi-Block - Partial Least Squares (MB-PLS) [102, 103]. A table of the advantages and limitations of both methods is presented in table 2.

SMB-PLS uses the MB-PLS hierarchical structure where the variables are organized in different groups or “blocks” associated to different sources of information known as “regressor blocks” ( $\mathbf{X}_b$ ). But, in this case, SMB-PLS imposes a sequential pathway in order to sequentially extract information from each of them.

Table 2. Advantages and limitations of MB-PLS and SO-PLS.

MB-PLS		SO-PLS	
Limitations	Advantages	Limitations	Advantages
Information mixing (super-score deflation)	Hierarchical structure	Between block correlated information excluded	Different number of latent variables for each block
Misleading interpretation at block level	Single model	As many models as number of blocks	Not sensitive to the scaling of the blocks
Same number of components for each block	Computed from PLS	Need to select block ordering	Clearer interpretation owing to sequential orthogonalization
Sensitive to the relative scaling of blocks		Selection of the number of latent variables can be complicated	

The first step of the algorithm is to compute the block weights ( $\mathbf{w}^T_1$ ) by the regression of an initial  $\mathbf{Y}$  score  $\mathbf{u}$  onto  $\mathbf{X}_1$ , followed by the calculation of the scores ( $\mathbf{t}_1$ ) from the first block. Then, in order to differentiate the correlated information from the orthogonal information, the subsequent blocks ( $\mathbf{X}_b$ ) ( $b>1$ ) are split using the following equation:

For  $b=1,2,\dots,B-1$  and  $k=1,2,\dots,B-b$

$$\mathbf{X}_{b+k}^{corr} = \mathbf{t}_b \cdot (\mathbf{t}_b^T \cdot \mathbf{t}_b)^{-1} \cdot \mathbf{t}_b^T \cdot \mathbf{X}_{b+k} \quad \text{Equation 3.11}$$

These blocks contain the correlated information to  $\mathbf{X}_1$ . After this, the block score for the subsequent block are computed by regressing  $\mathbf{u}$  onto  $\mathbf{X}_b^{corr}$  to obtain the block weights  $\mathbf{w}_b^{T,corr}$ . Next, the block score  $[\mathbf{t}_1 \dots \mathbf{t}_b]$  are combined in the super level score  $\mathbf{T}$ . The last step is the computation of a PLS cycle between  $\mathbf{u}$  and  $\mathbf{T}$  to compute the super level weights ( $\mathbf{w}_T$ ) and the super scores  $\mathbf{t}_T$ . This computation cycle is repeated until convergence on  $\mathbf{t}_T$ . Deflation of all  $\mathbf{X}_b$  using the super scores is then performed. The

procedure is repeated for computing the next component using the residuals of all data blocks. It continues to extract components from the first  $\mathbf{X}$ -deflated block in the sequence until it has modeled all relevant information from  $\mathbf{Y}$ . Any criteria available for selecting the number of components in latent variable methods can be used.

Once all the information from  $\mathbf{X}_1$  has been explained, the same methodology is applied to the subsequent blocks. Since only the correlated information with the previous block was removed by the deflation step, the components for the subsequent block will only model new information not explained by the previous components. For the last block in the sequence, a regular PLS model is fit to the  $\mathbf{X}_B$  and  $\mathbf{Y}$  residuals. The pseudo-code of the SMB-PLS algorithm [95] can be found in Annex 1.

SMB-PLS combines the strength of SO-PLS and MB-PLS methods avoiding their limitations (fig. 13).

The advantages of this method are:

1. Different number of components can be used for each block.
2. It enables the visualization of between blocks correlated information.
3. Different number of components can be computed for each block since only the correlated information is removed after the deflation for the subsequent block. This leaves orthogonal (i.e. new) information in the  $\mathbf{X}_b$  blocks to further explain variations in  $\mathbf{Y}$  by additional components.
4. For each latent variable, block scores and loadings are computed for each block to enable interpretation of relationships between variables, outlier detection and visualization of clustering patterns. The super scores also give important information on the correlation structure between the blocks.

This algorithm has other interesting properties. First, both the block scores and super scores are orthogonal. In MB-PLS, the block scores are correlated. However, in SMB-PLS the information captured by the block scores is the same as the super scores for each latent variable and only the numerical values are not exactly the same. It is only necessary to use either the super scores or block scores for interpretation. Also, for the weights, the block weights are important for the interpretation and relations between variables inside each block. But the super weights are equally important since they provide information about how the information extracted from each block distributes in each component of the model [93-95].

### 3.3. Registration method

In medical image (among other areas), registration methods are those that modify the spatial resolution and correct the position of one sequence with the aim of aligning it to another sequence (reference sequence), i.e. making every pixel from one sequence to exactly correspond to the same pixel of the reference sequence. During the explanation of the method, the selected “reference” sequence will always be referred to perfusion and the “secondary” sequences will be diffusion and T2. This means that the registration method developed in this thesis will align (modify) the diffusion and T2 sequences in order to be spatially coherent with the perfusion one.

The proposed method consists on determining the position where each pixel of the “secondary” sequences from the original sequence (the one taken during the acquisition) needs to be moved, considering their position in the “reference” sequence. For this purpose, this registration method applies a linear transformation taking into consideration some points selected by the specialists. In this method, they manually select two reference points for each spatial direction ( $x$ ,  $y$  and  $z$ ) corresponding to the limits of the organ. These points are needed for both sequences (reference and secondary) and should be taken individually for each patient. The specialists define these coordinates as  $X1$ ,  $X2$ ,  $Y1$ ,  $Y2$ ,  $Z1$  and  $Z2$ . A schematic illustrative view of these points is shown in figure 12.

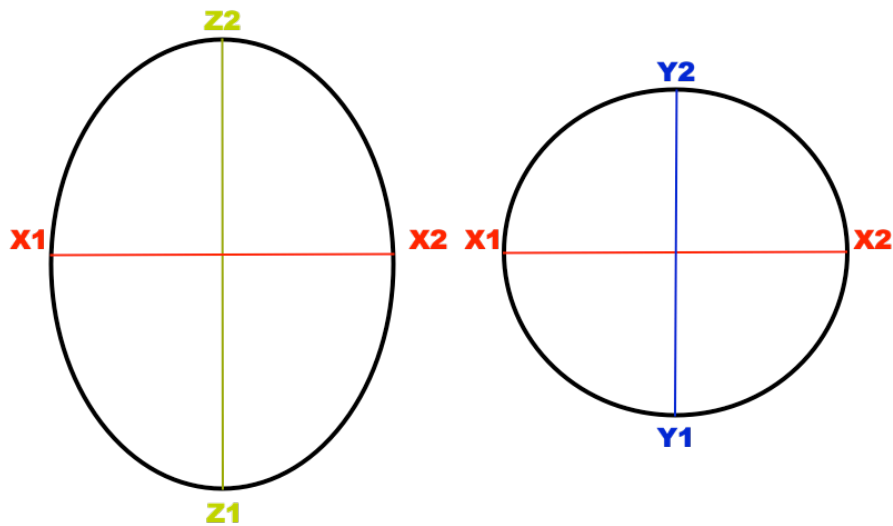


Figure 12. 3D schematic view of the prostate, left: frontal (coronal) plane, right: transverse plane. The points represent the limits of the organ in each spatial direction ( $x$ ,  $y$  and  $z$ ).

The main idea behind the method is based on calculating a function that associates the position of a pixel from one sequence to the other one. For doing this, a linear transformation using the reference points of the prostate is applied. First, it is necessary to calculate the slope of the lineal transformation for each spatial direction. The equation is shown down below:

$$Rel_p = \frac{(ref_{p2}-ref_{p1})}{(sec_{p2}-sec_{p1})}, p: z, y \text{ or } x \quad \text{Equation 3.12}$$

Where “Rel<sub>p</sub>” is the slope of the lineal transformation for each spatial direction *p*, “ref” is the keyword for the reference sequence (perfusion) and “sec” is the keyword for the secondary sequence (diffusion/T2).

Once the slope is calculated for each direction, the following equation determines the location for each position “*i*” (in secondary) or “*j*” (in reference) of each pixel in the corresponding spatial direction:

$$location_p(i) = \left( \frac{(i-sec_{p1})}{Rel_p} \right) + in_{p1}, p: z, y \text{ or } x \quad \text{Equation 3.13}$$

$$location_p(j) = Rel_p \cdot (j - in_{p1}) + out_{p1} \quad \text{Equation 3.14}$$

This way, a function able to determine the location in “ref” from the location in “sec” (eq. 3.13) (or otherwise, eq. 3.14) for each spatial direction (*x*, *y* and *z*) is obtained. This is a direct relation between one pixel in the “ref” sequence with their corresponding location in the “sec” sequence, where only the slope Rel<sub>p</sub> and the coordinates of one reference pixel (*p*<sub>1</sub> in eq. 3.12) are needed.

Taking as a reference the data structure shown in figure (9, A), the method follows two consecutive steps in order to do the transformation of the secondary data structure:

1. First determine if the resolution is the same between the reference and the secondary sequence. If it corresponds perfectly, it is possible to directly apply the linear transformation explained in step 2. Otherwise, the dimensions of the images should be modified.

Normally in MR imaging, the spatial resolution is the same for *x* and *y* and do not change independently. On the one hand, if the resolution of the reference sequence is higher than the secondary sequence, the reference sequence should be rescaled in a higher resolution considering that the information of one pixel will be taken to fill the

empty new pixels of the re-scaled image. This can be considered as an artificial expansion (extrapolation) of the original data structure (fig. 13).

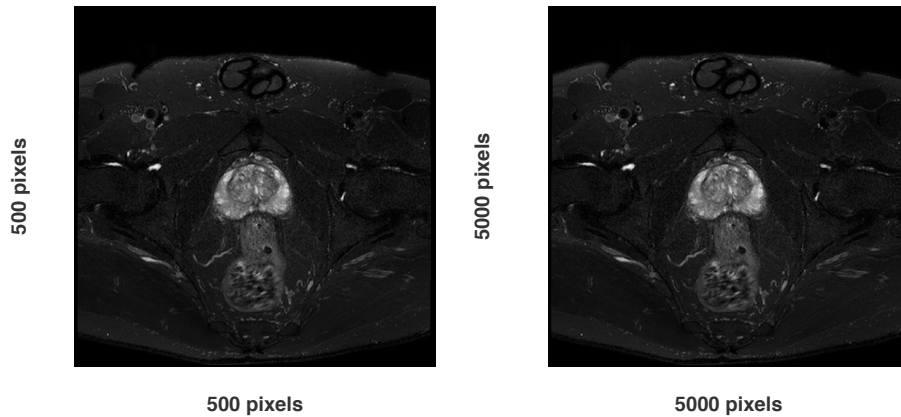


**Figure 13. Example of an expansion performed on a T2w image. The original image is (500x500) pixel resolution (left) and the reconstructed image is (5000x5000) pixel resolution (right). There are no great differences between them because the method is only extrapolating the information available.**

On the other hand, if the resolution of the reference sequence is lower than the secondary sequence, the process is the same but in this case is a compression of the original image. In this case, it is assumed that the information from various pixels is used only for one pixel in the reconstructed image, with the associated loss of information. (fig. 14).

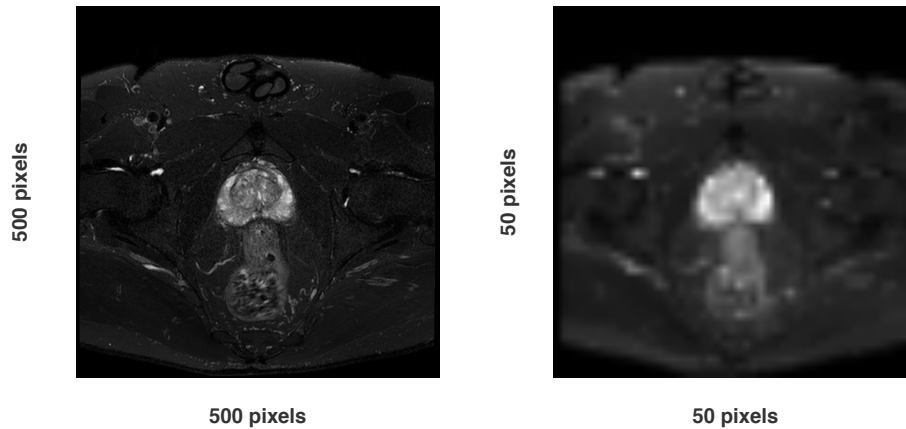


**Figure 14. Example of a compression performed on a T2w image. The original image is (500x500) pixel resolution (left) and the reconstructed image is (50x50) pixel resolution (right). There are huge differences between them because the method is compressing the data from a high-resolution image into a low-resolution image, with the associated loss of information.**

The same idea of expansion/compression can be applied for the  $z$  spatial direction. The size of  $z$  is determined by the number of slices taken during the acquisition, and if the number of slices of the reference sequence is higher or lower than the secondary one, the method will apply an expansion or a compression, respectively.

2. Once the resolutions of both sequences are equal, the linear transformation is also applied for determining the final position of the pixels. However, one problem clearly appears when trying to determine the exact destination in the “ref” sequence. The result, normally, will be an intermediate position inside a 3D parallelepiped structure. In other words, the real contribution to each pixel is composed not only by one pixel but also by their eight neighbour vertices of the corresponding structure (fig. 15).

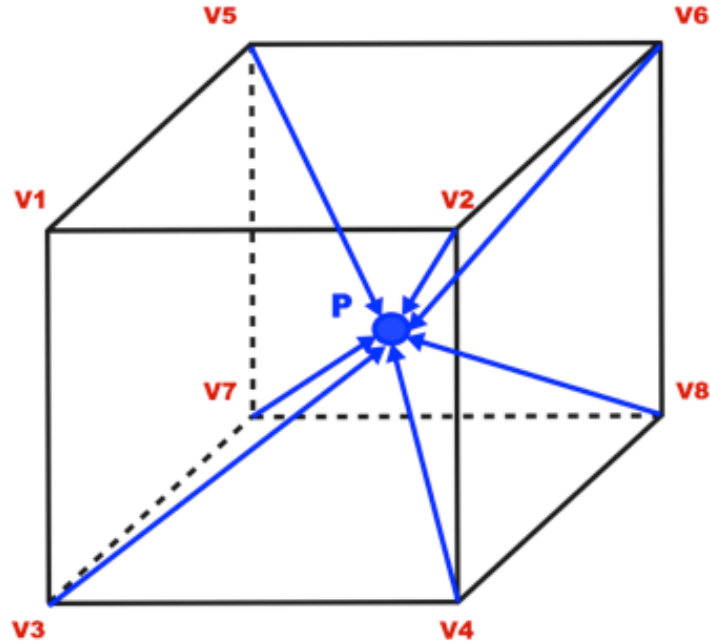


Figure 15. Destination point of one specific pixel and the contribution by distance of its eight neighbours forming a parallelepiped structure.

This way, the signal intensity of “P” will be calculated as an average of the eight neighbour signal intensities weighted by the inverse of its Euclidean distance to “P” as it is shown in equation 3.15.

$$Distance_i = \sqrt{[(P_x - V_{ix})^2 + (P_y - V_{iy})^2 + (P_z - V_{iz})^2]}, i=1..8 \quad \text{Equation 3.15}$$

The contribution of each vertex should be a number between [0-1] and the sum of all the contributions should be 1. For doing this, the total sum of the inversed distances is calculated as follow:

$$D_{GLOB} = \sum_{i=1}^8 \frac{1}{Distance_i} \quad \text{Equation 3.16}$$

And finally, the weighted contribution is calculated in equation 3.17.

$$S_{new} = \sum_{i=1}^8 \frac{Distance_i^{-1}}{D_{GLOB}} \cdot S_i \text{ Equation 3.17}$$

Where  $s_{new}$  is the output intensity value for the secondary sequence after applying registration (diffusion (2), the one reconstructed by the method) and  $s_i$  is the input intensity value taken from the corresponding pixel of the secondary original sequence (diffusion (1), the one taken by the acquisition system).

After applying this method for all the pixels of the data structure, an aligned reconstruction of the secondary sequence is obtained.

This method is applied case-by-case to the diffusion and the normalized T2-weighted sequences (patients with delimited ROI's). One example of the application of the method is shown in figure 16.

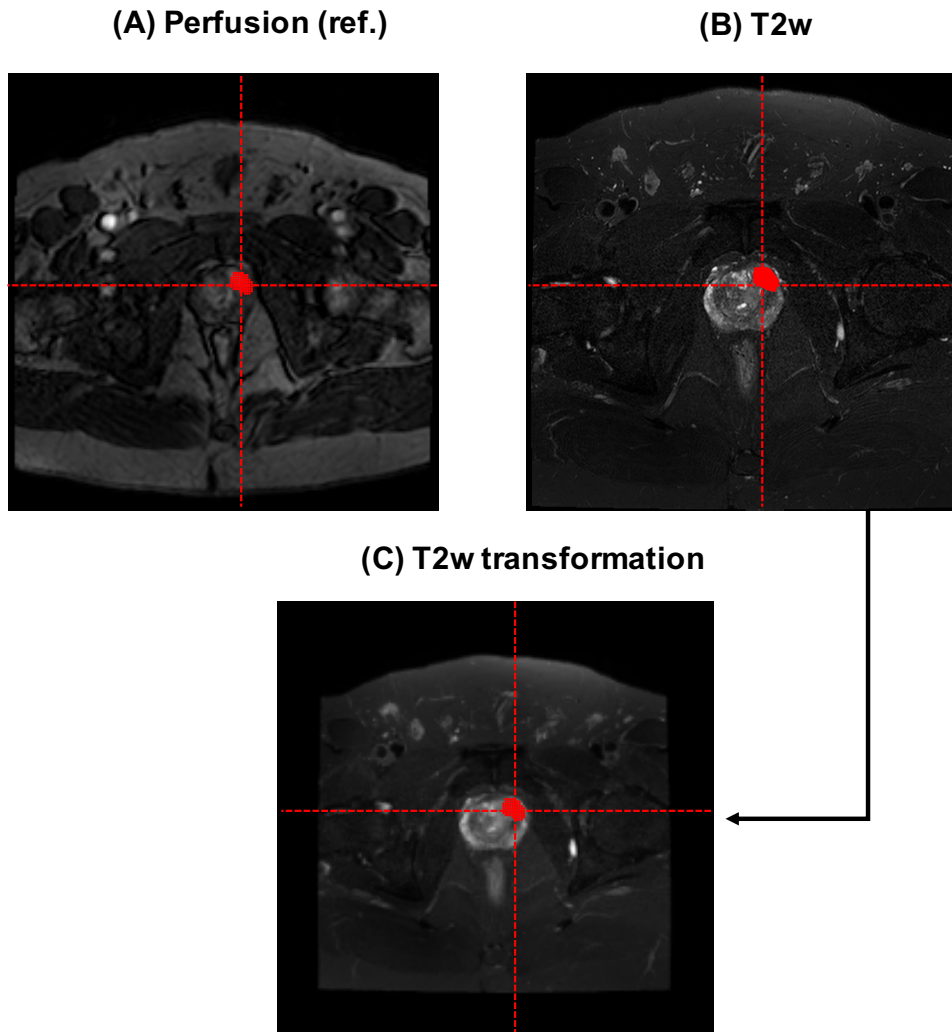


Figure 16. (A) Reference sequence image (perfusion), with the reference ROI highlighted in red. (B) T2w muscle normalized original image. The red lines indicate where the ROIs gravity center is placed in perfusion. (C) T2w after applying the registration method aligning it to perfusion. The Lesion ROI is shown in red. (The method performed a compression and an alignment). The lines check how well the method has aligned both sequences.



# Chapter 4

## Developing new imaging biomarkers with MCR

Traditionally, multivariate curve resolution (MCR) models have been applied in chemistry problems [80, 96, 104-105]. From early 2000s, the applications of these models on images have increased, mainly in chemistry and pharmaceutical environments [106-107] favored by the similitude between the image data structure (after proper unfolding) and the data arrays commonly analyzed, where each row contains the profile along the columns variables (e.g., wavelengths) of each observation (pixels vs samples).

The wide applicability of MCR on chemical images comes from the fact that the spectrum at each pixel location can be modeled as the weighted sum of its pure chemical compounds present in the whole data structure, where this weight is the relative concentration of each chemical compound at that pixel location. This concept can be easily extrapolated to other environments, as is the case of medical MR images, where the registered signal, which depends on the type of sequence (or study), is also a weighted sum of the relative relevance of each “pure” physiological behavior (phenomenon) at that pixel location.

### 4.1. Data structure preparation of MR images

For applying MIA to MR imaging it is necessary to unfold each image ( $x \cdot y \cdot J$ ) (where  $x \cdot y$  is the image size and  $J$  is the number of time points in DCE-MR, and the number of

b-value's in DW-MR), thus forming a 2D structure  $((x \cdot y) \cdot J)$  matrix that can be analyzed by MCR (see chapter 3.1, figures 9 and 10). Then, each slice is stacked one below the other, forming the data structure shown in figure 11 (chapter 3.1). This type of unfolding, keeping the  $J$  variables in columns and stacking each slice one below the other, is applied because the underlying physiological phenomena are assumed to be the same throughout the whole prostate volume.

The following sections will show how these issues have been addressed, and how MCR can help in developing new easy-to-interpret biomarkers, both in perfusion and diffusion. In the case of perfusion, this work will show how these new biomarkers are related to those obtained from the pharmacokinetic models. We will also provide a methodology for reducing the uncertainty in the estimation of the pharmacokinetic models (filtering). Finally, for the diffusion sequence, a method for validating the different clinical exponential models will be shown.

## 4.2. Applying MCR to DCE-MRI

By applying the unfolding procedure shown in figure 11, an  $\mathbf{S}$  matrix ( $x \cdot y \cdot z$  rows,  $t$  columns) is obtained for the DCE-MR images related to each patient. Where  $z$  is the number of slices taken for covering the prostatic region of this patient,  $x \cdot y$  (normally,  $x$  and  $y$  present the same size: 192 pixels) is the number of pixels for each image (do not vary during the MR study of each patient) and  $t$  is the number of time points taken during the DCE-MRI process (after introducing the contrast). After applying the unfolding process, MCR-ALS [81, 96-98] can be applied.

The idea behind MCR, traditionally applied in analytical chemistry, can be easily transferred to the concept of dynamic perfusion phenomena, stating that the pixel enhancement curve  $C(x,y,t)$  is a linear combination of the different "pure" dynamic behaviors existing in it. The lack of orthogonality restriction in the pure dynamic behaviors improves the model in terms of physiological interpretability.

In this thesis,  $\mathbf{D}^T$  is a matrix containing in its rows each one of the dynamic behaviors modeled,  $\mathbf{C}$  gathers in its rows the relative importance of each modeled dynamic behavior for each pixel of the image, and  $\mathbf{E}$  is a residual matrix. As commented in section 3.2, this notation is not the commonly used in MCR, where  $\mathbf{D}$  usually relates to the data matrix and  $\mathbf{S}$  to the "pure spectra".

The iterative ALS process can provide infinite solutions for the same data matrix. This problem can be solved by imposing other type of constraints commonly related to prior knowledge about the problem faced, so it is possible to obtain easier-to-interpret solutions, which also tend to be unique when the constraints introduced under the hypothesized assumptions are sensible [108].

#### 4.2.1. MCR-perfusion sequential step procedure

MCR relies in the correct determination of the number of “real” dynamic behaviors in a data set. In this case, the expected behaviors are shown in figure 17, and defined here as:

- (1) Type A: drastic enhancement and fast washout (AIF) (blood flowing within the arteries), corresponding to the dynamics pattern in the artery closest to the organ of interest (fig. (17, A)).
- (2) Type NT: slow progressive enhancement with slow or without washout, corresponding to a non-cancerous tissue (fig. (17, B)).
- (3) Type VT: delayed drastic enhancement and widened washout in comparison with the perfusion in the arteries (AIF), corresponding to a highly vascular tissue, such as a tumor (fig. (17, C)).

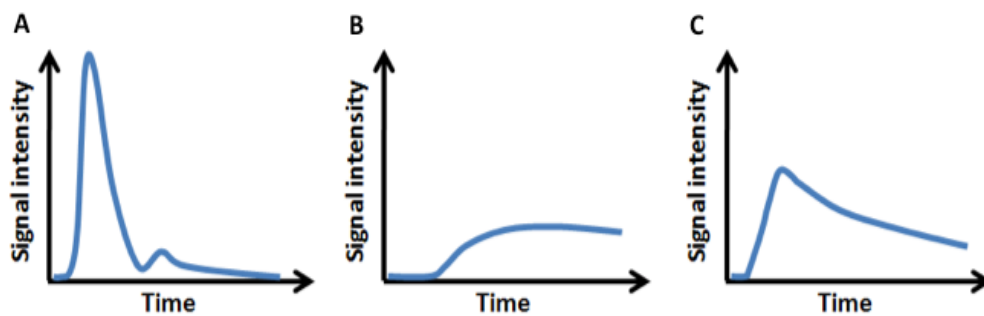


**Figure 17. Dynamic patterns after the injection of a contrast media in dynamic contrast-enhanced magnetic resonance images. (A) Abrupt initial peak and fast washout: AIF. (B) Slow progressive enhancement with slow or without washout. (C) Delayed fast initial enhancement and slow washout. Curves (B) and (C) are often analyzed using the same pharmacokinetic model, which may lead to biased results in the estimated parameters.**

When some “a priori” information is available, it can be used as an initial estimation. This a priori knowledge can be checked by using some tool able to show up the relevant sources of information in the time-sequenced images. One possible way to do this is by applying PCA on the data set, and taking a look at the number of latent variables (PCs) with the highest variances. Once the number of likely dynamic behaviors present in the image is determined, the purest dynamics in the raw data can be sought using e.g., SIMPLISMA [99]. The loadings ( $\mathbf{P}^T$ ) extracted from PCA (not the best option in this case, because not all the purest dynamic behaviors could be a priori known to be located at some pixels nor negative dynamics behaviors could appear), genetic algorithms methods [109-111], or orthogonal projection approach [112] can provide an initial guess of  $\mathbf{D}^T$  in order to start the ALS algorithm.

The previous steps only help on the initial estimation of the dynamic behaviors ( $\mathbf{D}^T$ ). However, these dynamic behaviors do not need to be present in all pixels. In order to find out the likely number of dynamic behaviors present in a pixel, the fixed size image window-evolving factor analysis [113-114] can be applied, as in [88]. Nevertheless, the experience in this problem has led to impose the following constraints: non-negativity on the pixel intensity values, because the intensity in a pixel has to be nonnegative, and non-negativity on the dynamic profiles. Regarding the use of additional constraints, it is preferably not to impose any a specific shape of the dynamics in  $\mathbf{D}^T$  that might bias the results, and leave the model free to fit the best dynamic form in each case. This is different in DW-MRI, where we expect specifically decreasing exponential shape curves. This way, the ambiguity in the solution is reduced by introducing “a priori” knowledge in the form of constraints, which will lead to more accurate and realistic solutions for  $\mathbf{D}^T$ .

The MCR model built this way provides the matrices  $\mathbf{D}^T$  and  $\mathbf{C}$  previously commented, gathering the dynamic behaviors found, as well as the corresponding relative importance of each dynamic behavior at each pixel location, respectively. By unfolding the  $\mathbf{C}$  matrix back into the original  $x \cdot y$  spatial dimension, new images (known as distribution maps) are obtained, which allow to locate those pixels more related to each of the corresponding dynamic behaviors provided by the model.

The whole sequential procedure is summarized in the following steps:

- a) Determination of the approximate number of dynamic behaviors by, e.g., PCA or SIMPLISMA, according to the number of relevant singular values and the available “a priori” knowledge about the process.
- b) Determination of the pixels with purest dynamic behaviors.
- c) Application of MCR-ALS with the additional constraints of non-negativity both on the pixel intensities and the dynamic behaviors.

Applying these first three steps on the whole prostatic region is necessary in order to obtain a unique model per patient. This way, the pure dynamic behaviors ( $\mathbf{D}^T$ ) are valid along all the prostatic volume and the different slices can be directly compared.

- d) For improving the precision in the prostate area, local MCR models were built for each of the analyzed prostates. Masks of the prostate provided by the specialists were used here for segmentation purposes. The dynamic behaviors obtained in the previous MCR model, with the exception of the AIF (which is present in the arteries, but not in the prostate) can be implemented as an initial guess. The same constraints were imposed.

In order to obtain an accurate initial estimation of the dynamic behaviors and for simplicity reasons, these steps can be first applied on a representative slice including the prostate, afterwards extending the results to the whole prostate volume (taking all the slices together).

**4.2.2. A detailed example of MCR-perfusion application**

To illustrate the application of the MCR-based methodology on the DCE-MR images, one case is discussed in detail on a patient with a carcinoma in the transitional gland of the prostate.

As commented before, the first step in any MCR analysis on DCE-MR images deals with obtaining the number of significant dynamic behaviors in the image. Figure 18 presents the variances of the 2<sup>nd</sup> to 10<sup>th</sup> PCs from the fitted PCA model (1<sup>st</sup> component is not shown since it distorts the scale and the differences between 2<sup>nd</sup> component and the subsequent ones cannot be distinguished). It can be seen that from PC 5 in advance, all the PCs have similar amount of explained variance, and even PC 4 is doubtful. This means that not only the three a priori assumed physiological dynamic behaviors may be present in the MR images but also some more unknown behaviors. Therefore both possibilities, using three (results not shown) and four behaviors, should be checked.

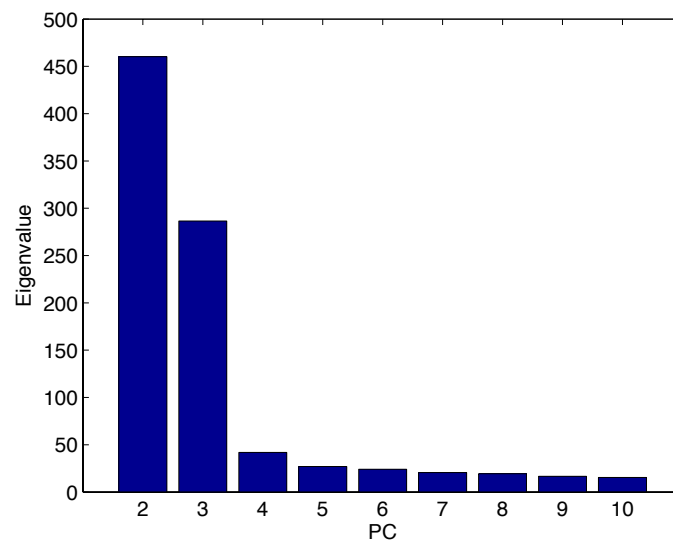


**Figure 18. Variance related to each PC, from the second PC to the 10th. 1<sup>st</sup> component is not shown since it distorts the scale of the bar plot (it is always considered statistically significance).**

Assuming four potential dynamic behaviors, the purest ones to be introduced in the model are found. Figure 19 shows the results corresponding to the case under study for the four dynamic behaviors indicated by PCA in figure 18. As can be seen, not only the types AIF, NT, and VT can be guessed but also an additional effect associated to the contrast media arrival (type CMA) (fig. (19, B)).

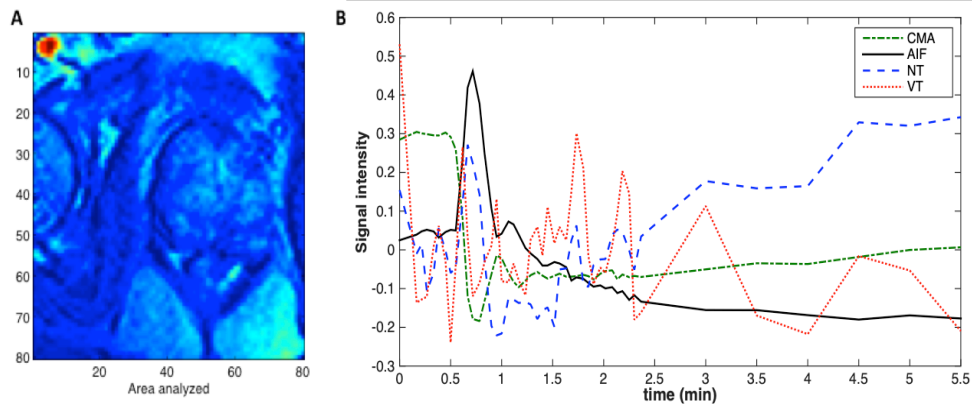


**Figure 19. (A) Image area selected for finding the initial estimates of the physiological dynamic behaviors. (B) The corresponding initial guesses: Non-physiological Contrast Media Arrival (type CMA, dotted-dashed green) effect, type AIF (solid black), type NT (dotted blue), and type VT (dashed red) initial guess dynamic behaviors.**

The next step consists in applying the non-negativity constraints on the pixels intensities and on the dynamic behaviors in the MCR model, matrices  $\mathbf{C}$  and  $\mathbf{D}^T$ , respectively. Figure 20 shows the obtained dynamic behaviors, very similar to those provided by the purity-based methods. The main difference would be in the estimation of the AIF, which is quite important for the pharmacokinetic modeling, as already stated. It is also possible to see that VT behavior is delayed with respect the AIF (about 3–4 seconds) and presents much larger amplitude.

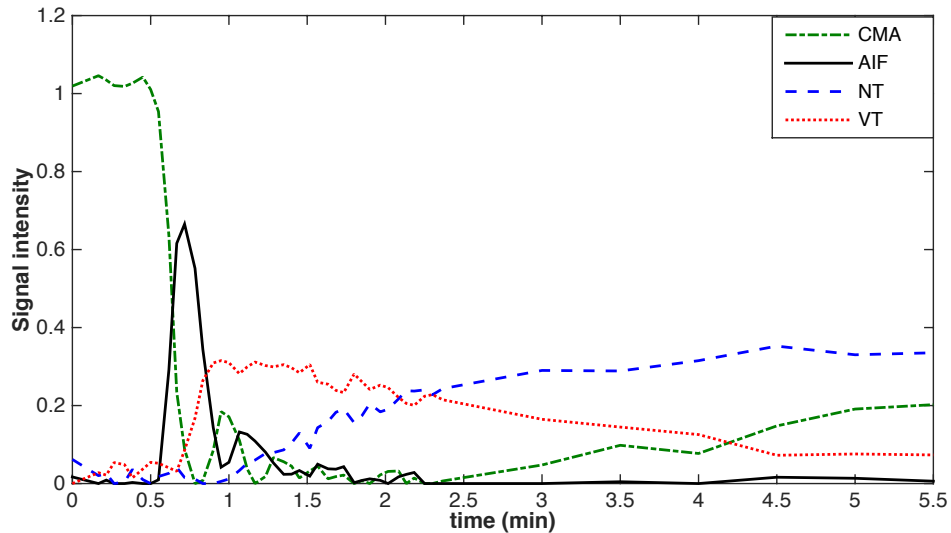


**Figure 20.** Dynamic behaviors provided by the MCR model: type AIF (black solid line), type NT (blue dotted line), type VT (red dashed line), and non-physiological CMA effect (green dashed-dotted line).

In order to visualize where these dynamic behaviors are more predominant, it is necessary to refold back each of the columns of the  $C$  matrix into their original spatial dimension,  $x-y$ , obtaining the dynamic behaviors distribution maps (fig. 21). By looking at both figures, we can appreciate that VT behavior (fig. (21, D)) is slightly appearing in some internal area of the prostate, and it is an indicator of a highly vascularized region. In addition, (fig. (21, B)) provides the pixels that show the arterial perfusion process sought, corresponding to the iliac arteries. Furthermore, there is a progressive enhancement in the rest of the prostate, as well as in the rest of the tissue, which is in accordance to the healthy-like contrast uptake process (type NT) (fig. (21, C)). Finally, it can be assessed that there is a clear additional non-physiological type called CMA effect (fig. (21, A)) of no physiological interest, but also captured by the model. This non-desired effect is probably inherent to MR studies, which use an exogenous contrast media. The arrival of the contrast media in the tissue of interest changes its magnetic properties and thus, the signal intensity. In other words, the images are slightly affected too, though the MR equipment usually equalizes them to minimize the effects. Also, this fourth dynamic is predominant at certain low-vascular peripheral regions (see fig. (21, A)), which correspond to some specific elements of the MR receiving coil. Nevertheless, it would be convenient to subtract this CMA from the data structure before the analysis, in order to better determine the AIF, as well as to improve the pharmacokinetic-based imaging biomarkers calculation (*see chapter 2.3.4*). From figure 21, it is possible to appreciate that the CMA effect seems to affect,

to some extent, the VT and NT types in the peripheral areas.

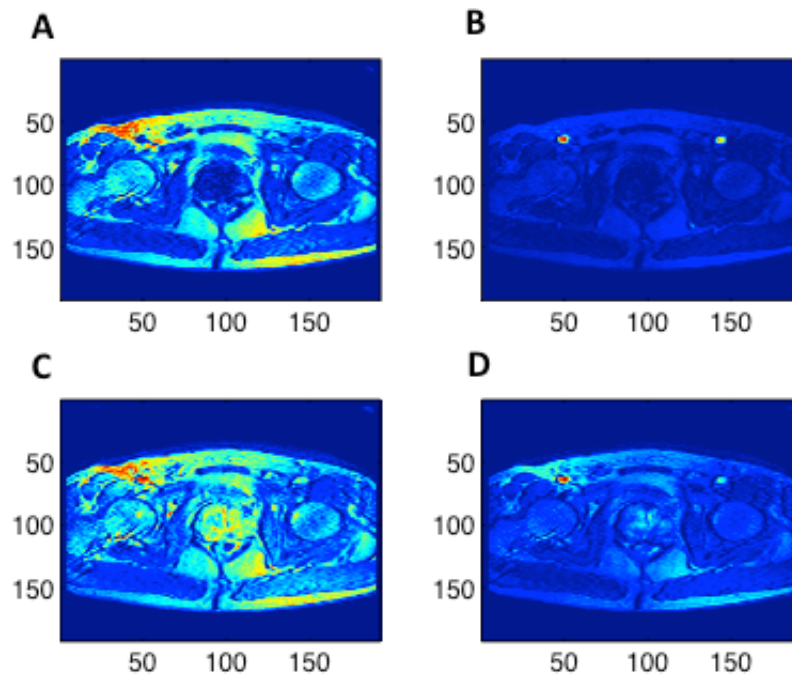


**Figure 21. Distribution maps of the dynamic behaviors shown in figure 20. Non-physiological Contrast Media Arrival (Type CMA) effect. (B) Type A (notice the high contribution at the iliac arteries). (C) Type NT. (D) Type VT.**

Up to this step, it must be stated that PCA is also able to extract out the AIF function in a very short time [65], but not the segregation between the behaviors in the prostate, nor the existence of the CMA type behavior. Furthermore, the fact of imposing orthogonality often forces the AIF dynamic to disaggregate on more than one PC (although this is not a limitation for the procedure related to the segmentation of the iliac arteries [65]).

The dynamic behaviors previously detected may still be estimated more precisely when focusing into the prostate area local model. In order to deal with this issue, MCR local models for the prostate area are fitted. This approach dismisses the AIF pure arterial behavior (related to the iliac arteries in this case), since it is not present in the prostate region. (Fig. (22, A)) shows the final optimized dynamic behaviors and distribution maps for the prostate area MCR local model. Furthermore, MCR feasible bands [108] can be also applied in order to check for possible ambiguities and study the feasibility

of the final dynamic behaviors obtained. As shown in figure (22, B), the bands are overlapping with the proposed solution. In other cases [88, 90], the bands are very close to the found dynamics, which gives confidence (joint to the clinical validation) in the methodology proposed.

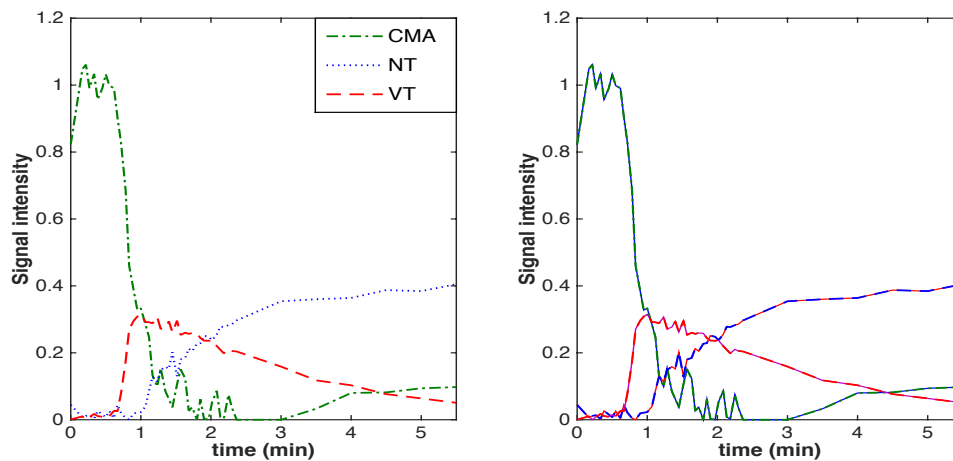


**Figure 22. (A) Dynamic behaviors provided by the prostate area MCR local model: type NT (blue dotted line), type VT (red dashed line), and type CMA (green dotted-dashed line). Note that type A has not been included as there are no arteries in the prostate area. (B) Feasible bands.**

As can be seen by comparing figures 20 and 22, all dynamic behaviors remain essentially the same. Only the non-physiological CMA effect has slightly changed, losing a peak at minute 1. On the other hand, figure 23 shows the benefits of focusing on the prostate region: now, the VT dynamic distribution map (fig. (23, C)) clearly shows up the pixels with higher intensities, i.e., more related to this type of behavior.

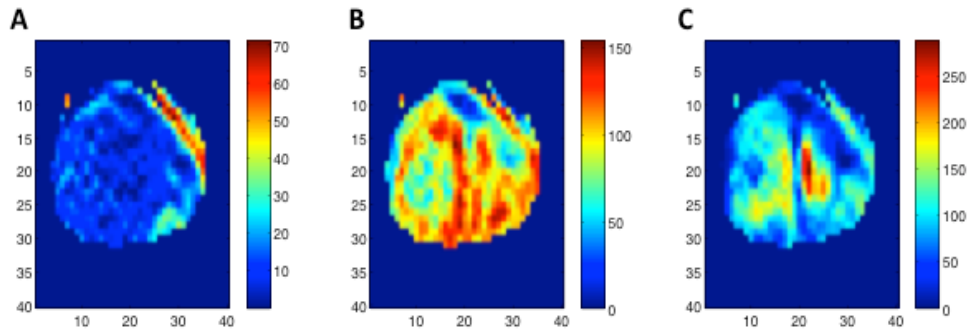


**Figure 23. Distribution maps of the dynamic behaviors from prostate MCR local model shown in figure 22. (A): type CMA. (B): type NT. (C): type VT. Note that type AIF has not been included as there are no arteries in the prostate area.**

After applying the appropriate sequential method to one slice of reference, the next step is to extend the MCR modeling methodology to the whole data structure, as indicated in figure 11, by stacking all the slices one below the other and using these found dynamic behaviors as initial guess on the masked selected pixels (corresponding to the prostatic area). Afterwards, applying MCR with the commented non-negativity constraints on both intensities and dynamics behaviors, figure 24 shows the final global optimal solution (A) as well as the corresponding feasible bands (B). There is only a very small variability at the end of the VT dynamics behavior. Moreover, these dynamic behaviors are very similar to those used as initial guess, shown in figure (22, A), indicating that these behaviors do not change significantly throughout the prostate volume.

The different distribution maps are shown for all 12 slices: figure 25, corresponding to the CMA artificial dynamic behavior; figure 26, corresponding to the NT dynamic behavior; and figure 27, corresponding to the VT dynamic behavior. The model gathers 94.6% of the variability in the data. This is extendable to all cases analyzed. Figure 28 provides the residuals sum of squares (RSS) images that show the pixels with some abnormal deviations with respect to the modeled dynamic behaviors.

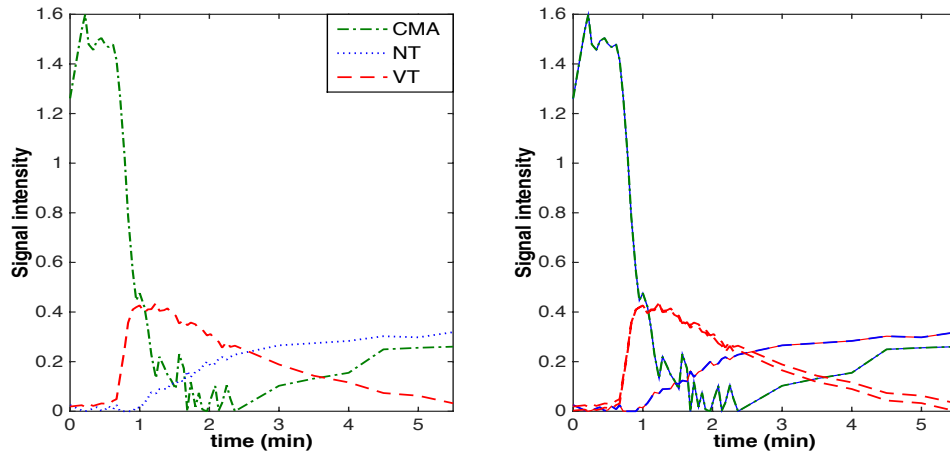


Figure 24. (A) Dynamic behaviors provided by the MCR global model of the prostate: type NT (blue dotted line), type VT (red dashed line), and type CMA (green dotted-dashed line). Note that type A has not been included as there are no large arteries in the prostate area. (B) Feasible bands.

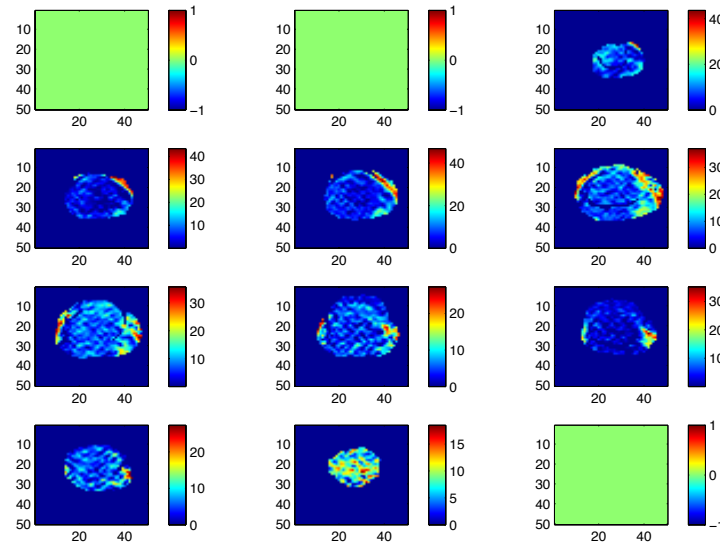
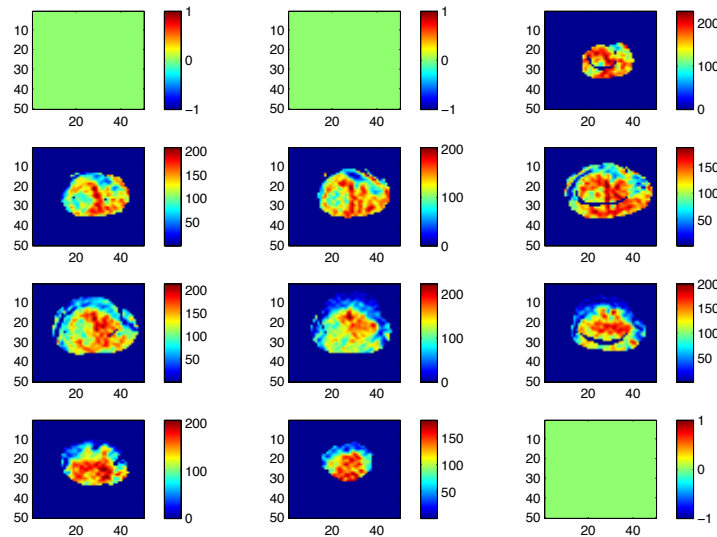
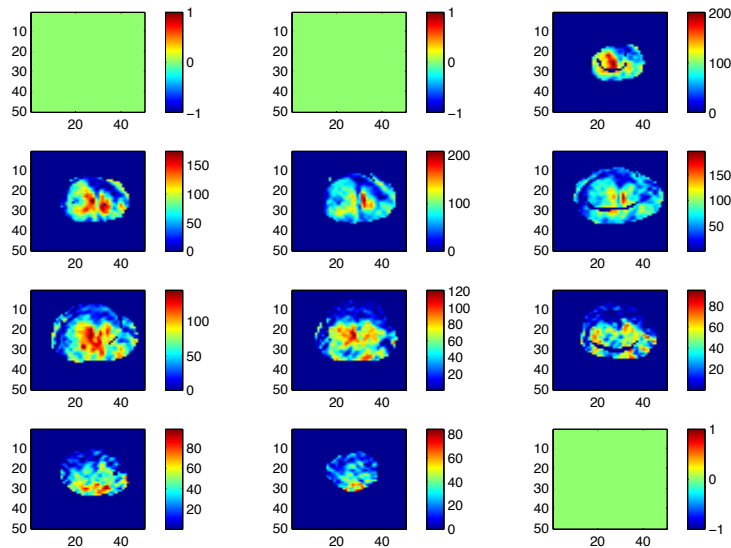


Figure 25. CMA distribution maps for the 12 slices analyzed, from left to right and from top to bottom. Note that slices 1, 2, and 12 do not have prostate area masked. Masks are the union of the peripheral and inner prostate zones (some slices present prostate pixels unselected due to manual masking selection).



**Figure 26. NT distribution maps for the 12 slices analyzed, from left to right and from top to bottom. Note that slices 1, 2 and 12 do not have prostate area masked. Masks are the union of the peripheral and inner prostate zones (some slices present prostate pixels unselected due to manual masking selection).**



**Figure 27. VT distribution maps for the 12 slices analyzed, from left to right and from top to bottom. Note that slices 1, 2 and 12 do not have prostate area masked. Masks are the union of the peripheral and inner prostate zones (some slices present prostate pixels unselected due to manual masking selection).**

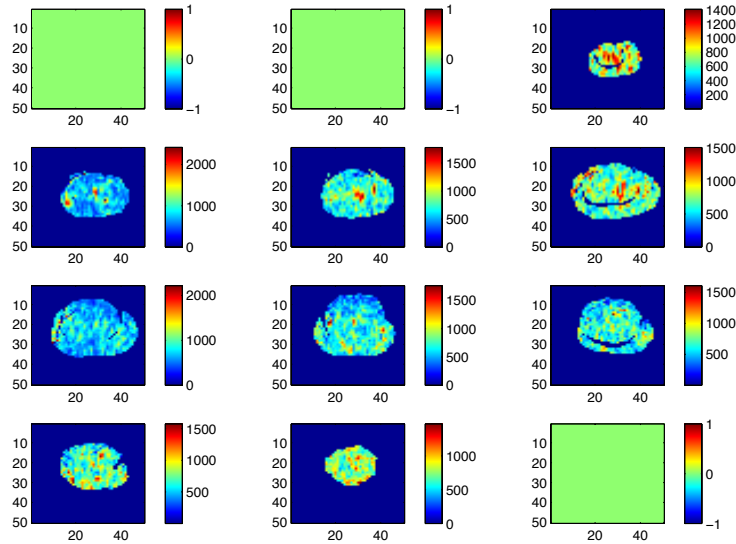


**Figure 28.** RSS distribution maps for the 12 slices analyzed, from left to right and from top to bottom. Note that slices 1, 2 and 12 do not have prostate area masked. Masks are the union of the peripheral and inner prostate zones (some slices present prostate pixels unselected due to manual masking selection).

Using this analysis scheme it is possible to obtain new and easy-to-interpret MCR-based imaging biomarkers, which provide a direct clinical interpretation of the underlying events of interest. Moreover, it is possible to detect (whenever existing) non-desired artificial effects, hence being able to extract them out from the pure physiological dynamic behaviors and improving the estimation, not only of the VT and NT dynamics but also of the AIF. Finally, it must be stated that using some kind of population dynamics behavior as initial guess, obtained from other methods such as PCA, provides essentially the same results.

### 4.3. Applying MCR to DW-MRI

The DW-MRI acquisition sequence is performed parallel to the transverse plane obtaining images associated to the different slices of the prostate and covering the whole volume of the organ. For each slice, images are taken with different b-values (6 b-values in our dataset), obtaining a 3D structure with (12-15) slices, (x-y) rows and 6 columns as in figure 10. All the slices from the same patient were studied with the same model by stacking the unfolded 2D matrices of each slice one below the other obtaining an S data matrix. This way the fitted behaviors were forced to keep the same

internal correlation structure along the whole prostate volume for a particular patient, as for the DW-MRI sequences.

After refolding the images, a signal decay  $\mathbf{s}$  is extracted from each pixel of the prostate, associated to the different b-values. In all cases, local models are built by removing the pixels that do not pertain to the prostate zone with manual masks provided by the specialists. In this case, local models were directly used because there was no need to study the outside of the prostate, as the arterial behavior is not relevant. This way, the interpretation of the results is improved and the computational time reduced.

In order to develop the new biomarkers in DW-MRI, it is first required to choose which  $n$ -exponential model should be selected. As for DCE-MRI, using MCR as the multivariate statistical projection model in MIA can help in deciding the number of exponential decays (i.e., behaviors) to use, providing new nonparametric models that can explain the principal diffusion behaviors extracted, helping specialists to detect and characterize early tumors in the prostate, and providing new imaging biomarkers that may complement those commonly used for clinical diagnosis.

#### **4.3.1. MCR-diffusion proposed model**

As commented before, in the diffusion process, the studied phenomena are those related to slow diffusion, associated to cellularization, and fast diffusion, associated to vascularization. Assuming that the signal spectrum in a pixel  $j$  can be expressed as a weighted sum of different decreasing exponential functions modeling the different phenomena of the diffusion process, we propose the following model:

$$\mathbf{s}_j = \sum_{i=1}^I c_{ij} \cdot (\alpha_i \cdot e^{-\beta_i \cdot b}), \quad \alpha_i, \beta_i, c_{ij} \geq 0 \quad \text{Equation 4.1}$$

Where  $I$  stands for the number of exponential functions used. In this thesis, models using 1, 2, and 3 exponential functions are studied. The triexponential approach is proposed in order to model a possible additional behavior with physiological meaning that might remain in the residuals of the biexponential approach.

The main differences regarding the theoretical models outlined previously are the non-normalization of the spectra (using  $\mathbf{s}$  instead of  $\mathbf{s}/s_0$ ) and the independence between the  $\alpha_i$  coefficients, which are not forced to sum up 1 (contrarily to what happens in the IVIM model with the  $f$  and  $(1-f)$  parameters).

As for DCE-MRI, the MCR-ALS has been used (*see equation 3.2*). In diffusion studies, matrix  $\mathbf{S}$  contains the signal spectrum  $\mathbf{s}$  for each pixel in rows,  $\mathbf{D}^T$  is a matrix containing in its rows each of the diffusion behaviors modeled,  $\mathbf{C}$  gathers in its rows

the relative contribution of each modeled behavior for each pixel of the image, and  $\mathbf{E}$  is a residual matrix.

Regarding the constraints to be used, in the case of the diffusion process, the following ones can be applied successively in order to validate the theoretical models most commonly applied in clinical practice.

- a) Non-negativity constraints are applied both in  $\mathbf{D}$  and  $\mathbf{C}$  matrices, because the modeled behaviors and their relative contribution in a pixel have to be non-negative.
- b) Unimodality constraints where only one maximum or minimum is admitted are imposed only in  $\mathbf{D}$ , due to the fact that the modeled behaviors are monotonically decreasing.
- c) Shape constraints are applied on the  $\mathbf{D}$  matrices inside ALS, in order to obtain a specific mathematical expression (i.e., exponential decay) for the modeled behaviors.

Including these constraints, the model can select the solutions with more physiological meaning, discarding the rest lacking any clinical interpretation.

#### ***4.3.2. MCR-diffusion sequential procedure***

The sequential procedure to obtain the different MCR models follows:

1. Fit MCR models with only non-negativity constraints in  $\mathbf{C}$  and  $\mathbf{D}$  with one, two, and three components. Select the model with the most appropriate number of components according to the similarity of the corresponding fitted behaviors with the exponential decay (i.e., expected physiological behavior) (Model 0).
2. Fit a new MCR model including non-negativity constraints in  $\mathbf{C}$  and  $\mathbf{D}$ , and unimodality constraints (only one maximum or minimum is allowed for each behavior) in  $\mathbf{D}$  using the number of components decided in step 1 (Model 1).
3. Check the adequacy of Model 1 by fitting the behaviors obtained (rows of DT matrix in step 2) with an exponential function and projecting the predicted exponential behavior onto the original data matrix  $\mathbf{S}$  to obtain the new  $\mathbf{C}$  matrix (Model 2).
4. Finally, fit a new MCR model including non-negativity constraints in  $\mathbf{C}$  and  $\mathbf{D}$  and shape (i.e., exponential decay) constraints in  $\mathbf{D}$  using the number of components decided in step 1 (Model 3).

The MCR models built this way provide the matrices  $\mathbf{D}^T$  and  $\mathbf{C}$ , gathering at each pixel location the behaviors (types of exponential decays) and their relative contribution, respectively. By relocating the pixels in each column of  $\mathbf{C}$  matrix into their original spatial dimension ( $x \cdot y$  pixels), the distribution maps are obtained, locating those pixels more related to each of the corresponding behaviors provided by the model.

It must be stressed that these distribution maps from  $\mathbf{C}$  matrix, not the prostate diffusion behaviors modeled in  $\mathbf{D}^T$  matrix, are the ones performing as imaging biomarkers. This is a conceptual difference with the clinical theoretical models method, where the biomarkers (e.g.,  $D$ ,  $D^*$ , and  $f$  in the case of the IVIM model) are extracted from the behavior modeled at each pixel location.

This tool can help the doctors to locate areas of the prostate that may be potentially affected by a cancerous process. Furthermore, the distribution maps of the RSS were used as a validation method, as they show the pixels that are not well fitted by the model. In the following, we illustrate the application of the MCR-based methodology on the DW-MR images, on a patient with a tumor on the peripheral gland.

### **Model 0**

Initially, the only constraint considered is non-negativity in  $\mathbf{C}$  and  $\mathbf{D}$  matrices. Figures 29 and 30 show the results with one and two components, respectively. In the one-component model, the fitted behavior follows an exponential decay pattern. As can be seen in the distribution map shown in figure (29, A), the pixels related to this behavior are distributed in the whole image, being the RSS low (fig. (29, B)). However, with two components (fig. 30), the residuals are even lower (fig. (30, C)), i.e., the model explains 99% of the variability, and the behaviors are more physiologically meaningful because of the shape of the obtained curves (fig. (30, D)): a quick fall related to fast diffusion ( $d_2$ ) and a slow fall associated to slow diffusion ( $d_1$ ). Nevertheless, there are still two “artifacts” (slight increases of signal intensity) present in both behaviors, at lower  $b$ -values in the pure diffusion (slow diffusion,  $d_1$ ) component and at higher  $b$ -values in the perfusion component (fast diffusion,  $d_2$ ). Regarding the distribution maps, they show that the component related to diffusion (fig. (30, A)) is more representative in the whole zone of the prostate than that of the perfusion component (fig. (30, B)), which is more localized.

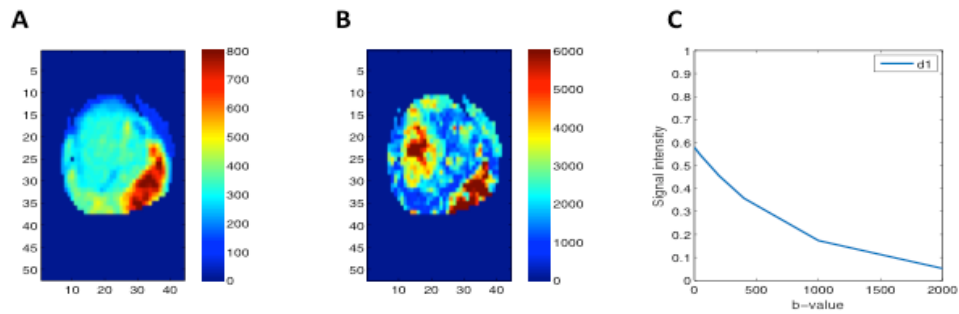


**Figure 29.** MCR Model 0 with one component (95% of explained variability). (A) Score distribution map related to the modeled behavior  $d_1$ . (B) RSS distribution map. (C) Modeled behavior  $d_1$  (solid blue line).

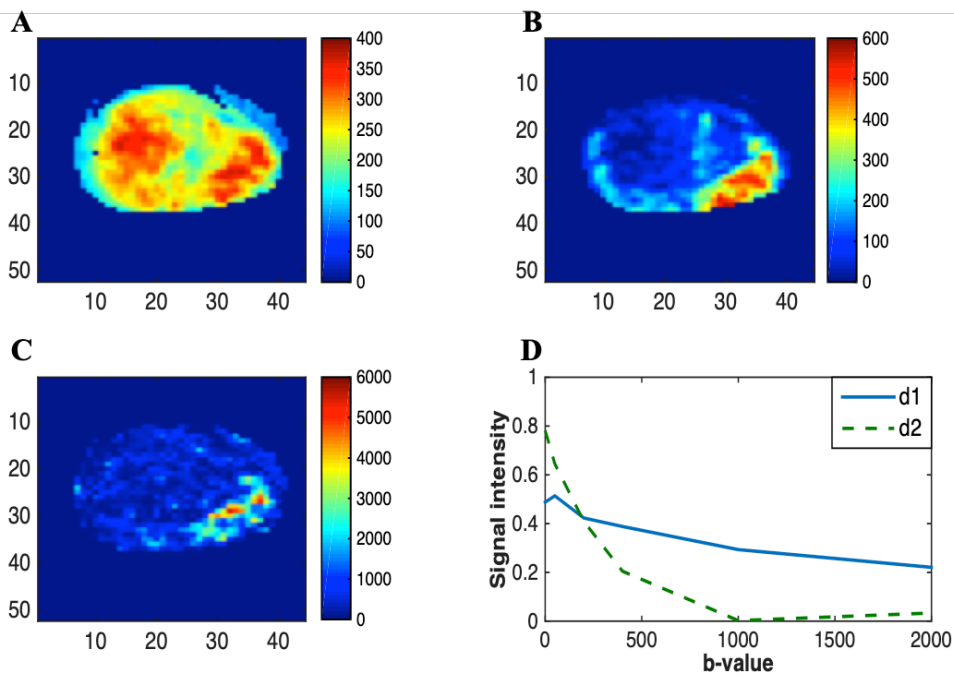


**Figure 30.** MCR Model 0 with two components (99% of explained variability). (A) Score distribution map related to first modeled behavior  $d_1$  (slow diffusion, solid blue line). (B) Score distribution map related to second modeled behavior  $d_2$  (fast diffusion, dashed green line). (C) RSS distribution map. (D) Modeled behaviors.

By comparing both models (with one and two components), it can be seen that the behavior fitted in the one-component model (fig. (29, C)) is a combination of the behaviors modeled in the two-component model (fig. (30, D)). This can also be observed in the score distribution maps (figures (29, A) and (30, A-B)). Therefore, the one-component MCR model is not able to explain all the physiological behaviors present in the diffusion studies due to its simplicity.

Figure 31 shows the modeled behaviors from the MCR model with three components. The behaviors associated to components 2 and 3 make no sense in diffusion studies because the signal spectra cannot increase as the b-value goes up (it is assumed that signal always attenuates when the b-value increases). Therefore, the two-components model is selected as the most appropriate to study the diffusion process.

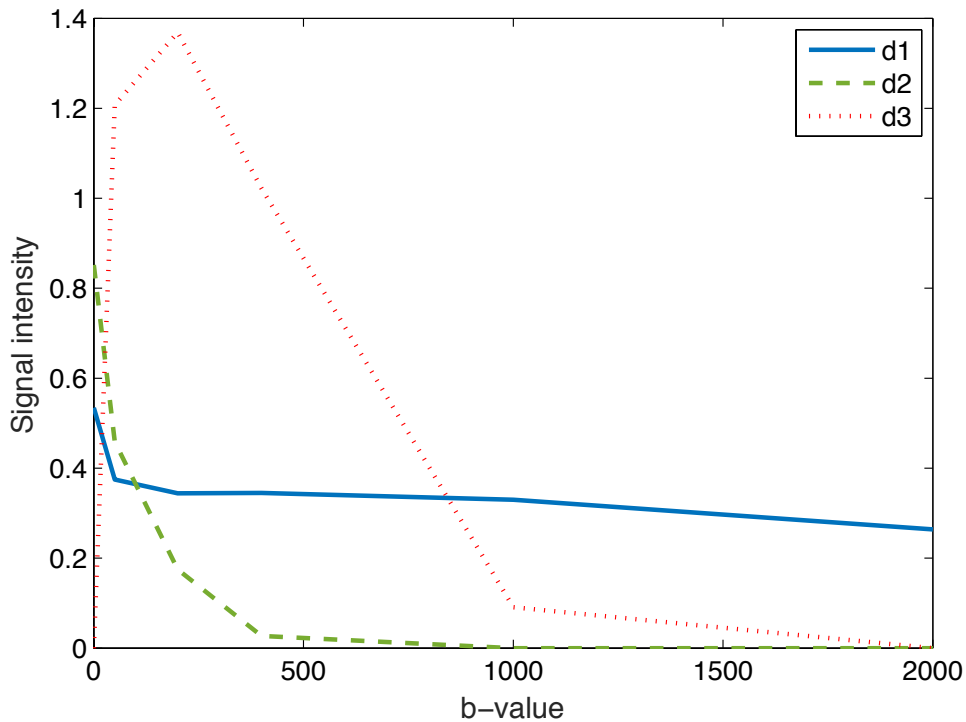


**Figure 31. Modeled behaviors from the MCR Model 0 with three components. The 3rd additional component ( $d_3$ ) represented by the red dotted line has no clinical meaning.**

### Model 1

The next steps consist on sequentially adding new constraints in order to refine the bi-exponential model. The first of these is unimodality (in  $\mathbf{D}$  matrix) in order to provide behaviors more similar to the exponential decay shape. The inclusion of this type of constraint allows removing the artifact present in the perfusion component at high b-values (a slight increase of  $d_2$  from 1500 to 2000 in the b-value) that appears in Model 0 (fig. (30, D)). Nevertheless, there is still one artifact (a slightly increase in the signal intensity from  $b=0$  s/mm<sup>2</sup> to  $b=50$  s/mm<sup>2</sup>) for the first behavior (slow diffusion component), which still accomplishes the unimodality constraint (one maximum at  $b=50$  s/mm<sup>2</sup>). Clinical validation indicates that this artifact cannot happen from a physiological point of view. Furthermore, adding a new component did not isolate this behavior (results not shown).

### Model 2

With the aim of removing the second artifact and checking the adequacy of the biexponential model in diffusion MR studies, a fitting of the behaviors is proposed using: (1) the results provided by Model 1 (the pure behaviors saved in the  $\mathbf{D}$  matrix) and (2) the information of the clinical theoretical models that proposes two decreasing exponential behaviors. Therefore, using fitting algorithms, both behaviors are tuned to exponential expressions  $\alpha \exp(-\beta b)$ . Furthermore, the goodness of fit is high (95%) obtaining two different pure exponential decays related to diffusion ( $d_1$ ) and perfusion ( $d_2$ ), respectively.

The exponential decay shape is obtained in the following way: for each one of the behaviors obtained from the previous model, initial parameters  $\alpha_i$  and  $\beta_i$  ( $i=1,2$ ) are fitted using the exponential decays shown in equation 4.1. Afterwards, using these exponential functions and the b-values, the “pure” behaviors are calculated, and arranged in the  $\mathbf{D}$  matrix. Once the exponential shape of the behaviors is obtained, the next step was to project the original data matrix on the pseudoinverse of the new fitted  $\mathbf{D}$  to get matrix  $\mathbf{C}$ , and from it the corresponding distribution maps.

Note that all these calculations are not performed within the ALS algorithm. It is just a fit of the  $\mathbf{D}_1$  matrix obtained from previous Model 1 on two exponential decays, thus obtaining the new  $\mathbf{D}_2$ , afterwards computing  $\mathbf{C}_2$ . This also means that this new  $\mathbf{C}_2$  matrix might provide negative values, since non-negativity constraints are not applied in the last projection step.

### Model 3

Finally, once the biexponential model is validated, the shape constraints for the  $\mathbf{D}$  matrix were included in the iterative process of the MCR-ALS algorithm, assuming

classical exponential expressions  $\alpha_i \exp(\beta_i b)$  for both behaviors, and non-negativity for **S** and **D** matrices. Details can be found in [89]. For every case, the exponential parameters,  $\alpha_i$  and  $\beta_i$  ( $i=1,2$ ), obtained from Model 2 have been used as an initial approximation.

As can be seen in figure (32, D), the fitted behaviors are two different strictly decreasing exponentials, one related to slow diffusion (slow attenuation,  $d_1$ ) and other related to fast diffusion (fast attenuation,  $d_2$ ). Furthermore, the goodness of fit is at least 99% in all the cases under study, which derives in low-RSS distribution maps (fig. (32, C)).

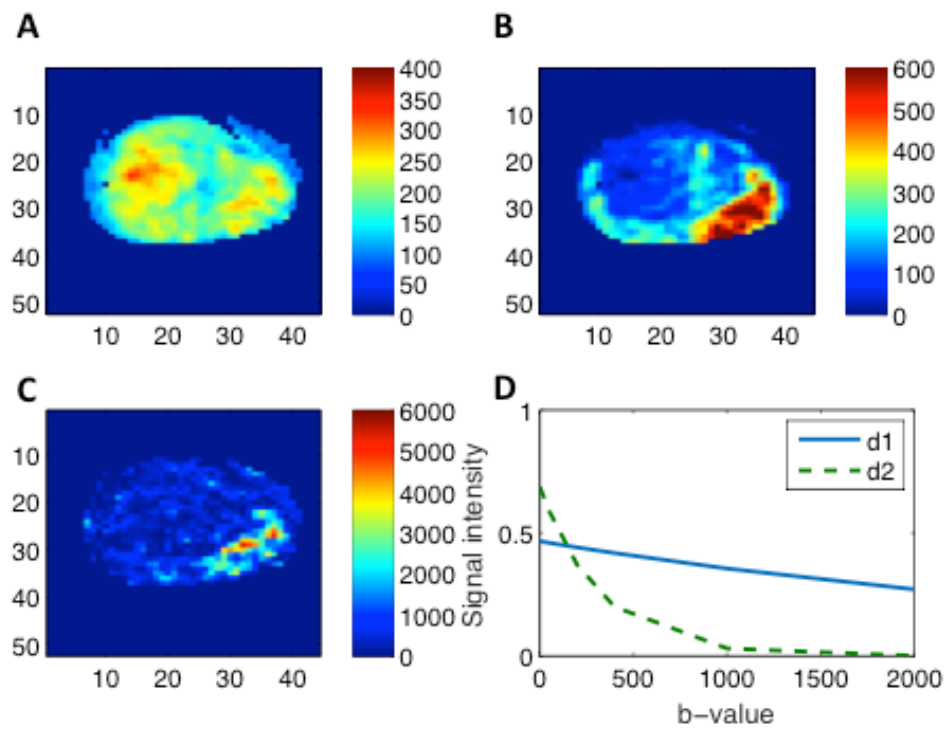


**Figure 32. MCR Model 3 (99% of explained variability). (A) Score distribution map related to  $d_1$  (slow diffusion, solid blue line). (B) Score distribution map related to  $d_2$  (fast diffusion, dashed green line). (C) RSS distribution map. (D) Modeled behaviors.**

#### **4.3.3. MCR-diffusion models discussion**

From all these results, it can be assumed that the monoexponential model seems too simple when trying to obtain all the behaviors present in the images. The triexponential

approach is not useful either, as it provides behaviors that are not physiologically interpretable. On the other hand, the biexponential model has shown up as an optimal approach for modeling the diffusion process. This model has been sequentially improved by comparing the new results provided by each further constrained model with the previous one. These conclusions are significantly related to the existing knowledge about the behavior of diffusion in tissues, where the biexponential approach through the IVIM theory is preferred in medical imaging research to explain the behavior of water molecules in tissues like tumors, where not only a cellular component but also a microvascular behavior is appreciated.

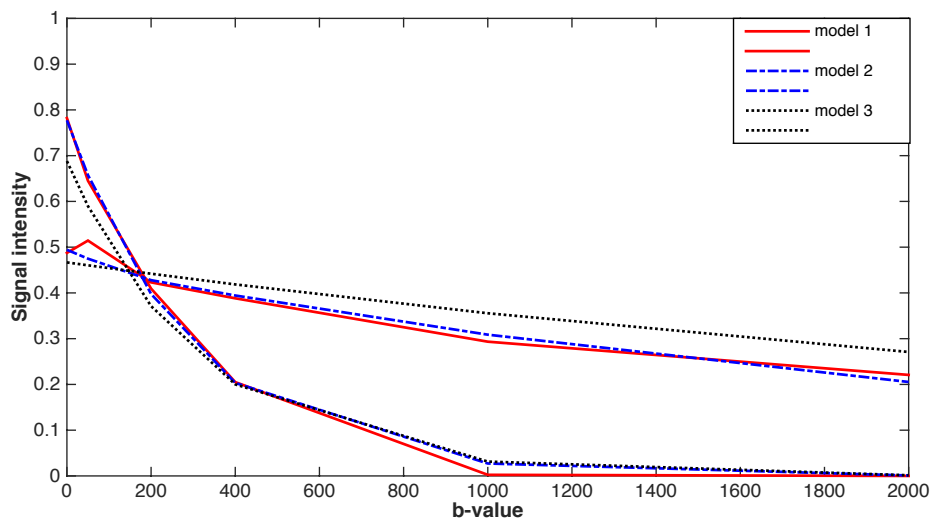


**Figure 33. Comparison between the behaviors provided by models 1 (solid red line), 2 (dashed blue line), and 3 (dotted black line).**

Figure 33 summarizes both modeled behaviors ( $d_1$  and  $d_2$ ) obtained from Models 1, 2, and 3, and figure 34 shows the distribution maps for these models. In all three models, the fast diffusion component presents an exponential decay, even in Model 1 where no shape is imposed. Regarding the slow diffusion component, it also presents an exponential decay after removing the artifact present at low b-values (Models 2 and 3). This can be seen in figure 35, where the higher residuals of Model 3 related to low b-values match this artifact in Model 1. Therefore, the pixels mainly related to this phenomenon are those having higher (negative) residuals in Model 3, as shown in figure 34, third column, third row. On the other hand, the distribution maps observed in figure 34 allow comparing all three models. As can be seen, there are slight but appreciable differences between them, as we move from Model 1 to 3.

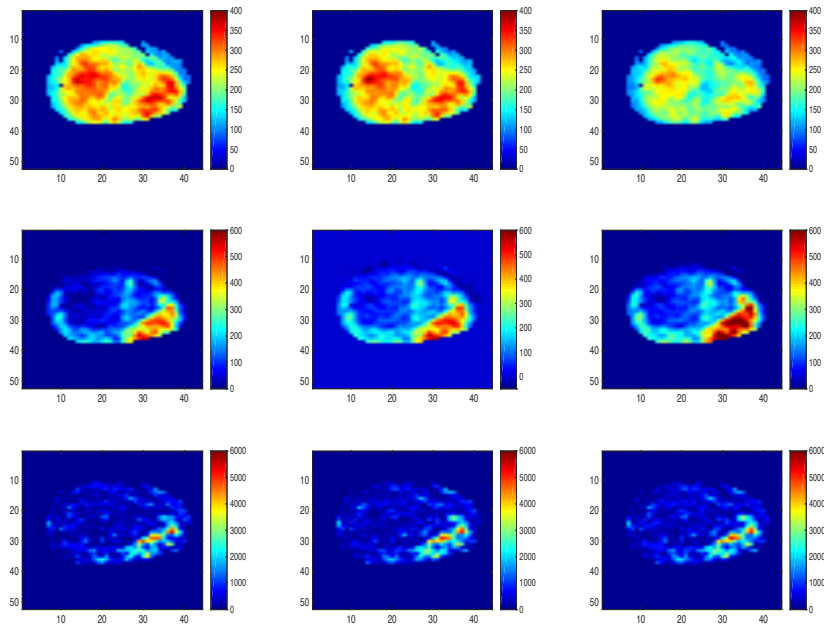


**Figure 34. Comparison between the distribution maps provided by the three different models. (Top)  $d_1$  related to slow diffusion, as the main behavior of normal prostate tissue. (Middle)  $d_2$  related to fast diffusion, related to highly vascularized regions, as tumors in the peripheral gland, like in this patient with a tumor in the peripheral gland. (Bottom) RSS distribution maps. (Left to right) Models 1, 2, and 3.**

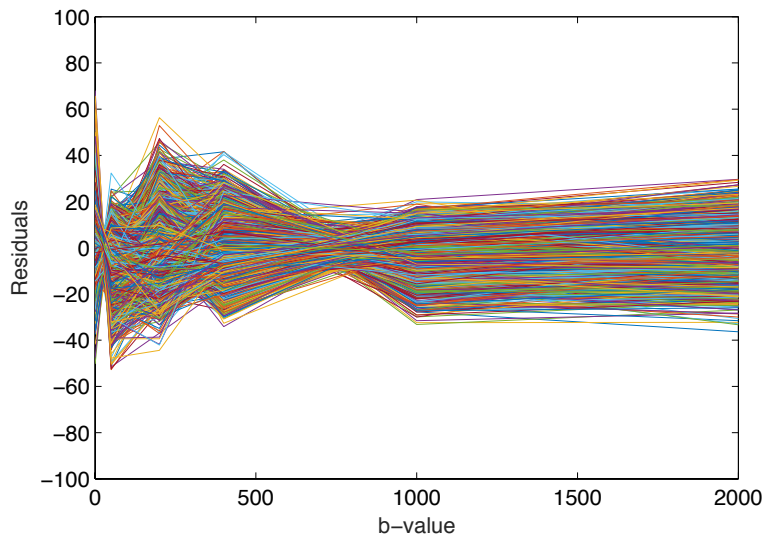


**Figure 35. Plot of the residuals obtained from Model 3 vs the b-values.**

This way, the proposed procedure provides adequate imaging biomarkers based on the biexponential model, which complement the IVIM biexponential model, using the distribution maps as a quantification of each behavior gathered in  $\mathbf{S}$  matrix at each pixel location. Still, both the MCR-based modeling and the theoretical biexponential modeling show two basic differences: first, the normalization of the spectra and second, the fact that the two factors weighting the exponentials do not have to be necessarily complementary. Furthermore, the fitting of the IVIM model is fitted pixel-by-pixel, unable to take profit of the global information that can be obtained using MCR models.

Once the way to calculate the different biomarkers from clinical approaches (*chapters 2.3 and 2.4*) and latent variable statistical models (*chapters 4.2 and 4.3*) has been defined, the next step is to prove their ability to detect and classify prostate tumors. In the next chapters, PLS-based methods [83-84] are proposed in order to separate and classify ROIs selected by the specialists and associated to healthy tissue in the peripheral zone (HP) or dominant lesions (DL) with different grades of aggressiveness (Gleason, [13]). First, the capability of perfusion-based imaging biomarkers to detect and differentiate the cancerous tissue from the healthy tissue [115] will be analyzed. The procedure and results are explained in chapter 5. And finally, in chapter 6, a method where all the biomarkers from all the explained techniques are combined and introduced in one single PLS-based model (SMB-PLS [93-95]) will be applied in order to detect and differentiate tumor aggressiveness. To do that, a pixel-by-pixel spatial registration method (*chapter 3.3*) is proposed with the objective of ensuring the spatial coherence between the techniques.



# Chapter 5

## Perfusion biomarkers comparison for cancer detection

In this chapter, the capability of imaging biomarkers obtained from multivariate statistic methods (MCR-perfusion) in combination with biomarkers from first and second generation pharmacokinetic models for improving prostate tissue classification has been studied using partial least squares-discriminant analysis (PLS-DA) [83-84] and variable selection.

The considered MCR-perfusion imaging biomarkers [88, 90] are the ones obtained in chapter 4.2 for the perfusion process (NT, VT and the RSS from the MCR model; i.e. the values per pixel obtained in the **C** matrix). Excluding the artificial CMA dynamic because of its lack of physiological significance, and the A type dynamic because this analysis is performed only in the local area of the prostate (MCR perfusion local modeling).

Regarding the pharmacokinetic models, following the biomarker calculation method explained in chapter 2.3.4, three biomarkers are obtained in the case of the Tofts model ( $K^{trans}$ ,  $k_{ep}$ ,  $v_e$ ), since no greater differences were found between Tofts and Tofts extended model. Thus, the simpler version is applied in this chapter. When considering second generation models, four biomarkers were calculated ( $F_p$ ,  $PS$ ,  $v_e$ ,  $v_p$ ). Moreover, for the reasons previously commented in section 2.3.4, RSS has been used as a complementary imaging biomarker, in order to provide information about how well the pixel is fitted by the assumed model.

## **5.1. Biomarker structure organization**

Once the biomarkers are obtained, we arrange them together into a valid structure in order to apply PLS-DA methods.

Firstly, the input matrices ( $\mathbf{X}$ ,  $\mathbf{Y}$ ) for the PLS-DA model have been built using the biomarker images obtained from the different approximations, i.e. pharmacokinetic or MCR models. The  $\mathbf{X}$  matrix is constructed by stacking all the selected pixels in rows with the value of the different considered biomarkers in columns. The selected pixels are the ones defined by the radiologists as DL (lesion) or HP (healthy) ROI's for each patient. These ROI's are logical images (binary masks) associated to one specific slice of the prostate. Thus, the  $\mathbf{X}$  matrix is constructed by stacking all the pixels assigned at the corresponding local image for all the patients. For the same pixels, a 2-column  $\mathbf{Y}$  matrix is defined with two dummy variables (0–1). The first column defined the “DL” variable (value 1 if the pixel belonged to the “DL” region and value 0 otherwise). The second column defined the “HP” variable and is built complementary to the first one. From this model, the class showing higher value is assigned to the corresponding pixel.

## **5.2. Goodness of prediction parameters: f-score, precision and recall**

In the  $\mathbf{Y}$  matrix, the assigned category of the pixels has been compared with the original classification. Therefore, if the pixel belongs to HP, it can be evaluated as a TN (True Negative) or FP (False Positive) depending on the prediction, and as a TP (True Positive) or FN (False Negative) if it is DL. Then, two different parameters, precision and recall, are calculated from the percentage of TP, FN and FP:

$$\mathbf{precision} = \frac{TP}{TP+FP} \quad \mathbf{recall} = \frac{TP}{TP+FN} \quad \text{Equation 5.1}$$

Both indexes are combined in a new performance index, f-score, chosen to evaluate the classification model performance. The f-score [116] is defined as the weighted harmonic mean of these two parameters:

$$\mathbf{f - score} = \frac{2 \cdot \mathbf{precision} \cdot \mathbf{recall}}{\mathbf{precision} + \mathbf{recall}} \quad \text{Equation 5.2}$$

This parameter determines the goodness of prediction for a classification model. It ranges between 0 and 1, and takes the maximum when the precision and recall are one

(the number of FP and FN are zero). The closer the f-score is to one, the better the model is in terms of prediction.

### **5.3. Variable selection and classification method**

The variable selection method proposed in this thesis (fig. 36) is a wrapped double cross-validation (2CV) with variable selection, showing high similarities with other 2CV methods [117, 118]. This methodology is applied in order to determine which parameters supply relevant information for classification. This way, the variable selection method allows removing all non-informative variables improving the classification performance (misclassifications rate based on the f-score).

The method consists in dividing the pixels from the cases of the data set (30 patients for this analysis) in three randomized groups of cases (i.e. 10 patients), defined as training, validation and test. All the pixels from each case have their own class identification (DL or HP) and are located in their corresponding group. Therefore, the pixels from a specific case are always included in the same group in order to avoid any type of overfitting. Moreover, the number of pixels in each category has been balanced as much as possible in order to avoid any bias of the model.

The method performs as follows: starting from a number of latent variables (NLV) equal to one, the training set is used for PLS-DA model building, using all the variables (biomarkers) of the considered pharmacokinetic or MCR model. Then, projecting the validation set onto the model fitted with the training set, an initial f-score (0) is calculated evaluating the performance in the model classification.

The f-score (0) is stored and then, the values of the  $B_{PLS}$  coefficients for each variable are compared with their “null” distribution obtained after breaking the correlation structure between  $\mathbf{X}$  and  $\mathbf{Y}$  of the training set. This breakage process consists of randomizing the order of the  $\mathbf{Y}$  matrix rows keeping the same  $\mathbf{X}$  and building a PLS-DA model to obtain the “null” model coefficients. This is internally repeated 500 times in order to obtain the null distribution [117, 118] of these coefficients. This way, the variable (biomarker) is removed from the  $\mathbf{X}$  matrix if the coefficient of a certain variable is not statistically significant. It is considered statistically significant if the real coefficient is out of the central 95% range for the random null distribution values (i.e.  $\alpha=0.05$ ).

Once all the non-statistically significant variables are removed, a new PLS-DA model is built with the remaining significant variables from the training set  $\mathbf{X}$  matrix, obtaining a new value of f-score (1) after projecting again the same validation set (only using the remaining significant variables) onto the new PLS-DA model. If the new f-score (1) is higher than f-score (0), the model is improved and the new value of f-score (1) is updated. In this case, the iterative process continues with a new variable selection

comparing the new  $B_{PLS}$  coefficients after breaking again the correlation structure between  $\mathbf{X}$  and  $\mathbf{Y}$ . However, if f-score (1) is lower than f-score (0), the best model is the one considered in the previous step. This iterative process is repeated until the f-score (n) is lower than the one obtained in the previous step, f-score (n-1); keeping this “best” model with its associated f-score (n-1) and its own variable selection. From the best model, a final external set (test) is projected onto this model obtaining the “final f-score”. This value is stored for further comparisons.

Afterwards, the NLV is increased in one, repeating the same process explained for one NLV. This way, at the end we obtain N-1 (where N is the initial number of variables considered in the  $\mathbf{X}$  matrix) improved models (with its own variable selection) and with their associated value of NLV and final f-score. After this, the final f-score of these N-1 models are compared and the highest final f-score determines the best model with the best variable selection. Note that if different models provide the same value of final f-score, the most parsimonious model is preferred for simplicity.

Once this process is completed, the initial groups (training, validation and set) are permuted (P) in the three possible different combinations (i.e. training to validation, validation to test and test to training) ensuring that every case belonged, at least, one time to each group. So far, it must be strengthened that this means all pixels belonging to one case are only considered as training, validation or test; hence performing a real clinical situation, where a new patient has to be diagnosed according to some previous clinical knowledge or model, after some analyses.

Then the iterative process is repeated again with the new groups, obtaining, at the end, three different improved models. Finally, the initial group randomization is repeated 500 times obtaining ( $500 \times 3 = 1500$ ) different data organizations. This scheme is shown in figure 36.

At the end of the process, the value of the final f-score, the variable selection (biomarkers that remain in the model), the percentage of TN, TP, FN, FP and the related NLV for this “best” model obtained for each distribution of the groups (1500) are stored.

Once the process is finished, the variable relative inclusion rate (percentage of times a variable is included from a pharmacokinetic, MCR or combined model) is evaluated as an additional indicator.

In order to show summarized and consistent results, the analysis is simplified selecting the highest 5% final f-score models. Also, as an additional constraint for this “5% selection”, the percentage of FN is limited to 20%, considering it as excessively high FN percentage for tumor detection.

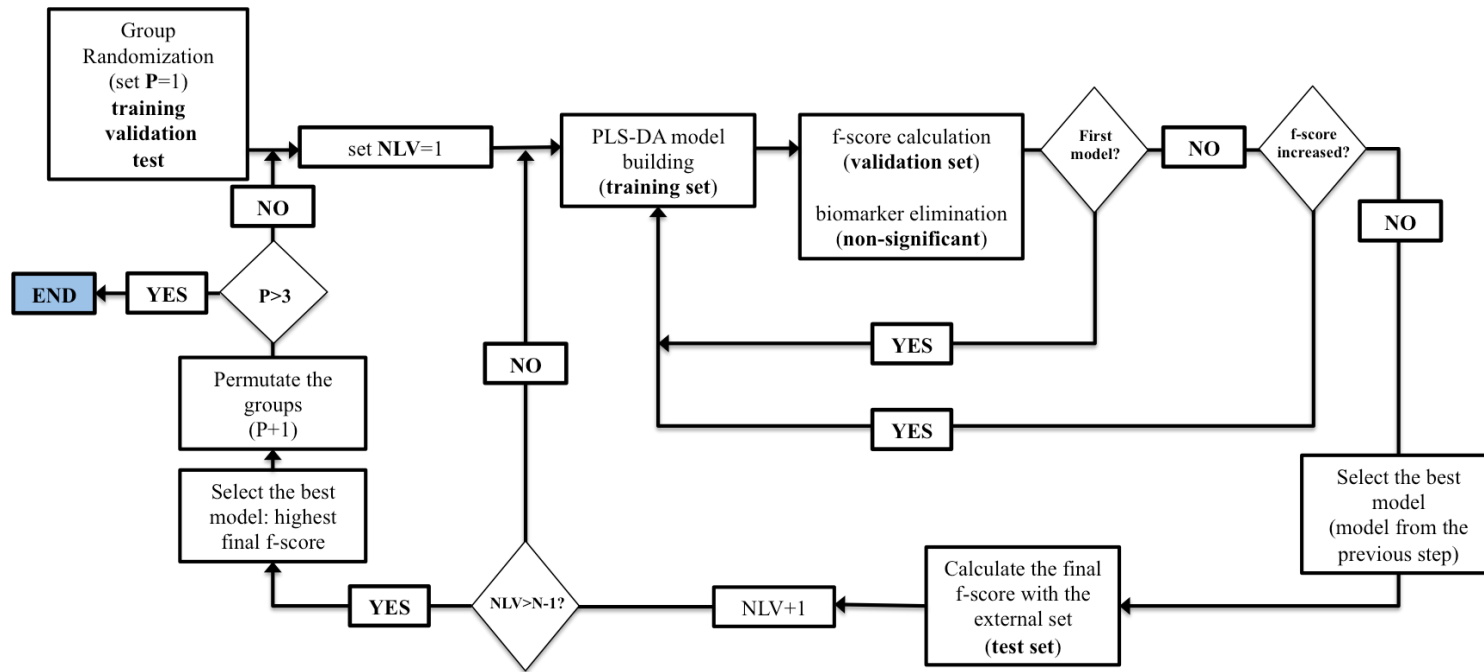


Figure 36. Variable selection process scheme, repeated 500 times to obtain the results for each proposed model. P represents the number of the three different group permutations proposed and NLV is the number of latent variables for PLS-DA.

#### 5.4. Results and discussion

The pharmacokinetic and MCR models have been evaluated, individually and in combination, in order to improve the results with different types of biomarkers. This way, the number of columns of the **X** matrix may vary depending on the number of biomarkers of the selected models. Table 3 shows the results:

**Table 3. Results summary for each considered model or models combinations using the 5% best models according to the final f-score. The best biomarkers were selected in terms of inclusion rate.**

Model	Max f-score	Mean f-score	Mean %FP	Mean %FN	Best biomarkers (Inclusion rate)
TOFTS	0.7871	0.7302	20.7	14.6	RSS, $v_e$ (80%) Others (<60%)
AATH	0.8125	0.7530	16.8	13.2	RSS (95%) Others (80%)
2CXM	0.8187	0.7556	15.4	13.6	Fp RSS (90%) Others (50-60%)
DP	0.8318	0.7455	16.1	14.7	RSS (100%) Others (<60%)
MCR	0.8145	0.7857	7.5	13.5	Type VT (95%) Type NT (100%)
MCR + 2CXM	0.8162	0.7789	9.2	13.9	MCR (>90%) 2CXM (50-70%)
MCR + AATH	0.8388	0.7804	9.6	12.6	MCR (>90%) AATH (60-70%)
MCR + DP	0.8659	0.7725	10.1	13.8	MCR (>90%) DP (60-70%) RSS DP (90%)

Three one-way ANOVAs have been proposed to study the statistical effect of the model on f-score, %FP and %FN by means of the Least Significant Difference (LSD) Intervals (figs. 37–39), respectively.

As can be seen in the figures, statistical significant differences are observed between the proposed models for the mean f-score and %FP (figs. 37 and 38). However, no statistically significant differences appear between FN rates, as can be seen in figure 39. Therefore, the ANOVA analyses show that the differences between the f-score are due to the differences in the %FP. Regarding the f-score and %FP, Toft's model (mean f-score of 0.73 and mean %FP of 20.7) performs significantly worse than two of the second-generation models (AATH and 2CXM), because their LSD intervals do not overlap, obtaining a mean f-score of 0.755 and a mean %FP of 15.4. Furthermore, second-generation 2CXM or AATH models are preferred over DP models due to the excessive computational time required to obtain the DP biomarkers, much higher than the other two second-generation models (6 times longer per pixel). Nevertheless, MCR alone or in combination with the best pharmacokinetic models obtained the best results for prediction, significantly better than any other types of model. This way, the mean f-score raised up to 0.7857 with 0.8145 as its maximum value, heavily reducing the rate of false positives (from 15.4% to 7.4%), which corresponds with 0.74 of sensitivity and 0.85 of specificity. These results are better than other studies including only first generation pharmacokinetic models [92, 119-122]. Additionally, no statistically significant differences were observed between the MCR and combined models. This suggests that using just MCR can be considered the best option for improving the f-score, since it is the most parsimonious model (i.e. adding the second-generation biomarkers do not improve statistically the classification results).

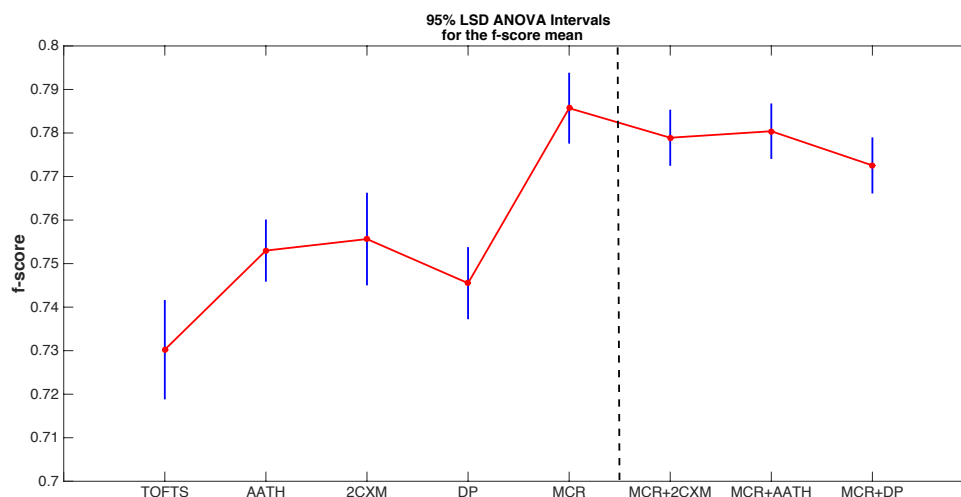
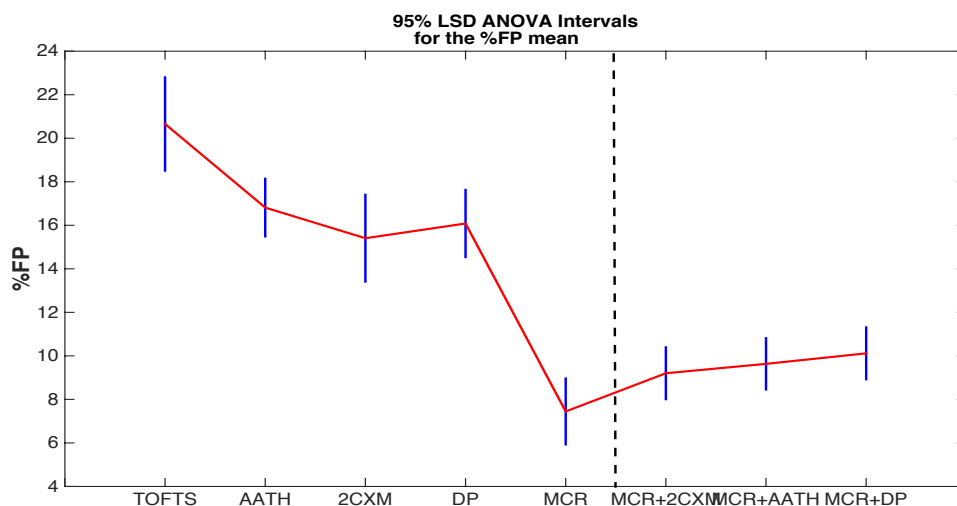
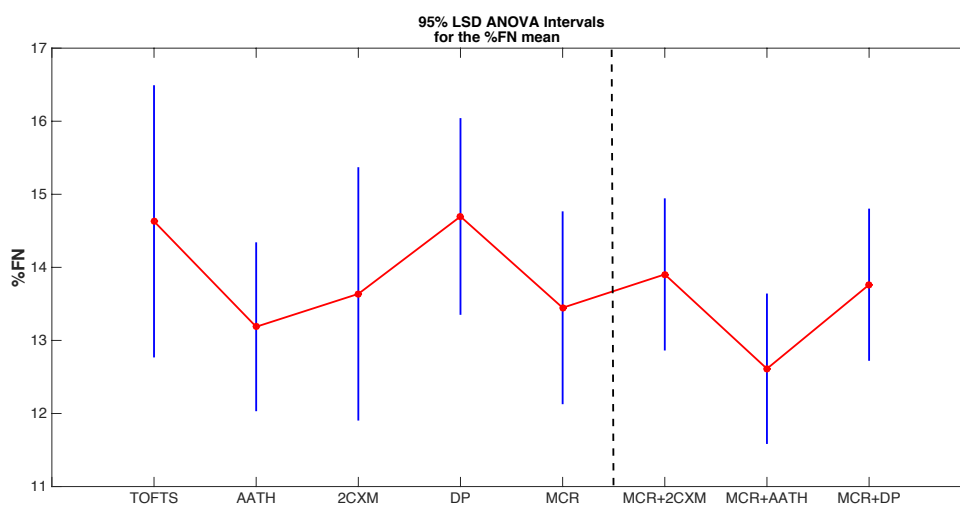


Figure 37. LSD ANOVA intervals for the f-score mean of the different individual and combined models ( $\alpha=0.05$ ) separated by the black dotted line.



**Figure 38. LSD ANOVA intervals for the %FP mean of the different individual and combined models ( $\alpha=0.05$ ) separated by the black dotted line.**



**Figure 39. LSD ANOVA intervals for the %FN mean of the different individual and combined models ( $\alpha=0.05$ ) separated by the black dotted line.**

Regarding the variable inclusion rate in the combined models, the MCR-ALS and the pharmacokinetic RSS variables have been included in more than 90% of the times, a much higher percentage in comparison with the 70% inclusion rate of the

pharmacokinetic biomarkers. This result suggests that pixels that do not fit the models properly (high RSS) should be considered as potential locations for abnormal vascular behaviors. They could be related to the presence of a tumor, and could be used as a surrogate indicator in order to locate lesions (i.e. a new biomarker). This finding needs further validation. Additionally, the RSS parameter can be used as an indicator of how reliable the provided pharmacokinetic biomarkers are, so that pixels that are not well fitted by the model should be considered as “outliers” that cannot be estimated (the values of the biomarkers won’t be reliable) by this specific pharmacokinetic model.

With regard to the goodness of prediction parameters, the classification index (f-score) parameter was selected because it is a balanced combination of the parameters that need to be minimized for improving the classification goodness (rates of FN and FP), but other indexes can be used instead (e.g. AUROC, area under the receiver operating characteristic curve, a common quality index in medicine). Both parameters are used in the field [123-125] and provide equivalent information. However, f-score is preferred in this work due to its simplicity and independence from the number of TN. The comparison of both figures-of-merit is not performed in this chapter, but the f-score vs sensitivity and specificity, which are directly related to the AUROC, will be compared in chapter 6. Also, the method proposed in this work is a combination of 2CV with variable selection, and could be tested by comparing the results with other variable selection methods (e.g. Variable Importance in Projection (VIP), Least Absolute Shrinkage and Selection Operator (LASSO) or selectivity ratio) [126-128]. Therefore, the method proposed in this chapter can be complemented making a comparison between different techniques and indexes for selecting the one that provides the best results.

Out of the pharmacokinetic models proposed, AATH has showed up as the best one, whereas the DP model is discarded due to the high computational time, and 2CXM is less consistent in comparison with AATH. These second-generation models have performed better for tumor detection than classical Tofts models, as demonstrated by the higher values of f-score. Also, RSS has risen as a potential biomarker in terms of inclusion rate. Nevertheless, the use of imaging biomarkers from MCR-ALS methods has provided better results than the DCE-MRI pharmacokinetic approximations for pixel-wise classification. The MCR dynamic behaviors (NT and VT) and the RSS were most of the times statistically significant, being the best biomarkers for lesion detection and tissue.

With regard to the limitations of the method, only perfusion biomarkers have been tested for discriminating tumors. The results can be complemented or improved by applying the same methodology with diffusion biomarkers or with both techniques in combination, as performed in chapter 6 for aggressiveness.

Besides, the application of this method is based in a pixel-level approximation, in contrast with the “truth” obtained from the biopsy, which is a qualitative value assigned to the whole ROI. Therefore, with this “gold standard”, the pixel-level cannot

*Application of multivariate image analysis to prostate cancer for improving the comprehension of the related physiological phenomena and the development and validation of new imaging biomarkers*

---

be discriminated with high precision and the values of f-score will be always below the value they can reach. This perspective has been changed in chapter 6, where the objective is to discriminate ROIs instead of pixels, easing the classification.

# Chapter 6

## Study of aggressiveness by combining different MRI sequences

As seen in the last chapter, perfusion MCR imaging biomarkers can discriminate between healthy and cancerous tissue in the prostate. But when trying to distinguish between different levels of aggressiveness (based on the Gleason scale [13, 16]), only one MR technique (source of information) is not enough for obtaining good results. Therefore, the necessity of providing acceptable rates of sensibility/specificity forces to combine different techniques (perfusion, diffusion and T2w) in order to take advantage of the different sources of information available. However, one problem arises when combining MR imaging biomarkers obtained from different sequences, taken at different time or positioning, known as the “alignment problem”. When using different types of sequences, it is not possible to ensure that the location of each pixel of e.g. the diffusion sequence corresponds exactly to the same pixel in the perfusion sequence (it might happen due to movements, change of resolution, different position of the patient, etc.). In order to solve this alignment problem, it is mandatory to apply image registration methods as the one proposed in chapter 3.3.

### 6.1. Data structure organization

In this chapter the goal is to discriminate aggressiveness. Following the ROI characterization method explained in chapter 3.1, DL ROIs are divided in two groups: LA (Low aggressiveness) and HA (High aggressiveness).

Regarding the imaging biomarkers (*see chapters 2.3, 2.4 and 4*), the calculation is performed using the output of the registration method (diffusion and normalized T2w) and the reference sequence (perfusion). The considered models are:

1. From clinical diffusion: Monoexponential, IVIM (the segmented version).
2. From statistical latent variable methods: MCR-Diffusion.
3. From pharmacokinetic perfusion: Extended Tofts (contrarily to chapter 5, extended contribute with more information in this case), AATH, 2CXM.
4. From statistical latent variable methods: MCR-Perfusion.
5. From T2w sequence: T2 muscle-normalized signal (only the signal, not an actual model).

The data block structure obtained from the previous models is summarized in table 4. Contrarily to chapter 5, this work is focused on discriminating ROI's instead of pixels. However the biomarkers cannot be applied directly because they have an individual value per pixel. In order to characterize the ROIs, this thesis calculates some statistical parameters for each biomarker using the pixel values of the whole ROI and obtaining an individual value, globally associated to the lesion. The calculated statistical parameters are: mean, median, standard deviation, P25, P75, skewness and kurtosis (where P25 and P75 are the percentile 25% and 75% respectively).

Once the biomarkers and the statistical parameters are calculated, data is arranged as in chapter 5, building a valid structure for applying multivariate statistical discriminant models like, in this case, SMB-PLS [93-95] in a discriminant version. Multiblock methods were applied in this chapter because of its ability to separate the information block-by-block instead of selecting individual variables, no matter which type of sequence (DCE or DW) or technique (clinical models or MCR) they came from. The aim of this chapter is to determine if all the blocks are necessary or some of them can be removed, for some positive reasons:

- Reducing the time computation.
- Removing the most patient invasive and expensive techniques (like perfusion) from the MR image protocol.

This multiblock model is preferred to other multiblock approximations [101-103] because of its ability to extract orthogonal information for each block in a consecutive way (block-after-block), grouping the correlated information or discarding the unnecessary latent variables. This way, it is possible to detect those truly relevant blocks in the tumor aggressiveness differentiation and, after that, remove the ones that do not supply additional discriminating power with respect to the previous blocks.

**Table 4. Data block structure. The number of variables is obtained after multiplying the ROI statistics (mean, median, variance, P25, P75, skewness, kurtosis), by the number of biomarkers provided by each perfusion or diffusion model.**

Blocks	Models	Imaging biomarkers	# variables
(1) Model-based DWI	Monoexponential, IVIM	ADC, D, D*, f, RSS	42 (6x7)
(2) MCR-Diffusion	MCR-ALS (Diffusion)	d <sub>1</sub> , d <sub>2</sub> , RSS	21 (3x7)
(3) Model-based DCE	Extended Tofts, AATH, 2CXM	K <sup>trans</sup> , k <sub>ep</sub> , v <sub>e</sub> , v <sub>p</sub> , F <sub>p</sub> , PS, RSS	105 (15x7)
(4) MCR-Perfusion	MCR-ALS (Perfusion)	NT, VT, RSS	21 (3x7)
(5) Normalized T2w	-	Muscle-normalized T2w	7

The input matrix  $\mathbf{X}$  is arranged in 5 blocks of variables ( $B=5, [\mathbf{X}_1 \dots \mathbf{X}_5]$ ) according to table 4, where the rows are assigned to the ROIs. Matrix  $\mathbf{Y}$  is defined with two columns of dummy variables (1,-1) for the same ROIs. The first column defined the “LA” variable (value 1 if the ROI is a lesion with low aggressiveness and -1 if it shows high aggressiveness). The second column is the “HA” variable and is built complementary to the first one.

The final database is composed of 36 lesion ROIs in a balanced way (18 LA and 18 HA) from 36 different biopsied patients.

## 6.2. SMB-PLS-DA iterative procedure method

The method proposed takes the basic idea of the SMB-PLS [93-95] model of extracting only the relevant latent variables from each block. But in this case, the variable selection method has not been treated in this thesis because of two big issues:

1. The number of variables is way larger than the method proposed in chapter 5 and the computational time would be extremely long.
2. The variable selection does not provide a direct clinical interpretation, since the variables are not the original biomarkers but a group of different parameters calculated from them (they do not have an individual meaning). It

would be an interesting option only in the case where the variables obtained from the same biomarkers are selected (for interpretation purposes). Nevertheless, this study is established as further work in chapter 7.

Thus, we propose a model that considers the blocks as a unit of information and not the variables within each block individually.

The method consists in selecting two different balanced sets in a proportion 2/3 (24 ROIs) for training and 1/3 (12 ROIs) for validation for each iteration. First, it is necessary to establish the block configuration defined as the order the SMB-PLS model is taking the blocks for calculation (this sequential order will remain constant during the iterative loop represented in figure 40), and they are selected based on the knowledge about the sequences and the potential influence of the blocks in discrimination (i.e. clinically, diffusion is preferred over perfusion as the best technique for assessing tumor aggressiveness, and T2w is usually used as a complementary morphological image for improving clinical interpretation and diagnosis).

Therefore, among all the possible different configurations that can be analyzed in order to maximize the prediction performance, only the ones shown in table 5 have been treated as initial seeds comparing perfusion vs diffusion and clinical vs MCR-based, plus T2w; afterwards, new configurations have been checked removing some of the blocks based on the obtained results (table 7).

After that, the SMB-PLS model is calculated for the training set using simple cross-validation (CV) and a fixed number of latent variables (this thesis has considered 15 as the maximum possible number of latent variables for each block because after many simulations, the optimal number of components never surpassed this value). Then, the approach calculates the projection of this model onto the validation set obtaining the goodness of prediction parameter  $Q^2$  for the  $\mathbf{Y}$  matrix at each number of latent variables. The number of optimal latent variables is that maximizing the  $Q^2$  (validation) of the projection of the model onto the validation set. Hereafter, the model is recalculated with the selected number of latent variables for that specific block using the validation set, and then, the same procedure is applied for the next block until all the blocks are included (or not) in the model with their respective number of optimal latent variables. It should be noted here that a double cross-validation procedure, with a training, validation and (external) test set, would have been preferred, but it was not possible to apply it because of the reduced sample size.

Once the optimal model is calculated, the final prediction of the validation set is calculated (the highest positive value for each column is determined as the predicted class for each ROI). Comparing it with the original true validation set, we can obtain the number of TP, TN, FP and FN and, therefore, calculate the different values for the figures-of-merit (f-score, sensitivity and specificity). These additional parameters are defined as follow:

$$\text{sensitivity} = \frac{TP}{TP+FN} \quad \text{specificity} = \frac{TN}{TN+FP} \quad \text{Equation 6.1}$$

This iterative process is repeated 500 times. An scheme is shown in figure 40.

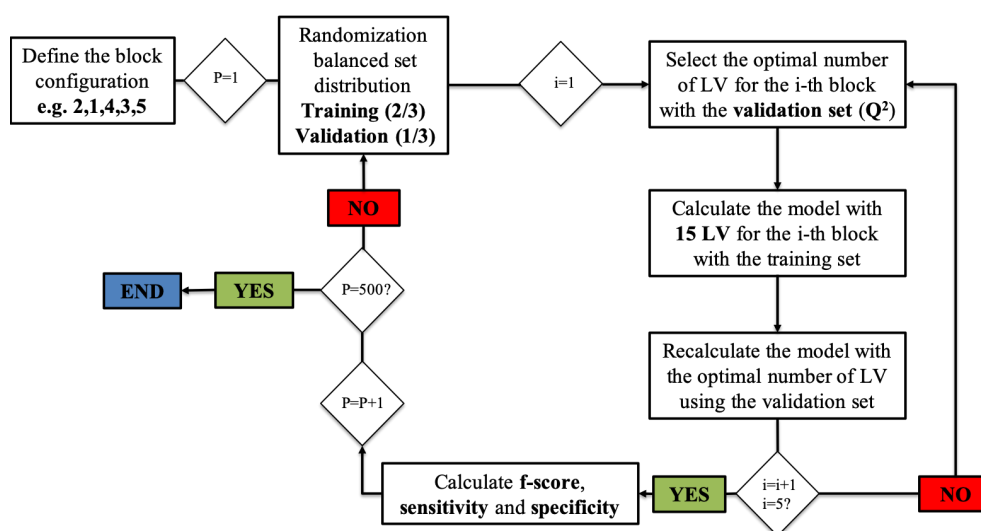


Figure 40. SMB-PLS iterative process scheme for each blocks configuration, repeated 500 times to obtain the results for each proposed model. P represents the number of the iteration and “i” corresponds to the block in the i-th position (1 to 5) in the configuration. LV is referred to the number of latent variables. The block identifier is defined in table 4.

At the end of the process, the value of the final f-score, selectivity, specificity, goodness of prediction  $Q^2$ , the percentage of TN, TP, FN, FP and the selected LV for each block of the “optimal” model obtained for each distribution of the groups (iteration) are stored.

Finally, the process is repeated again with the next configuration, obtaining, at the end, another improved model for each iteration (500).

### **6.3. Results and discussion**

As commented before, the iterative process is performed with different configurations in order to check and compare how relevant the block input order is. Then, the results of removing some blocks (or groups of information) are presented with the objective of studying how important the different MRI series (Diffusion, Perfusion and T2w) are. This study is important since if some blocks were not relevant at all, they could be removed. If that is the case, in future studies the computation time will be reduced and the model will become more parsimonious. Additionally, if good results can be obtained using only MCR-based models, the cost will be reduced because they do not require expensive high resolution equipment, which is not available at every hospital.

The results summary for each proposed configuration is shown in table 5.

**Table 5. Results summary for each proposed configuration, according to the maximum goodness of prediction  $Q^2$ . The f-score, sensitivity and specificity are calculated as the mean values. The code for the configurations is defined in table 4.**

<b>Configuration</b>	<b>f-score</b>	<b>Sensitivity</b>	<b>Specificity</b>
12345	0.7449	0.7771	0.7492
21435	0.7508	0.7834	0.7557
24135	0.7450	0.7804	0.7473
34125	0.6759	0.6997	0.6948
43215	0.7390	0.7707	0.7443

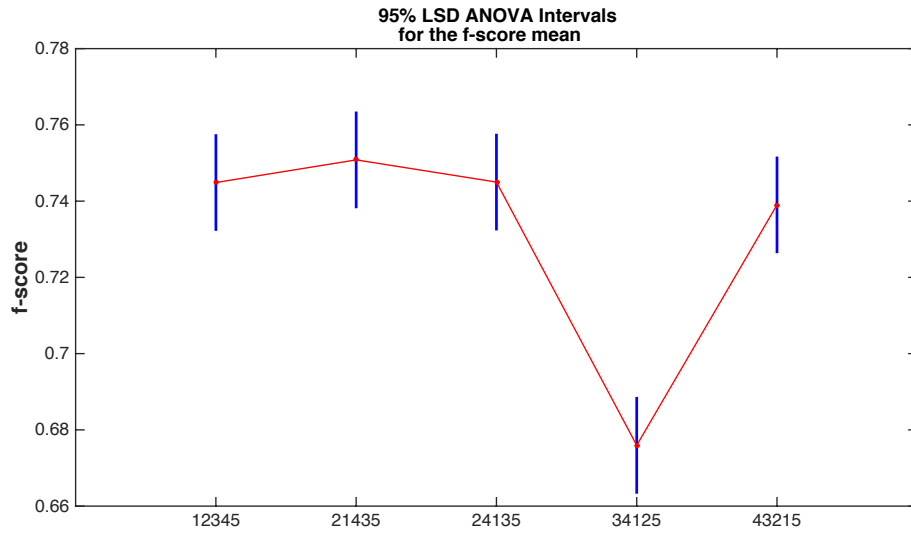
Besides, the prediction power (represented by the validation  $Q^2$ ) and the number of optimal LV selected for each block in terms of averages are shown in table 6.

**Table 6. Results summary for each proposed configuration. The  $Q^2$  and the number of optimal LV are calculated as the mean values. The code for the configurations is defined in table 4.**

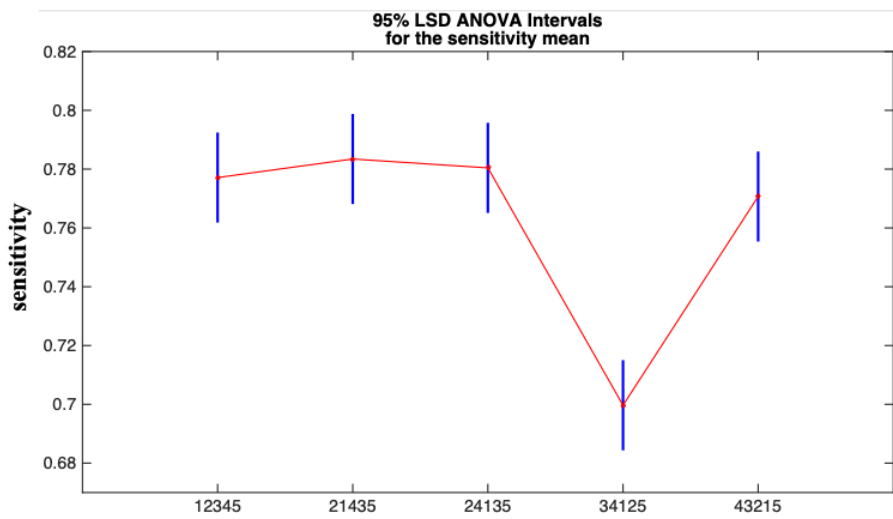
<b>Conf.</b>	<b>Average <math>Q^2</math></b>	<b>Average LV block (1)</b>	<b>Average LV block (2)</b>	<b>Average LV block (3)</b>	<b>Average LV block (4)</b>	<b>Average LV block (5)</b>
12345	31.96%	3.78	4.16	3.02	2.93	1.48
21435	33.70%	3.69	5.00	2.24	4.27	1.56
24135	33.15%	3.84	2.11	4.87	3.28	1.66
34125	18.52%	3.49	3.05	3.01	4.05	1.63
43215	30.79%	2.99	3.89	2.21	5.05	1.48
<b>Average results</b>						
-	29.62%	3.56	3.64	3.07	3.92	1.562

Table 6 gives a global view of the results. Respecting the number of LV, they decrease as the number of blocks increases because there is less orthogonal information left. It should be highlighted that both MCR (2 and 4) blocks are constantly represented with high number of LV, independently of the position they are sequenced.

Studying the parameters,  $Q^2$  percentage is higher when diffusion blocks (1,2) or MCR-blocks (2,4) are introduced first as happens with the f-score, sensitivity and specificity values. The greatest differences are observed only if the perfusion blocks are introduced first instead of the diffusion ones, where the values of  $Q^2$  are low (as the f-score is in table 5). The statistical significance of the differences is studied by applying ANOVA with 2 factors: the block input configuration and the validation set selection for each iteration (500 runs), used as a blocking factor for decreasing the variability and facilitating the appreciation of statistical significance differences. ANOVA LSD intervals of f-score, sensitivity and specificity are obtained for studying the statistical significance of the differences among the different configurations, figures 41, 42 and 43.



**Figure 41. LSD ANOVA intervals for the average f-score of the different block configurations ( $\alpha=0.05$ ). All the results are considered for performing the ANOVA. The code for the configurations is defined in table 5.**



**Figure 42. LSD ANOVA intervals for the average sensitivity of the different block configurations ( $\alpha=0.05$ ). All the results are considered for performing the ANOVA. The code for the configurations is defined in table 5.**

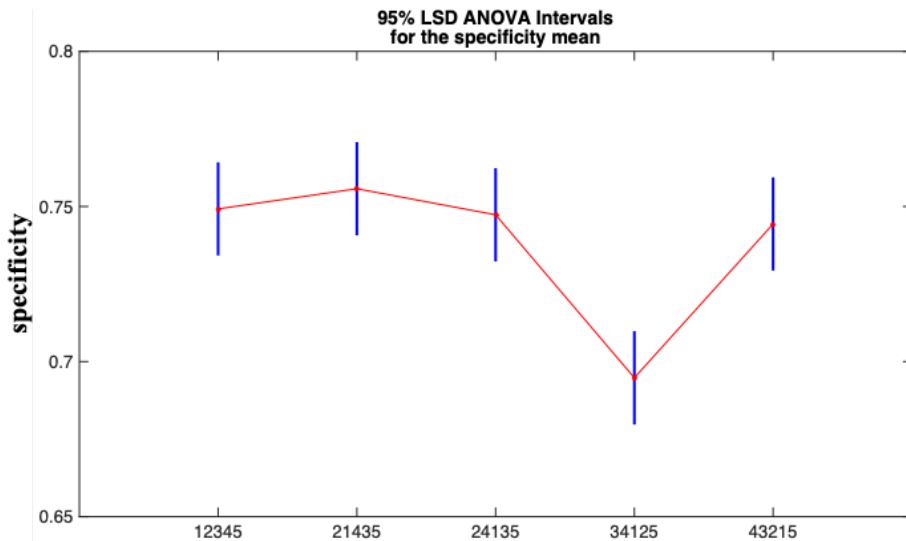


**Figure 43. LSD ANOVA intervals for the average specificity of the different block configurations ( $\alpha=0.05$ ). All the results are considered for performing the ANOVA. The code for the configurations is defined in table 5.**

As can be observed in figures 41, 42 and 43, there are not relevant statistical significant differences between the different configurations. However, when trying to prioritize pharmacokinetic perfusion models over the other blocks (the configuration 34125), the values obtained are significantly worse than the other configurations for all the parameters (f-score, sensitivity and specificity), losing prediction performance. This result can be interpreted as the pharmacokinetic models are not a good reference (starting point) in the algorithm for discriminating tumor aggressiveness.

Once the importance of the order has been analyzed, the next step is to remove some of the blocks from the iterative process and perform it again. First, both diffusion blocks (1 and 2) were removed. Then, the perfusion ones (3 and 4) and finally, the T2w block (5) was additionally removed for both scenarios. The aim is twofold: first, to replicate the same results with a more parsimonious model; and second, to study the relevance of each MRI technique in terms of performance to assess tumor aggressiveness. The result summary is shown in table 7. The LV selection summaries by block are shown in table 8.

**Table 7. Results summary for the models where one or various sources of information are removed, according to the maximum goodness of prediction  $Q^2$ . The f-score, sensitivity and specificity are calculated as the mean values. The code for the configurations is defined in table 4.**

Configuration	f-score	Sensitivity	Specificity
125 (without perfusion)	0.7579	0.7901	0.7527
345 (without diffusion)	0.5975	0.6194	0.5918
12 (only diffusion)	0.7027	0.7446	0.6862
34 (only perfusion)	0.5252	0.5397	0.5236
15 (clinical dif. + T2w)	0.7172	0.7516	0.7124
25 (MCR-dif. + T2w)	0.6983	0.7409	0.6961

Regarding the prediction power, as can be seen in table 8, the  $Q^2$  is clearly lower when diffusion is out of the models. T2w block seems to be important because the model losses prediction power if it is not included in the models. Besides, including T2w does not imply any additional cost when taking the acquisition because it is performed normally in the clinical routine.

**Table 8. Results summary for the models where one or various sources of information are removed. The  $Q^2$  and the number of optimal LV are calculated as the mean values. The code for the configurations is defined in table 4.**

Configuration	Average $Q^2$	Average LV 1 <sup>st</sup> block	Average LV 2 <sup>nd</sup> block	Average LV 3 <sup>rd</sup> block
125 (without perfusion)	31.36%	3.67	3.10	1.74
345 (without diffusion)	-5.09%	2.17	1.86	1.52
12 (only diffusion)	18.36%	2.59	1.36	-
34 (only perfusion)	-27.92%	1.66	0.82	-
15 (clinical dif. + T2w)	23.54%	3.02	2.21	-
25 (MCR-dif. + T2w)	21.91%	3.72	1.66	-

The ANOVA is performed as well for checking statistical significant differences (figs. 44, 45 and 46).

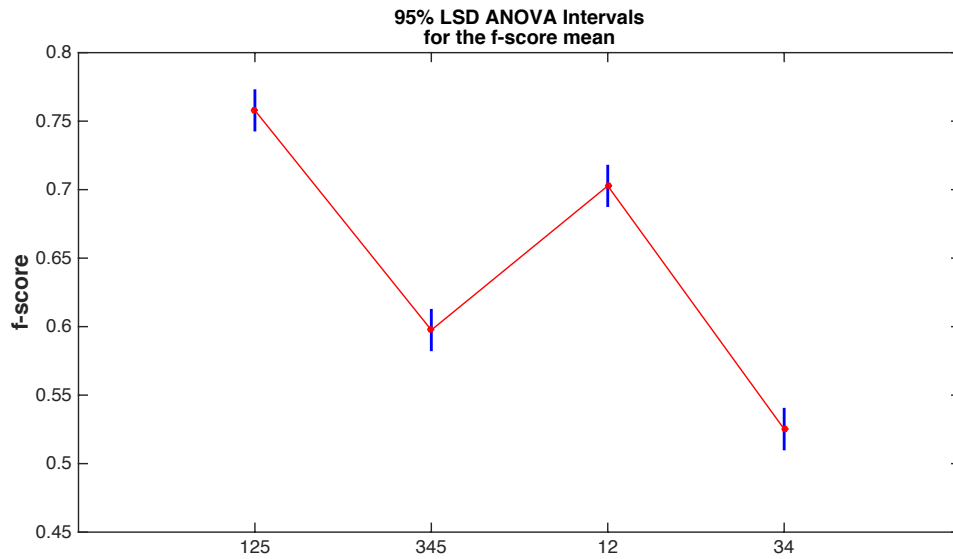


**Figure 44.** LSD ANOVA intervals for the average f-score of the different block configurations after removing some of them ( $\alpha=0.05$ ). All the results are considered for performing the ANOVA. The code for the configurations is defined in table 4.

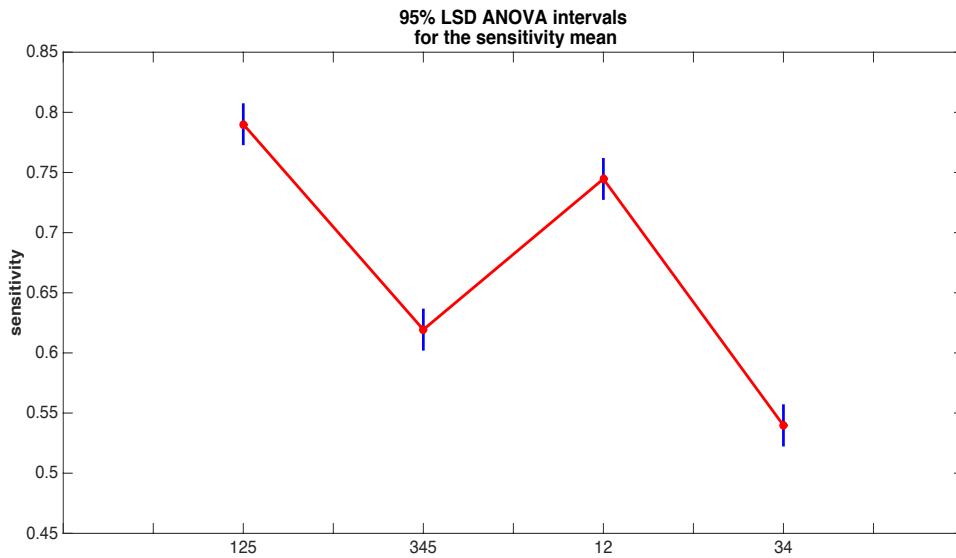


**Figure 45.** LSD ANOVA intervals for the average sensitivity of the different block configurations after removing some of them ( $\alpha=0.05$ ). All the results are considered for performing the ANOVA. The code for the configurations is defined in table 4.

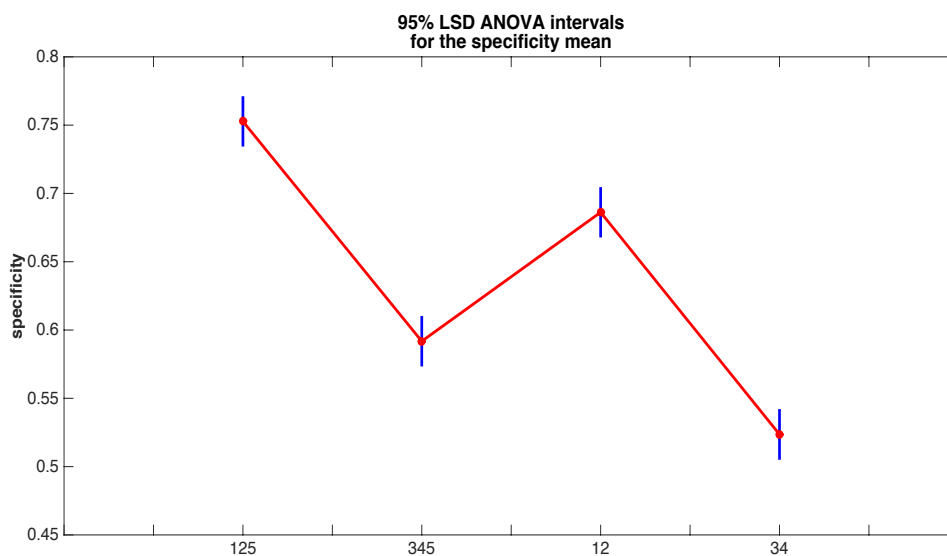


**Figure 46. LSD ANOVA intervals for the average specificity of the different block configurations after removing some of them ( $\alpha=0.05$ ). All the results are considered for performing the ANOVA. The code for the configurations is defined in table 4.**

In this case, there are relevant statistical significant differences ( $p\text{-value} < 0.05$ ) between the proposed sequences. First of all, diffusion blocks (1 and 2) cannot be taken out of the model because the f-score of sequences 345 and 34 are statistically significant worse than 125 and 12. Besides, the T2w block appears to be relevant and it improves the model when it is included (125 is statistically better than 12; and 345 is statistically better than 34). Similar results are observed when comparing sensitivity and specificity (figures 45 and 46).

Finally, in summary graphs (figures 47, 48 and 49), the results obtained when considering all the blocks or only few of them are compared.

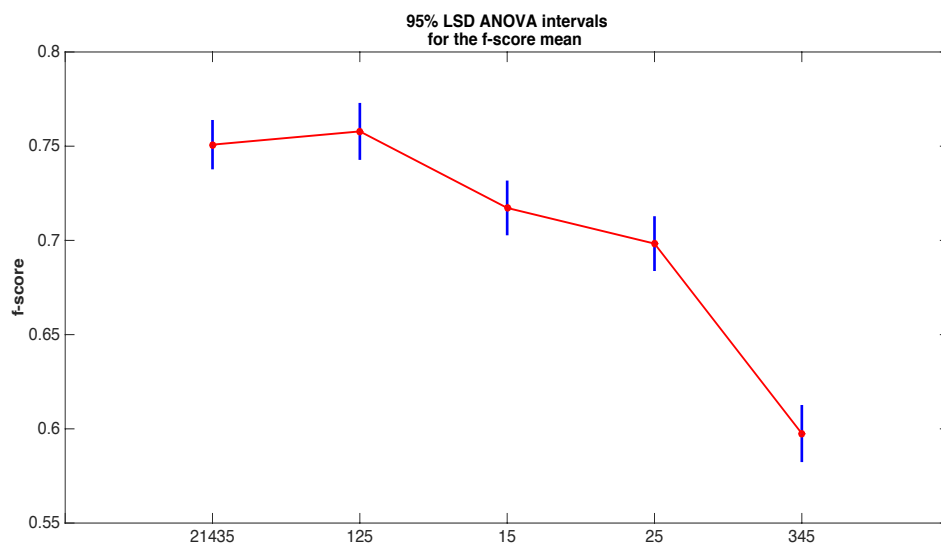


Figure 47. Summary plot of LSD ANOVA intervals for the average f-score ( $\alpha=0.05$ ). The code for the configurations is defined in table 4.

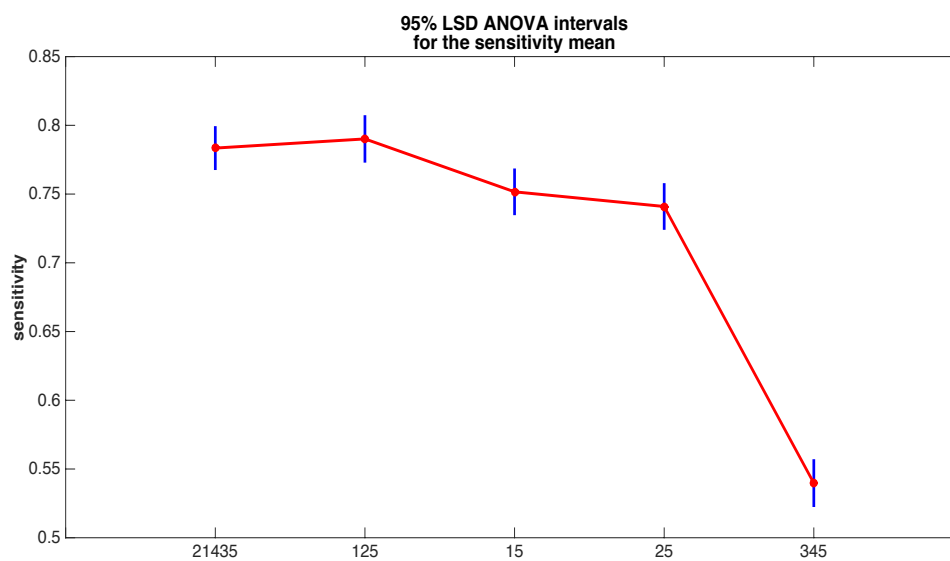
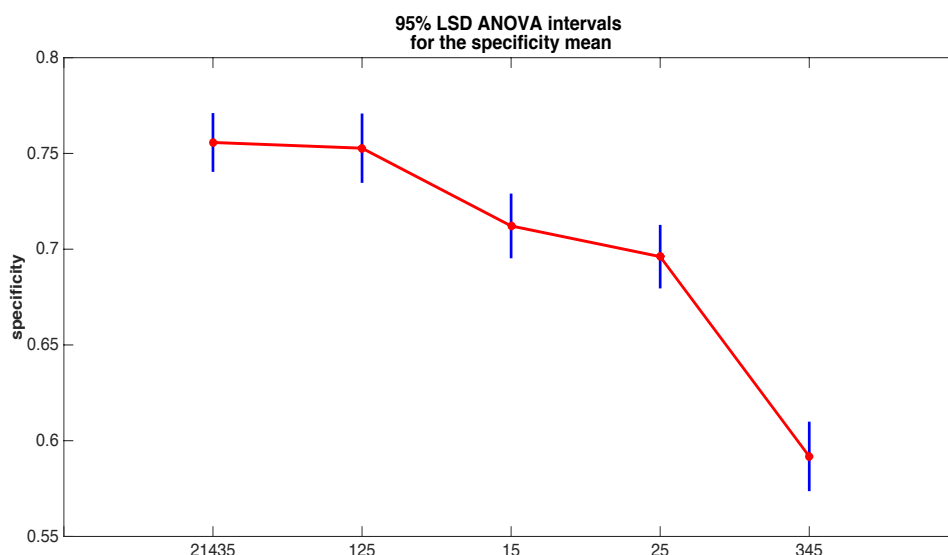


Figure 48. Summary plot of LSD ANOVA intervals for the average sensitivity ( $\alpha=0.05$ ). The code for the configurations is defined in table 4.



**Figure 49. Summary plot of LSD ANOVA intervals for the average specificity ( $\alpha=0.05$ ). The code for the configurations is defined in table 4.**

These results show up different and relevant ideas:

- First, they indicate that perfusion blocks (3 and 4) can be removed from the study, since they alone provide the worst results, and there are no statistical significant differences between the best models considering all the blocks and the models where only diffusion sequences and T2 images are used. This conclusion is relevant because perfusion is an invasive method for the patient, which is more harmful than diffusion and, furthermore, pharmacokinetic models need better equipment and higher temporal resolution to be well-estimated. Moreover, the computation time is way higher for perfusion pharmacokinetic models (approximately 1 day per patient) than diffusion (1 hour per patient) and even lower for MCR-based models (5 minutes per patient).
- Second, when trying to use only one of the diffusion blocks (15 and 25) the f-score is significantly worse than the combination of both (125). This result determines that blocks 1 and 2 are complementary and performs better together.

With regards to the limitations of the method, the database is relatively small (36 patients). For further validation, it should be increased with new characterized cases. Future studies including larger cohorts are necessary in order to assess the clinical significance and impact of the results obtained in this work. Besides, this analysis is

performed at the ROI level, which means that the level of detail and characterization is lower than the pixel level approximation, but the classification and the predictive power is increased (is easier to classify ROIs than pixels).

With respect to the algorithm, the method is in need of “a priori” knowledge in order to propose good and reliable input sequences of the blocks, which are introduced manually and it will become a problem when trying to automatize and generalize the method. Also, the number of iterations and maximum number of latent variables should be previously fixed attending to this “a priori” knowledge, guarantying that this value will be enough for obtaining reliable results without investing an unnecessary large amount of time.

From the results obtained, diffusion blocks (1 and 2) are the best sources of information for discriminating aggressiveness in prostate, and T2w block (5) cannot be ignored or discarded. Perfusion is not relevant as the same results without their blocks of information (3 and 4) are obtained. In this chapter, the inferior capability of perfusion quantitative analysis for grading tumor aggressiveness has been proved, as it provides less valuable information than diffusion and T2w. These results should be taken into account in future revisions of the MR image protocols in prostate. MCR models are always higher represented in their respective methods than the clinical models but the combination of the clinical and MCR diffusion methodologies and T2w provides the best results, which are extremely high for the best configuration (f-score of 0,76 and  $Q^2$  of 31,36%), these results are better than using only clinical approaches separately as in other studies [92].



# Chapter 7

## Conclusions

This thesis has studied and proved the capability of MCR models to extract behaviors with clinical meaning from DCE-MR and DW-MR images by including a priori knowledge through imposing constraints and meaningful initial guesses.

MCR models are able to directly locate and grade the intensity of these behaviors in the images, providing new imaging biomarkers, complementary to those obtained from the theoretical models, to improve clinical diagnosis.

MCR also helps in segregating those artifacts that may introduce uncertainty in the estimation of any biomarker, and provides an evaluation tool for assessing the appropriateness of theoretical models, with a data driven model methodology that allows incorporating the knowledge we have about the processes in a sequential fashion.

Perfusion based imaging biomarkers are capable enough in discriminating tumor from healthy tissues (DL vs HP), but they fail when going into a deeper level studying aggressiveness (LA vs HA).

In chapter 5, MCR-perfusion based biomarkers have shown up as better than the pharmacokinetic models ones for pixel-wise classification of DL vs HP areas. NT and VT parameters were almost always selected by the variable selection method. Out of the pharmacokinetic models, second generation performs better than first generation and AATH has shown as the best one.

In chapter 6, the combination of different techniques by applying registration methods and sequential multi-block PLS models (SMB-PLS) performed extraordinarily well, obtaining high f-score, sensitivity and specificity values for ROI-wise classification. When preparing the data, the order of sequencing the blocks in SMB-PLS is important as it affects the results of the study. Finally, for improving the models, it has been demonstrated that the perfusion blocks can be removed from the statistical models, as they did not improve the results obtained by diffusion and T2w based parameters alone. This result should be taken into account in future revisions of the MR image protocols in prostate.

# Chapter 8

## Further work

This thesis has left diverse open studies still to be approached. A list of the main and straightforward are listed below:

- Application of the variable selection method with SMB-PLS for studying tumor aggressiveness (as did in chapter 5 for lesion detection).
- Extrapolation of the MCR-biomarker calculation method to other organs (brain, breast, etc.).
- Study of diffusion from the anisotropic point of view with Diffusion Tensor Imaging (DTI) in breast cancer.
- To extent the current studies to a larger cohort in order to assess the clinical significance and impact of the results obtained in chapter 6.



# Chapter 9

## References

- [1] Heidenreich A, Bastian PJ, Bellmunt J, Bolla M, Joniau S, van der Kwast T, et al. EAU guidelines on prostate cancer. Part 1: screening, diagnosis, and local treatment with curative intent-update 2013. *Eur. Urol.* 2014; 65(1): 124-37.
- [2] Ferlay J, Steliarova-Foucher E, Lortet-Tieulent J, Rosso S, Coebergh JW, Comber H, et al. Cancer incidence and mortality patterns in Europe: estimates for 40 countries in 2012. *Eur. J. Cancer.* 2013; 49(6): 1374-403.
- [3] López-Abente G, Mispireta S, Pollan M. Breast and prostate cancer: an analysis of common epidemiological features in mortality trends in Spain. *BMC Cancer.* 2014; 14: 874.
- [4] Gil-Vernet JM. Prostate cancer: anatomical and surgical considerations. *BJU Int.* 1996; 78(2): 161-8.
- [5] Verma S, Rajesh A. A clinically relevant approach to imaging prostate cancer: review. *AM. J. Roentgenol.* 2011; 196 (3 Suppl): S1-10 Quiz S1-4.

- [6] McNeal JE. Regional morphology and pathology of the prostate. *Am. J. Clin. Pathol.* 1968; 49(3): 347-57.
- [7] McNeal JE. The zonal anatomy of the prostate. *The Prostate.* 1981; 2(1): 35-49.
- [8] McNeal JE. Origin and evolution of benign prostatic enlargement. *Investig. Urol.* 1978; 15(4): 340-5.
- [9] McNeal JE. Normal histology of the prostate. *Am. J. Surg. Pathol.* 1988; 12(8): 619-33.
- [10] McNeal JE, Redwine EA, Freiha FS, Stamey TA. Zonal distribution of prostatic adenocarcinoma. Correlation with histologic pattern and direction of spread. *Am. J. Surg. Pathol.* 1988; 12(12): 897-906.
- [11] Mai KT, Belanger EC, Al-Maghrabi HM, Robertson S, Wang D, Margnean C. Primary prostatic central zone adenocarcinoma. *Pathol. Res. Prac.* 2008; 204(4): 251-8.
- [12] Coakley FV, Hricak H. Radiologic anatomy of the prostate gland: a clinical approach. *Radiol. Clin. N. Am.* 2000; 38(1): 15-30.
- [13] Murphy GP, Busch C, Abrahamson PA, Epstein JI, McNeal JE, Miller GJ, et al. Histopathology of localized prostate cancer. *Consensus Conference on Diagnosis and Prognostic Parameters in Localized Prostate Cancer.* Stockholm, Sweden, May 12-13, 1993. *Scandinavian journal of urology and nephrology Supplementum.* 1994; 162:7; discussion 115-27.
- [14] Epstein JI, Allsbrook WC, Jr., Amin MB, Egevad LL, Committee IG. The 2005 International Society of Urological Pathology (ISUP) Consensus Conference on Gleason Grading of Prostatic Carcinoma. *Am. J. Surg. Pathol.* 2005; 29(9): 1228-42.
- [15] Ross HM, Kryvenko ON, Cowan JE, Simko JP, Wheeler TM, Epstein JI. Do adenocarcinomas of the prostate with Gleason score (GS)  $\leq 6$  have the potential to metastasize to lymph nodes?. *Am. J. Surg. Pathol.* 2012; 36(9): 1346-52.

- 
- [16] Gleason DF, Mellinger GT. Prediction of prognosis for prostatic adenocarcinoma by combined histological grading and clinical staging. *J. Urol.* 1974; 111(1): 58-64.
- [17] Albertsen PC, Hanley JA, Gleason DF, Barry MJ. Competing risk analysis of men aged 55 to 74 years at diagnosis managed conservatively for clinically localized prostate cancer. *JAMA.* 1998; 280(11): 975-80.
- [18] Wolters T, Roobol MJ, van Leeuwen PJ, van den Bergh RC, Hoedemaeker RF, van Leenders GJ, et al. Should pathologists routinely report prostate tumour volume? The prognostic value of tumour volume in prostate cancer. *Eur. Urol.* 2010; 57(5): 821-9.
- [19] Ruijter ER, van de Kaa CA, Schalken JA, Debruyne FM, Ruiters DJ. Histological grade heterogeneity in multifocal prostate cancer. Biological and clinical implications. *J. Pathol.* 1996; 180(3): 295-9.
- [20] Wise AM, Stamey TA, McNeal JE, Clayton JL. Morphologic and clinical significance of multifocal prostate cancers in radical prostatectomy specimens. *Urology.* 2002; 60(2): 264-9.
- [21] Karavitakis M, Winkler M, Abel P, Livni N, Beckley I, Ahmed HU. Histological characteristics of the index lesion in whole-mount radical prostatectomy specimens: implications for focal therapy. *Prostate Cancer Prostatic Dis.* 2011; 14(1): 46-52.
- [22] Borque A, Rubio-Briones J, Esteban LM, Sanz G, Dominguez-Escrig J, Ramirez-Backhaus M, et al. Implementing the use of nomograms by choosing threshold points in predictive models: 2012 updated Partin Tables vs a European predictive nomogram for organ-confined disease in prostate cancer. *BJU Int.* 2014; 113(6): 878-86.
- [23] Crawford ED, DeAntoni EP, Etzioni R, Schaefer VC, Olson RM, Ross CA. Serum prostate-specific antigen and digital rectal examination for early detection of prostate cancer in a national community-based program. The Prostate Cancer Educational Council. *Urology.* 1996; 47(6): 863-9.
- [24] Smith DS, Catalona WJ. Interexaminer variability of digital rectal examination in detecting prostate cancer. *Urology.* 1995; 45(1): 70-4.
- [25] Catalona WJ, Hudson MA, Scardino PT, Richie JP, Ahmann FR, Flanigan RC, et al. Selection of optimal prostate specific antigen cutoffs for early detection of

- prostate cancer: receiver operating characteristic curves. *J Urol.* 1994; 152(6 Pt 1): 2037-42.
- [26] Arcangeli CG, Ornstein DK, Keetch DW, Andriole GL. Prostate-specific antigen as a screening test for prostate cancer. The United States experience. *Urol. Clin N. Am.* 1997; 24(2): 299-306.
- [27] Epstein JI. What's new in prostate cancer disease assessment in 2006?. *Curr. Opin. Urol.* 2006; 16(3): 146-51.
- [28] Eichler K, Hempel S, Wilby J, Myers L, Bachmann LM, Kleijnen J. Diagnostic value of systematic biopsy methods in the investigation of prostate cancer: a systematic review. *J. Urol.* 2006; 175(5): 1605-12.
- [29] Rajinikanth A, Manoharan M, Soloway CT, Civantos FJ, Soloway MS. Trends in Gleason score: concordance between biopsy and prostatectomy over 15 years. *Urology.* 2008; 72(1): 177-82.
- [30] Kvale R, Moller B, Wahlqvist R, Fossa SD, Berner A, Busch C, et al. Concordance between Gleason scores of needle biopsies and radical prostatectomy specimens: a population-based study. *BJU Int.* 2009; 103(12): 1647-54.
- [31] Koksall IT, Ozcan F, Kadioglu TC, Esen T, Kilicaslan I, Tunc M. Discrepancy between Gleason scores of biopsy and radical prostatectomy specimens. *Eur. Urol.* 2000; 37(6): 670-4.
- [32] Cookson MS, Fleshner NE, Soloway SM, Fair WR. Correlation between Gleason score of needle biopsy and radical prostatectomy specimen: accuracy and clinical implications. *J. Urol.* 1997; 157(2): 559-62.
- [33] Keetch DW, Catalona WJ, Smith DS. Serial prostatic biopsies in men with persistently elevated serum prostate specific antigen values. *J. Urol.* 1994; 151(6): 1571-4.
- [34] Futterer JJ, Verma S, Hambroek T, Yakar D, Barentsz JO. High-risk prostate cancer: value of multi-modality 3T MRI-guided biopsies after previous negative biopsies. *Abdom. Imag.* 2012; 37(5): 892-6.
- [35] Djavan B, Ravery V, Zlotta A, Dobronski P, Dobrovits M, Fakhari M, et al. Prospective evaluation of prostate cancer detected on biopsies 1, 2, 3 and 4: when should we stop?. *J. Urol.* 2001; 166(5): 1679-83.

- 
- [36] Jones JS. Editorial comment. Repeat prostate biopsy and the incremental risk of clinically insignificant prostate cancer. *Urology*. 2011; 77(3): 552.
- [37] Chang DT, Challacombe B, Lawrentschuk N. Transperineal biopsy of the prostate—is this the future?. *Nat. Rev. Urol.* 2013; 10(12): 690-702.
- [38] Haider MA, van der Kwast TH, Tanguay J, Evans AJ, Hashmi AT, Lockwood G, et al. Combined T2-weighted and diffusion-weighted MRI for localization of prostate cancer. *AM. J. Roentgenol.* 2007; 189(2): 323-8.
- [39] Lüdemann L, Prochnow D, Rohlfing T, Franiel T, Warmuth C, Taupitz M, et al. Simultaneous quantification of perfusion and permeability in the prostate using dynamic contrast-enhanced magnetic resonance imaging with an inversion-prepared dual sequence. *Ann. Biomed. Eng.* 2009; 2(37): 749-62.
- [40] Le Bihan D. Molecular diffusion nuclear magnetic resonance imaging. *Magn. Reson. Q.* 1991; 7: 1-30.
- [41] Seitz M, Shukla-Dave A, Bjartell A, Touijer K, Sciarra A, Bastian PJ, et al. Functional magnetic resonance imaging in prostate cancer. *Eur. Urol.* 2009; 55(4): 801-14.
- [42] American College of Radiology. MR Prostate Imaging Reporting and Data System version 2.0. (Accessed February 2019), from <http://www.acr.org/Quality-Safety/Resources/PIRADS/>.
- [43] Atkinson AJ, Colburn WA, Degruittola VG, Demets DL. Biomarkers and surrogate end-points: preferred definitions and conceptual framework. *Clin. Pharmacol. Ther.* 2001; 69: 89-95.
- [44] National Institute of Biomedical Imaging and Bioengineering homepage. <https://www.nibib.nih.gov/science-education/science-topics/magnetic-resonance-imaging-mri>. (Visited February 2019).
- [45] De Visschere P. Improving the diagnosis of clinically significant prostate cancer with magnetic resonance imaging. *J. Belg. Soc. Radiol.* 2018; 102(1): 22.
- [46] Janus C, Lippert M. Benign prostatic hyperplasia: appearance on magnetic resonance imaging. *Urology*. 1992; 40(6): 539-41.

- [47] Weinreb JC, Barentsz JO, Choyke PL, Cornud F, Haider MA, Macura KJ, et al. PI-RADS Prostate Imaging-Reporting and Data System: 2015, Version 2. *Eur. Urol.* 2016; 69(1): 16-40.
- [48] Vargas HA, Akin O, Franiel T, Goldman DA, Udo K, Touijer KA, et al. Normal central zone of the prostate and central zone involvement by prostate cancer: clinical and MR imaging implications. *Radiology.* 2012; 262(3): 894-902.
- [49] Kelloff GJ, Choyke P, Coffey DS, Working G. Prostate cancer imaging challenges in clinical prostate cancer: role of imaging. *AM. J. Roentgenol.* 2009; 192(6): 1455-70.
- [50] Akin O, Sala E, Moskowitz CS, Kuroiwa K, Ishill NM, Pucar D, et al. Transition zone prostate cancers: features, detection, localization and staging at endorectal MR imaging. *Radiology.* 2006; 239(3): 784-92.
- [51] Alonzi R, Hoskin P. Functional imaging in clinical oncology: magnetic resonance imaging – and computerised tomography-based techniques. *Clin. Oncol.* 2006; 18(7): 555-70.
- [52] Giannarini G, Petralia G, Thoeny HC. Potential and limitations of diffusion-weighted magnetic resonance imaging in kidney, prostate and bladder cancer including pelvic lymph node staging: a critical analysis of the literature. *Eur. Urol.* 2012; 61: 326-40.
- [53] Heijmink SW, Fütterer JJ, Strum SS, Oyen WJ, Frauscher F, Witjes JA, et al. State-of-the-art urologic imaging in the diagnosis of prostate cancer. *Acta Oncol.* 2011; 50(Suppl. 1): 25-38.
- [54] Collins DJ, Padhani AR. Dynamic magnetic resonance imaging of tumor perfusion. *IEEE Eng. Med. Biol. Mag.* 2004; 23: 65-83.
- [55] Jackson ASN, Reinsberg SA, Sohaib SA, Charles-Edwards EM, Jhavar S, Christmas TJ, Thompson AC, Bailey MJ, Corbishley CM, Fisher C, Leach MO, Dearnaley DP. Dynamic contrast-enhanced MRI for prostate cancer localization. *Br. J. Radiol.* 2009; 82: 148–56.
- [56] Leach MO, Brindle KM, Evelhoch JL, Griffiths JR, Horsman MR, Jackson A, et al. The assessment of antiangiogenic and antivascular therapies in early-stage clinical trials using magnetic resonance imaging: issues and recommendations. *Br. J. Cancer.* 2005; 92: 1599–610.

- 
- [57] Tofts PS, Brix G, Buckley DL, Evelhoch JL, Henderson E, Knopp MV, et al. Estimating kinetic parameters from dynamic contrast-enhanced T1-weighted MRI of a diffusable tracer: standardized quantities and symbols. *J. Magn. Reson. Imaging*. 1999; 10: 223–32.
- [58] Sourbron SP, Buckley DL. Tracer Kinetic modelling in MRI: estimating perfusion and capillary permeability. *Phys. Med. Biol.* 2012; 57(2): R1-R33.
- [59] Leach MO, Brindle KM, Evelhoch JL, Griffiths JR, Horsman MR, Jackson A, et al. Assessment of antiangiogenic and antivascular therapeutics using MRI: recommendations for appropriate methodology for clinical trials. *Br. J. Radiol.* 2003; 76(Spec N° 1): S87-91.
- [60] Port RE, Knopp MV, Brix G. Dynamic contrast-enhanced MRI using Gd-DTPA: interindividual variability of the arterial input function and consequences for the assessment of kinetic in tumors. *Magn. Reson. Med.* 2001; 45: 1030-38.
- [61] McGrath DM, Bradley DP, Tessier JL, Lacey T, Taylor CJ, Parker GJ. Comparison of model-based arterial input functions for dynamic contrast-enhanced MRI in tumor bearing rats. *Magn. Reson. Med.* 2009; 61: 1173-84.
- [62] Yang C, Karczmar GS, Medved M, Oto A, Zamora M, Stadler WM. Reproducibility assessment of a multiple tissue method for quantitative dynamic contrast-enhanced MRI analysis. *Magn. Reson. Med.* 2009; 61: 851-59.
- [63] Meng R, Chang SD, Jones EC, Goldenberg SL, Kozlowski P. Comparison between population average and experimentally measured arterial input function in predicting biopsy results in prostate cancer. *Acad. Radiol.* 2010; 17: 520-5.
- [64] Jackson JE. A User's guide to Principal Components. Ed. Wiley: New York, 1991.
- [65] Sanz-Requena R, Prats-Montalbán JM, Martí-Bonmatí L, Alberich-Bayarri A, García-Martí G, Pérez R, Ferrer A. Automatic individual arterial input functions calculated from PCA outperform manual and population-averaged approaches for the pharmacokinetic modeling of DCE-MR images. *J. Magn. Reson. Imaging*. 2015; 42: 477-87.
- [66] Charles-Edwards EM, De Souza NM. Diffusion weighted-magnetic resonance imaging and its application to cancer. *Cancer Imaging*. 2006; 6: 135-43.
- [67] Le Bihan D, Breton E, Lallemand D, Aubin ML, Vignaud J, Laval-Jeantet M. Separation of diffusion and perfusion in intravoxel incoherent motion MR imaging. *Radiology*. 1988; 168(2): 497-505.

- [68] Gili J. Técnicas especiales en IRM. In Gili J, editor. Introducción biofísica a la resonancia magnética aplicada a la clínica. II. Barcelona: Universidad Autónoma de Barcelona; 2007. p. 141-6.
- [69] Le Bihan D, Turner R, Douek P, Patronas N. Diffusion MR imaging: clinical applications. *AM. J. Roentgenol.* 1992; 159(3): 591-9.
- [70] Garcia Figueiras R, Padhani AR, Vilanova JC, Goh V, Villalba Martin C. [Functional imaging of tumors. Part 1]. *Radiología.* 2010; 52(2): 115-25.
- [71] Lemke A, Stieltjes B, Schard LR, Faun FB. Toward an optimal distribution of b values for intravoxel incoherent motion imaging. *Magn. Reson. Imaging.* 2011; 29: 766-76.
- [72] Szafer A, Zhong J, Anderson AW, Gore JC. Diffusion-weighted imaging in tissues: theoretical models. *NMR Biomed.* 1995; 8(7-8): 289-96.
- [73] Le Bihan D, Breton E, Lallemand D, Grenier P, Cabanis E, Laval-Jeantet M. MR imaging of intravoxel incoherent motions: application to diffusion and perfusion in neurologic disorders. *Radiology.* 1986; 161: 401-7.
- [74] Cho GN, Moy L, Zhang JL, Baete S, Lattanzi R, Moccaldi M, et al. Comparison of fitting methods and b-value sampling strategies for intravoxel incoherent motion in breast cancer. *Magn. Reson. Med.* 2015; 74(4): 1077-85.
- [75] Vargas HT, Hötker AM, Goldman DA, Moskowitz CS, Gondo T, Matsumoto K, et al. Updated prostate imaging reporting and data system (PIRADS v2) recommendations for the detection of clinically significant prostate cancer using multiparametric MRI: critical evaluation using whole-mount pathology as standard of reference. *Eur. Radiol.* 2016; 26: 1606-12.
- [76] Donaldson SB, West CML, Davidson SE, Carrington BM, Hutchison G, Jones AP, et al. A comparison of tracer kinetics models for T1-weighted dynamic contrast-enhanced MRI: application in carcinoma of the cervix. *Magn. Reson. Med.* 2010; 63: 691-700.
- [77] Geladi P, Grahn. Multivariate Image Analysis. *Wiley.* Chichester, England, 1996.
- [78] Prats-Montalbán JM, Ferrer A, de Juan A, Multivariate image analysis: a review with applications. *Chemom. Intell. Lab. Syst.* 2011; 107: 1-23.
- [79] Jackson JE. A user's guide to principal components. New York: *Wiley*; 2003.
- [80] De Juan A, Tauler R. Multivariate curve resolution (MCR) from 2000: progress in concepts and applications. *Crit. Rev. Anal. Chem.* 2006; 36(3-4): 163-76.

- 
- [81] Tauler R, Smilde AK, Kowalski BR. Selectivity local rank, three-way data analysis and ambiguity in multivariate curve resolution. *J. Chemom.* 1995; 9: 31-58.
- [82] Multivariate Curve Resolution homepage. <http://www.mcrals.info/>. (Accessed February 2019).
- [83] Geladi P, Kowalski BR. Partial Least-Squares Regression: A Tutorial, *Anal. Chim. Acta.* 1986; 185: 1-17.
- [84] Sjöström M, Wold S, Söderström B. (1986) PLS Discriminant Plots, Proceedings of PARC in Practice, Amsterdam, June 19-21, 1985. Elsevier Science Publishers B.V., North-Holland.
- [85] Bruwer MJ, MacGregor JF, Noseworthy D. Dynamic contrast-enhanced MRI diagnosis in oncology via principal component analysis. *J. Chemom.* 2008; 22: 708-16.
- [86] Gurjal P, Amrhein M, Bonvin D, Vallée JP, Montet X, Michoux N. Classification of magnetic resonance images from rabbit renal perfusion. *Chemom. Intell. Lab. Syst.* 2009; 98: 173-81.
- [87] Fortuna J, Elzibak AH, Fan Z, MacGregor JF, Noseworthy MD. Liver functional magnetic resonance imaging analysis using a latent variable approach. *J. Chemom.* 2012; 26: 170-9.
- [88] Prats-Montalbán JM, Sanz-Requena R, Martí-Bonmatí L, Ferrer A. Prostate functional magnetic resonance image analysis using multivariate curve resolution methods. *J. Chemom.* 2014; 28(8): 672-80.
- [89] Aguado-Sarrió E, Prats-Montalbán JM, Sanz-Requena R, Alberich-Bayarri A, Martí-Bonmatí L, Ferrer A. Prostate diffusion weighted-magnetic resonance image analysis using multivariate curve resolution methods. *Chemom. Intell. Lab. Syst.* 2015; 140: 43-8.
- [90] Prats-Montalbán JM, Aguado-Sarrió E, Ferrer A. (2016) Multivariate Curve Resolution for Magnetic Resonance Image analysis: applications in prostate cancer biomarkers development. In "*Resolving Spectral Mixtures, with application from ultrafast spectroscopy to super-resolution imaging*", Data Handling in Science and Technology 30, 519–550, Elsevier, Amsterdam.
- [91] Piqueras S, Duponchel L, Tauler R, de Juan A. Resolution and segmentation of hyperspectral biomedical images by multivariate curve resolution-alternating least squares. *Anal. Chim. Acta.* 2011; 705: 182-92.

- [92] Sanz-Requena R, Martí-Bonmatí L, Pérez-Martínez R, García-Martí G. Dynamic contrast-enhanced case-control analysis in 3T MRI of prostate cancer can help to characterize tumor aggressiveness, *Eur. J. Radiol.* 2016; 85: 2119-26.
- [93] Lauzon-Gauthier J, Duchesne C. A new multiblock PLS algorithm including a sequential pathway. In: *EuroPact 2014*, May 6-9, 2014, Barcelona, Spain. 130.
- [94] Azari K, Lauzon-Gauthier J, Tessier C, Duchesne C. Establishing multivariate specification regions for raw materials using SMB-PLS, In: “*Proceedings of the 9<sup>th</sup> IFAC symposium on advanced control of chemical processes*”, ADCHEM 2015, Whistler, BC, Canada, 2015, 1132-37.
- [95] Lauzon-Gauthier J, Manolescu P, Duchesne C. The sequential multi-block PLS algorithm (SMB-PLS): Comparison of performance and interpretability. *Chemom. Intell. Lab. Syst.* 2018; 180: 72-83.
- [96] Tauler R. Multivariate curve resolution applied to second order data. *Chemom. Intell. Lab. Syst.* 1995; 30: 133-46.
- [97] De Juan A, Tauler R. Chemometrics applied to unravel multicomponent processes and mixtures: revisiting latest trends in multivariate resolution. *Anal. Chim. Acta.* 2003; 500: 195-210.
- [98] Jaumot J, Gargallo R, de Juan A, Tauler R. A graphical user-friendly interface for MCR-ALS: a new tool for multivariate curve resolution in MATLAB. *Chemom. Intell. Lab. Syst.* 2005; 76: 101-10.
- [99] Windig W, Guilment J. Interactive self-modeling mixture analysis. *Anal. Chem.* 1991; 63: 1425-32.
- [100] De Juan A, Maeder M, Hancewicz T, Duponchel L, Tauler R. Chemometric tools for image analysis. In “*infrared and Raman Spectroscopic Imaging*”. Wiley-VCH Verlag GmbH & Co. KGaA, 2009; 65-109.
- [101] Næs T, Tomic O, Mevik BH, Martens H. Path modelling by sequential PLS regression. *J. Chemom.* 2011; 25: 28-40.
- [102] Wangen LE, Kowalski BR. A multiblock partial least squares algorithm for investigating complex chemical systems. *J. Chemom.* 1989; 3: 3-20.
- [103] MacGregor JF, Jaeckle C, Kiparissides C, Koutoudi M. Process monitoring and diagnosis by multiblock PLS methods. *AIChE J.* 1994; 40: 826-38.
- [104] Gargallo R, Tauler R, Cuesta-Sanchez F, Massart DL. Validation of alternating least-squares multivariate curve resolution for chromatographic resolution and quantitation. *TrAC, Trends Anal.Chem.* 1996; 15(7): 279-86.

- 
- [105] Smilde AK, Tauler R, Saurina J, Bro R. Calibration methods for complex second-order data. *Anal. Chim. Acta.* 1999; 398(2-3): 237-51.
- [106] De Juan A, Maeder M, Hancewicz T, Tauler R. Local rank analysis for exploratory spectroscopic image analysis. Fixed size image window-evolving factor analysis. *Chemom. Intell. Lab. Syst.* 2005; 77(1-2): 64-74.
- [107] Gallagher NB, Shaver JM, Martin EB, Morris J, Wise BM, Windig W. Curve resolution for multivariate images with applications to TOF-SIMS and Raman. *Chemom. Intell. Lab. Syst.* 2004; 73: 105-17.
- [108] Jaumot J, Tauler R. MCR-BANDS: a user friendly MATLAB program for the evaluation of rotation ambiguities in multivariate curve resolution. *Chemom. Intell. Lab. Syst.* 2010; 103: 96-107.
- [109] Chtioui Y, Bertrand D, Barba D. Feature selection by a genetic algorithm. Application to seed discrimination by artificial vision. *J. Sci. Food Agric.* 1998; 76: 77-86.
- [110] Leardi R. Nature-inspired methods in chemometrics: genetic algorithms and artificial neural networks. *Data handling in science and technology*, vol 23. Amsterdam: Elsevier: 2003.
- [111] Wang M, Zhou X, King R, Wong STC. Context based mixture model for cell phase identification in automated fluorescence microscopy. *BMC Bioinf.* 2007; 8(32): 1-12.
- [112] Cuesta Sánchez F, Toft J, van den Bogaert B, Massart DL. Orthogonal projection approach applied to peak purity assessment. *Anal. Chem.* 1996; 68: 79-85.
- [113] De Juan A, Maeder M, Hancewicz T, Tauler R. Use of local rank-based spatial information for resolution of spectroscopic images. *J. Chemom.* 2008; 22: 291-8.
- [114] Ked HR, Massart DL. Peak purity control in liquid chromatography with photodiode-array detection by a fixed size moving evolving factor analysis. *Anal. Chim. Acta.* 1991; 246: 379-90.
- [115] Aguado-Sarrió E, Prats-Montalbán JM, Sanz-Requena R, Garcia-Martí G, Martí-Bonmatí L, Ferrer A. Biomarker comparison and selection for prostate cancer detection in Dynamic Contrast Enhanced-Magnetic Resonance Imaging (DCE-MRI). *Chemom. Intell. Lab. Syst.* 2017; 165: 38-45.
- [116] Sjöström M, Wold S, Söderström B. (1986) PLS Discriminant Plots, Proceedings of PARC in Practice, Amsterdam, June 19-21, 1985. Elsevier Science Publishers B.V., North-Holland.

- [117] Westerhuis J, Hoefsloot H, Smit S, Vis D, Smilde A, van Velzen E, et al. Assessment of PLS-DA cross validation. *Metabolomics*. 2008; 4: 81-89.
- [118] Kuligowski J, Pérez-Guaita D, Escobar J, de la Guardia M, Vento M, Ferrer A, et al. Evaluation of the effect of chance correlations on variable selection using partial least squares-discriminant analysis. *Talanta*. 2013; 116: 835-40.
- [119] Jackson AS, Reinsberg SA, Sohaib SA, Charles-Edwards EM, Jhavar S, Christmas TJ, et al. Dynamic contrast-enhanced MRI for prostate cancer localization. *Br. J. Radiol.* 2009; 82: 148-56.
- [120] Franiel T, Lüdemann L, Rudolph B, Lutterbeck E, Hamm B, Beyersdorff D. Differentiation of prostate cancer from normal prostate tissue: role of hotspots in pharmacokinetic MRI and histologic evaluation. *AM. J. Roentgenol.* 2010; 194: 675-81.
- [121] Vos EK, Litjens GJ, Kobus T, Hambroek T, Hulsbergen-van de Kaa CA, Barentsz JO, et al Assessment of prostate cancer aggressiveness using dynamic contrast-enhanced MRI at 3T. *Eur. Urol.* 2013; 64: 448-55.
- [122] Durmus T, Vollnberg B, Schwenke C, Kilic E, Huppertz A, Taupitz M, et al. Dynamic contrast-enhanced MRI of the prostate: comparison of gadobutrol and Gd-DTPA. *Fortschr. Röntgenstr.* 2013; 185: 862-8.
- [123] Yetisgen-Yildiz M, Gunn M.L, Xia F, Payne TH. A text processing pipeline to extract recommendations from radiology reports. *J. Biomed. Inform.* 2013; 46: 354-62.
- [124] Pham AD, Névéol A, Lavergne T, Yasunaga D, Clément O, Meyer G, et al. Natural language processing of radiology reports for the detection of thromboembolic diseases and clinically relevant incidental findings. *BMC Bioinf.* 2014; 15: 266.
- [125] Obuchowski NA. Receiver Operating Characteristic Curves and their use in radiology. *Radiology*. 2003; 229: 3-8.
- [126] Favilla S, Durante C, Li Vigni M, Cocchi M. Assessing feature relevance in NPLS models by VIP. *Chemom. Intell. Lab. Syst.* 2013; 129: 76-86.
- [127] Tibshirani R. Regression shrinkage and selection via the lasso. *J. Royal Stat. Soc. Series B (Methodological)*. 1996; 58: 267-88.
- [128] Hastie T, Tibshirani R, Friedman J. (2009) *The Elements of Statistical Learning*. New York: Springer.

## ANNEX 1: PSEUDO-CODE OF THE SMB-ALGORITHM (CHAPTER 3.3)

**For**  $b= 1,2 \dots B-1$

1. Set  $\mathbf{u}$  to any column of  $\mathbf{Y}$  as an initialization
2. Begin the convergence loop
  - 2.1.  $\mathbf{w}_b = \mathbf{X}_b^T \cdot \mathbf{u} / (\mathbf{u}^T \cdot \mathbf{u})$
  - 2.2.  $\mathbf{w}_b = \mathbf{w}_b / \|\mathbf{w}_b\|$
  - 2.3.  $\mathbf{t}_b = \mathbf{X}_b \cdot \mathbf{w}_b$

**For**  $k = 1,2 \dots B-b$

- 2.4.  $\mathbf{X}_{b+k}^{corr} = \mathbf{t}_b \cdot (\mathbf{t}_b^T \cdot \mathbf{t}_b)^{-1} \cdot \mathbf{t}_b^T \cdot \mathbf{X}_{b+k}$
- 2.5.  $\mathbf{w}_{b+k}^{corr} = \mathbf{X}_{b+k}^{Tcorr} \cdot \mathbf{u} / (\mathbf{u}^T \cdot \mathbf{u})$
- 2.6.  $\mathbf{w}_{b+k}^{corr} = \mathbf{w}_{b+k}^{corr} / \|\mathbf{w}_{b+k}^{corr}\|$
- 2.7.  $\mathbf{t}_{b+k}^{corr} = \mathbf{X}_{b+k}^{corr} \cdot \mathbf{w}_{b+k}^{corr}$

**End**

- 2.8.  $\mathbf{T} = [\mathbf{t}_b \ \mathbf{t}_{b+1}^{corr} \ \dots \ \mathbf{t}_B^{corr}]$
- 2.9.  $\mathbf{w}_T = \mathbf{T}^T \cdot \mathbf{u} / (\mathbf{u}^T \cdot \mathbf{u})$
- 2.10.  $\mathbf{w}_T = \mathbf{w}_T / \|\mathbf{w}_T\|$
- 2.11.  $\mathbf{t}_T = \mathbf{T}^T \cdot \mathbf{w}_T / (\mathbf{w}_T^T \cdot \mathbf{w}_T)$
- 2.12.  $\mathbf{q} = \mathbf{Y}^T \cdot \mathbf{t}_T / (\mathbf{t}_T^T \cdot \mathbf{t}_T)$
- 2.13.  $\mathbf{u} = \mathbf{Y} \cdot \mathbf{q} / (\mathbf{q}^T \cdot \mathbf{q})$

Loop until convergence on  $\mathbf{t}_T$  or  $\mathbf{u}$ . Go to step 3 when converged.

3. **For**  $k = b, b+1 \dots B$ 
  - 3.1.  $\mathbf{p}_k = \mathbf{X}_k^T \cdot \mathbf{t}_T / (\mathbf{t}_T^T \cdot \mathbf{t}_T)$
  - 3.2.  $\mathbf{E}_k = \mathbf{X}_k - \mathbf{t}_T \cdot \mathbf{p}_k^T$

**End**

4.  $\mathbf{F} = \mathbf{Y} - \mathbf{t}_T \cdot \mathbf{q}^T$
5. Store all vectors at the block and super levels as new columns in matrices.
6. To compute the next LV, replace  $\mathbf{X}_k$  by  $\mathbf{E}_k$  ( $k \geq b$ ) and  $\mathbf{Y}$  by  $\mathbf{F}$  and go back to step 1.
7. When the relevant info in block  $\mathbf{X}_b$  is depleted, increment  $b$  and start at step 1. Using  $\mathbf{X}_b$  and  $\mathbf{Y}$  residuals.

**End**

8. For  $b = B$ , fit a regular PLS model to  $\mathbf{E}_B$  and  $\mathbf{F}$ .